



# Kent Academic Repository

**Cowell, Jordan (2023) *First Principles Study of Ferroelectricity in Halide Perovskites for Future Photoferroics*. Doctor of Philosophy (PhD) thesis, University of Kent,.**

## Downloaded from

<https://kar.kent.ac.uk/99936/> The University of Kent's Academic Repository KAR

## The version of record is available from

## This document version

UNSPECIFIED

## DOI for this version

## Licence for this version

CC BY (Attribution)

## Additional information

## Versions of research works

### Versions of Record

If this version is the version of record, it is the same as the published version available on the publisher's web site. Cite as the published version.

### Author Accepted Manuscripts

If this document is identified as the Author Accepted Manuscript it is the version after peer review but before type setting, copy editing or publisher branding. Cite as Surname, Initial. (Year) 'Title of article'. To be published in *Title of Journal*, Volume and issue numbers [peer-reviewed accepted version]. Available at: DOI or URL (Accessed: date).

## Enquiries

If you have questions about this document contact [ResearchSupport@kent.ac.uk](mailto:ResearchSupport@kent.ac.uk). Please include the URL of the record in KAR. If you believe that your, or a third party's rights have been compromised through this document please see our [Take Down policy](https://www.kent.ac.uk/guides/kar-the-kent-academic-repository#policies) (available from <https://www.kent.ac.uk/guides/kar-the-kent-academic-repository#policies>).

# First Principles Study of Ferroelectricity in Halide Perovskites for Future Photoferroics

A thesis submitted for the degree of  
Doctor of Philosophy

by

Jordan A.R. Cowell

School of Physical Sciences

University of  
**Kent**

Canterbury

UK

May 31, 2022



*The two most important days in your life are the day you are born and the day you  
find out why...*

Mark Twain

*To everyone who couldn't be here to celebrate this work with me... I miss you all*

# Declaration

The work performed in this review titled "First principles study of ferroelectricity in halide perovskites for future photoferroics" was performed under the supervision of Dr. Nicholas Bristowe. I declare that all work is entirely my own, and has not been submitted for the purposes of a qualification at any other institution or any other degree. Elements of the work presented in this review are the product of collaborations with colleagues, and as such I would like to declare their contribution:

- Chapter 4: Development of the code to determine the effect of the dielectric response from the phonon modes was done with help from my good friend Jay Verma. You can find a copy of this code and the phonon-dielectric tables in [Appendix B](#).
- Chapter 5: This work is an expansion of a review originally completed by Andrew McMahon (Imperial College London). In his review he looked at improper ferroelectricity in Lead halide perovskites. We look to expand upon this by looking at a variety of chemistries and developing a link between the size of the polar distortion and the band-gap.

Jordan A.R. Cowell



# Acknowledgements

I would like to firstly acknowledge a massive group of people who have supported me, encouraged me and helped me throughout my PhD. Ever since I went to university to study physics I wanted to complete some research and it has been the hardest thing I've ever done. Without all of these people I mention I wouldn't have ever made so I thank every single one of you. Thank you for the University of Kent for allowing me to carry out this research project and supporting me with a Vice-Chancellor's PhD Studentship.

I would like to thank all *three* of my supervisors. Firstly Nick, my *actual* supervisor who has been one the most supportive, patient, fair and firm people I've had the pleasure to work with. Without his continued support throughout the entirety of my PhD I would not have got to the point I have now. I will be eternally grateful for everything you have done for me. Secondly, I would like to thank Emma who was my second source of guidance throughout my PhD, helping me with a lot of the chemistry that I didn't know that I would need to learn, so once again, eternally grateful for your help and support through this. Finally, Paul, my third supervisor. Thank you for your support throughout the end of my PhD and especially as I have come to the end of writing up, your guidance has been very helpful.

There are so many people that I want to thank here so some will be very generalised. I want to say thanks to all of the people I worked with at the University of Kent from the MEE group to rooms 104 and 114, I miss all of the interesting conversations that we had about each others research and your probing questions in our

group meetings helped develop my project and even develop my own understanding about my work. I send thanks and well wishes to everyone on my old university football team Unathletico Madrid - thanks for all the brilliant nights out and great afternoons on the pitch.

Thank you to all of my old university housemates for all of the wonderful evenings and support. Thank you to all of my friends from home, for being that secondary support network. There are a few I want to name more personally. Thanks to Kier, Ox, Seb, Chloe, Jack, Lewis, Callum and Rosa for being the greatest friends a man could want/need. Our nights of gaming, DnD drinking and general shenanigans has kept me sane throughout all of the academic pain I decided to put myself through. I want to extend a thank you to all of my colleagues at school (SLGGS). Thank you especially to Arwen, Jo, Malcolm and Pat and more recently Becky for your wonderful support. Thank you for covering and supporting me through the final sections of this thesis, you're all absolutely stellar. Finally I want to say thanks to a few more people:

- Jay: Thanks for being there mate, you've always been by my side as I've been by yours, heres to many more years bud!
- Sam: Thanks for being a great housemate and a brilliant friend, here's to many more years of moaning about Gordon in the White Hart!
- Nan: Thank you for giving me that big red book of 1000 science facts 20 years ago... you could probably state you're the reason I wrote this. Thanks for being my greatest academic fan. I'll make sure you've got a bound copy!
- Dad: Thanks for being the most supportive dad possible. You've always said I can achieve whatever I want and that's what has driven me to this points. Thanks mate.
- Mum: Thank you for all of the evenings of deep chats, drinking and singing. Thank you for believing in me (Without that chat in second year I wouldn't be here now), Thank you for fighting through everything you have been through,

you've been a complete soldier over the year of this submission and i'm so proud you have pulled through!

- Syd: Thanks for being a nuisance :) and being supportive to everything I do. I'm glad we are finally getting on like brother and sister should, let it continue.

And finally, thank you to Paul. My partner in crime, my drinking buddy, my absolute best friend, my academic equal. Can't wait for us to spend the rest of our lives together chatting nonsense, drinking in pubs and eating in every restaurant in the UK. I'm so blessed to have such a wonderful support network of colleagues, friends and family. Thank you all so so much.

**This is for all of you!**



# Abstract

Perovskite and perovskite-like materials have garnered warranted attention over the previous decade due to their potential use in high efficiency photovoltaic devices. Their flexibility both chemically and sterically gives materials' scientists and engineers the opportunity to tune the properties of such materials to suit the application that it is needed for. In this thesis we use *ab initio* methods to describe the fundamental distortions that appear in a series of structures and their associated optoelectronic properties. In the first results chapter we complete a rigorous exploration of a variety of chemistries where we explore the various distortions that can appear in these materials. I show that the system exhibits a very complex interplay between primarily the breathing distortion and Jahn-Teller distortion and subsequently all other distortions that appear at lower tolerance factors. We also explore the appearance of a polar instability. In the second results chapter we take the understanding of these distortions and physical aspects of the gold double perovskites to discuss the optoelectronic properties of these materials. We find that the Jahn-Teller distortion opens up the gap in a metallic to insulator phase transition, we examine the effects of each of the distortions on the size of the gap and the effective masses of the structures and we see that the introduction of tilt distortions opens up the gap even more and increases the effective masses of the charge carriers. Examination of pressure presented us with the unusual discovery that hydrostatic pressure suppresses the appearance of the tilt distortions in this perovskite structure due to the cooperative nature between the tilt and Jahn-Teller distortions (something that is suppressed with pressure). With the

knowledge of the effects of pressure we predicted a polar phase in the  $\text{Rb}_2\text{Au}_2(\text{Br}, \text{I})_6$  structures with the introduction of a small hydrostatic pressure. We explored the possibility of an enhanced dielectric constant through tuning of lattice parameters with pressure and was able to show an enhanced dielectric constant at a region where the phonon frequency was sufficiently softened. In the final part of the thesis we discussed the application of *hybrid improper ferroelectricity*. We showed through symmetry analysis that a polar distortion appears in the low-symmetry  $\text{A}_3\text{B}_2\text{X}_7$  (A = Cs, Rb, K; B = Pb, Sn, Ge; X = I, Br, Cl) Ruddlesden-Popper structures via a trilinear coupling term with two non-polar distortions. We explored the effect of chemical substitution on the size of the gap and the effects each change in the chemistry had on the size of the distortions, we suggested that the  $\text{Cs}_3\text{Ge}_2\text{I}_7$  system is a proper ferroelectric (does not follow the improper method) and finally we explored the effects of Spin-Orbit coupling and the type of exchange-correlation functional that was used on the accuracy of our results. Overall we believe that the work presented in this review puts forward some exciting and interesting discussions of charge-separation in perovskite photovoltaics. As we look forward in this review we make some suggestions of other structures which would be more suitable for a possible experimental analysis.

# Abbreviations

**DFT** – Density Functional Theory

**FE** – Ferroelectricity

**PCE** – Power Conversion Efficiency

**PV** – Photovoltaics

**DoS** – Density of States

**IRREPS** – Irreducible Representation

**HIFE** – Hybrid Improper Ferroelectricity

**LDA** – Local Density Approximation

**GGA** – Generalised Gradient Approximation

**PAW** – Projected Augmented Wave

**DFPT** – Density Functional Perturbation Theory

**CIF** – Crystallographic Information File

**VB(M)** – Valence Band (Maximum)

**CB(M)** – Conduction Band (Minimum)

**MAPI** – Methylammonium Lead Iodide

# Contents

<b>Declaration</b>	<b>3</b>
<b>Acknowledgements</b>	<b>4</b>
<b>Abstract</b>	<b>8</b>
<b>Abbreviations</b>	<b>11</b>
<b>Contents</b>	<b>12</b>
<b>List of Figures</b>	<b>16</b>
<b>List of Tables</b>	<b>23</b>
<b>1 Introduction</b>	<b>25</b>
1.1 Photovoltaic History and Function . . . . .	28
1.2 Solar Cells . . . . .	32
Semiconductors and The Photovoltaic Effect . . . . .	32
1.3 Perovskites . . . . .	42
1.4 Ferroelectrics . . . . .	48
Photoferroics . . . . .	53
1.5 Outline and Aims of Thesis . . . . .	57
<b>2 Theoretical and Computational Methods</b>	<b>59</b>

<i>CONTENTS</i>	13
2.1 Density Functional Theory . . . . .	60
Clamped Nuclei and Born-Oppenheimer Approximations . . . . .	62
Hohenberg & Kohn Theorem . . . . .	63
Kohn-Sham Equations . . . . .	64
Local Density Approximation (LDA) . . . . .	65
Beyond the Local Density Approximation . . . . .	66
Self-Consistent Equations . . . . .	69
2.2 Periodicity, Basis Sets & Pseudopotentials . . . . .	72
Periodicity and Reciprocal Space . . . . .	72
Basis Sets . . . . .	74
Plane Waves . . . . .	74
Pseudopotentials . . . . .	75
2.3 Density Functional Perturbation Theory . . . . .	77
Hellman-Feynmann Theorem . . . . .	77
DFPT Methodology . . . . .	78
2.4 Post-Processing Methods . . . . .	79
Process . . . . .	81
2.5 Conclusion . . . . .	81
<b>3 The Structural Complexity of Gold Halide Double Perovskites</b>	<b>83</b>
3.1 Introduction . . . . .	84
Competition vs. Cooperation . . . . .	84
Gold Double Perovskites . . . . .	85
3.2 Computational Methods . . . . .	89
3.3 Results . . . . .	89
Analysis of the Tetragonal Phases and Phonons . . . . .	89
Analysis of the Tilted Phase . . . . .	94
Low Symmetry Phase . . . . .	99
Phase Diagram . . . . .	101
Polar Phase . . . . .	102

Proper . . . . .	102
Improper . . . . .	106
3.4 Conclusions . . . . .	106
<b>4 Tuning the Optoelectronic and Dielectric Properties of Gold Double Perovskites</b>	<b>109</b>
4.1 Introduction . . . . .	110
Dielectric Response through Phonons . . . . .	111
4.2 Results . . . . .	112
Cubic $\rightarrow$ $I4/mmm$ . . . . .	112
$I4/mmm \rightarrow C2/m$ . . . . .	120
$I4/mmm \rightarrow P2_1/c$ . . . . .	123
Effects of Pressure on Distortions . . . . .	126
Dielectric Response . . . . .	129
4.3 Conclusions and Final Remarks . . . . .	132
<b>5 Engineering Ferroelectricity in Metal Halide Perovskites</b>	<b>135</b>
5.1 Introduction . . . . .	136
Ferroelectric Solar Cells . . . . .	138
5.2 Hybrid Improper Ferroelectricity . . . . .	139
5.3 Computational Methods . . . . .	142
5.4 Results . . . . .	143
Structural Analysis of the $I4/mmm$ and $Cmc2_1$ Phases . . . . .	143
Electronic Structure of $I4/mmm$ and $Cmc2_1$ . . . . .	145
Discussion of Band-Gap . . . . .	150
Functionals and Spin-Orbit Coupling . . . . .	152
5.5 Conclusions and Final Remarks . . . . .	154
<b>6 Conclusions, Final Remarks and Future Work</b>	<b>157</b>
Chapter 3: Structural Analysis . . . . .	158
Chapter 4: Optoelectronic Analysis . . . . .	158

<i>CONTENTS</i>	15
Chapter 5: Hybrid Improper Ferroelectricity . . . . .	159
Final Remarks . . . . .	160
<b>Bibliography</b>	<b>161</b>
<b>Appendices</b>	<b>188</b>
<b>A The Structural Complexity of Gold Halide Double Perovskites APPENDIX</b>	<b>189</b>
A.1 Rb <sub>2</sub> Au <sub>2</sub> I <sub>6</sub> Phonons . . . . .	190
A.2 Full INVARIANTS Analysis of Structures . . . . .	190
Pm $\bar{3}$ m $\rightarrow$ I4/mmm . . . . .	190
Pm $\bar{3}$ m $\rightarrow$ C2/m . . . . .	191
Pm $\bar{3}$ m $\rightarrow$ P2 <sub>1</sub> /c . . . . .	191
Pm $\bar{3}$ m $\rightarrow$ I4mm (Strain Induced Mechanism) . . . . .	192
Pm $\bar{3}$ m $\rightarrow$ I4mm (Improper Mechanism) . . . . .	192
<b>B Tuning the Optoelectronic and Dielectric Properties of Gold Double Perovskites APPENDIX</b>	<b>193</b>
B.1 Electronic Density of States: Rb <sub>2</sub> Au <sub>2</sub> I <sub>6</sub> . . . . .	194
B.2 Electronic Density of States: K <sub>2</sub> Au <sub>2</sub> I <sub>6</sub> . . . . .	196
B.3 Phonon Dielectrics . . . . .	198
Dielectric Code . . . . .	198

# List of Figures

1.1	The correlation between the temperature change of the atmosphere in comparison to today's temperature and the amount of CO <sub>2</sub> in the atmosphere in PPM. . . . .	26
1.2	The share of electricity from different sources for the world. What we see is a <i>slow</i> decline in the use of fossil fuels but overall there is still a massive over reliance on coal. Generally across the world we see a more of reduction in the use of coal, but an increase in either oil or gas. Figure from [3]. . . . .	27
1.3	This graphic from Our World in Data shows explicitly that even though there has been reductions in the overall percentage of fossil fuels being burnt for fuel, the overall percentage is a constant increase in the amount that is being burnt due to the overall increase in human population on the Earth. Figure from [3]. . . . .	27
1.4	NREL summary of the different photovoltaic cells that have been produced through time with the associated efficiencies[8]. . . . .	30
1.5	Evolution of the PCE of inorganic halide solar cells from the original CsSnI <sub>3</sub> up to the more recent CsPbI <sub>3</sub> . Figure from [15]. . . . .	31
1.6	Basic description of a) an insulator b) a semiconductor and c) a metal. . . .	33
1.7	Simple schematic of the excitation of an electron from the valence band (VB) to the conduction band (CB). . . . .	36

<i>List of Figures</i>	17
1.8 Schematic of a $p$ - $n$ junction showing the depletion zone and the formation of the electric field across the junction. This allows for the charges to be separated when excitation occurs. Schematic from [29]	38
1.9 A) Energy band diagrams of p-type and n-type semiconductors. B) The energy diagram of a pn-junction which is in equilibrium. Similar to figure 1.8 we can see a potential barrier appear between the two types of semiconductor. Figure from [30].	38
1.10 Basic JV curve which shows the different characteristics of a photovoltaic device ( $V_{OC}$ , $J_{SC}$ , $FF$ , $P_{MPP}$ .), Figure from [31]	40
1.11 Structure of the SrTiO <sub>3</sub> Perovskite which shows the corner sharing octahedra at the centre of the structure. The Strontium atoms surround the octahedra. Atomic positions from [34]	43
1.12 Ferroelectric hysteresis loop with some key points for the loop. $\mathbf{P}_{sat}$ is the saturation polarisation, $\mathbf{P}_r$ is the remnant polarisation and $E_c$ is the coercive field. Figure from [58].	49
1.13 1-Dimensional chain of alternating ions with negative and positive charge. The dashed lines show two different unit cells of same length $a$	50
1.14 Visual description of a possible mechanism of the BPE in ferroelectric photovoltaics. Three energy scenarios above the ground state which show the photocurrent moving to the right over the asymmetric potential wells that form in non-centrosymmetric crystals. Figure taken from [68]	55
2.1 The different methods that are employed in condensed matter physics when looking at particular time and length scale regimes. Figure is taken from [90].	60
2.2 Jacobs ladder of exchange-correlation functionals linking the Hartree world to the heaven of chemical accuracy. Higher up the ladder leads to increased computational expense but with increased chemical accuracy.	67
2.3 An adapted flow chart of the one found in chapter 3 of [94] showing the self-consistent method of calculating the electronic density.	71

2.4	PBE bandstructure of a silicon crystal to show the bands passing through the critical points of the Brillouin zone. K-Path ( $\Gamma \rightarrow X \rightarrow U \rightarrow K \rightarrow \Gamma \rightarrow L \rightarrow W \rightarrow X$ from SeeK-Path[108]. . . . .	74
2.5	Schematic of the wavefunctions and potentials of both the all-electron and pseudopotential[111], above the cutoff radius $r_c$ the wavefunction and potentials match. . . . .	76
2.6	Flow chart of the process of taking raw data through DFT to the completed structural analysis of ground state structures. . . . .	82
3.1	Low-symmetry $I4/mmm$ phase which shows clearly the Jahn-Teller like effect in the $A_2Au_2X_6$ structure with a rock-salt like ordering of the square-planar and octahedral geometries. . . . .	87
3.2	Schematic of the field splitting from the octahedral ( $O_h$ ) geometry to the square-planar ( $D_{4h}$ ), clearly showing the destabilisation of the $d_{x^2-y^2}$ orbital. . . . .	88
3.3	Phonon dispersion of the $CsAu_3$ structure. A 2x2x2 supercell was used to highlight the key symmetry points R, X and M. . . . .	90
3.4	The $Cs_2Au_2I_6$ structure ( <i>left</i> ) with all of the atoms included and ( <i>right</i> ) with the atoms removed for clarity on the octahedral structure (where the A-site cation caesium is represented by blue. The purple anions are represented by iodine and the gold cations sit within the gold octahedral cages). . . . .	91
3.5	Volume-Energy curve of the $Cs_2Au_2I_6$ $I4/mmm$ phase which is fitted to Murnaghan equation of state. The optimal volume of our structure is displayed above as $V_0$ . . . . .	92
3.6	Phonon dispersion curve for the $Rb_2Au_2I_6$ structure showing clear instabilities present in the structure - Instabilities with the corresponding irreducible representations are shown in Table 3.2. Structurally due to size of the crystal itself the phonons are all at the $\Gamma$ point. . . . .	96

<i>List of Figures</i>	19
3.7 Schematic of the $\text{Rb}_2\text{Au}_2\text{I}_6$ $C2/m$ phase showing the tilt distortions present. The A-site pink cations represent the Rubidium, the X-site purple anions represent the iodine and the B-site gold cations are found inside the gold octahedral cage. . . . .	97
3.8 Schematic of the $\text{K}_2\text{Au}_2\text{I}_6$ structure with the very clear anti-polar and tilt distortions present. Analysis of the modes shows the appearance of two tilt distortions. . . . .	99
3.9 Basic phase schematic for the Gold double perovskite-like structures . . . .	101
3.10 The change in the energy landscape as the the size of the polar distortion is varied. The bottom of the double well is characterised by the real distortion size of the $\Gamma_4^-$ mode. . . . .	103
3.11 Contribution to the lowering of the energy through both the hydrostatic and tetragonal strain. . . . .	104
4.1 Incremental increase of the size of the Jahn-Teller ( $R_3^-$ ) (25%, 50%, 75% of the maximum value found in the ground state structure) distortion for the $\text{Cs}_2\text{Au}_2\text{I}_6$ and the overall effect on the bandstructure. . . . .	115
4.2 Increase in the size of the Breathing ( $R_2^-$ ) (25%, 50%, 75% of the maximum value found in the ground state structure) distortion for the $\text{Cs}_2\text{Au}_2\text{I}_6$ with the overall effects on the bandstructure. The bandstructures shown here show a small increase in the size of the gap as shown by Table 4.1. . . . .	116
4.3 Band-Gap for the groundstate $\text{Cs}_2\text{Au}_2\text{I}_6$ structure. As described by Debichichi <i>et al.</i> [106], the formation of an <i>intermediate band</i> (IB) forms between both the conduction band (CB) and the valence band (VB) at approximately 0.7-1.5eV. . . . .	117
4.4 Density of states for the $\text{Cs}_2\text{Au}_2\text{I}_6$ $I4/mmm$ structure. (a) Density of States looking exclusively at the Au- $d$ $d^8$ alongside the I- $p$ states. (b) Density of states looking exclusively at the Au- $d$ $d^{10}$ sites alongside the I- $p$ states. . . .	118

4.5	Bandstructure for the $\text{Rb}_2\text{Au}_2\text{I}_6$ $I4/mmm$ phase. We see a similar shape to the caesium counterpart but with the gap bigger due to the increase in both the breathing and Jahn-Teller distortions. . . . .	120
4.6	Bandstructure for the $\text{Rb}_2\text{Au}_2\text{I}_6$ $C2/m$ phase. We see more flattening of the bands in the tilted low symmetry phase which opens up the gap. . . . .	121
4.7	Bandstructure for the $I4/mmmm$ $\text{K}_2\text{Au}_2\text{I}_6$ phase. The bandstructure looks similar to all of the other $I4/mmm$ phases, with small changes in the gap due to chemical substitution. . . . .	124
4.8	Bandstructure for the low symmetry $P2_1/c$ $\text{K}_2\text{Au}_2\text{I}_6$ phase. All of the bands appear more flat due to the two tilts that appear in the low symmetry structure, subsequently reducing Au-I-Au orbital overlap and reducing the bandwidth. Indirect band-gap of 1.22eV between the $C2-Y2$ point and the $\Gamma$ point. . . . .	124
4.9	Absorption of all three caesium compounds across a range of 12eV (100nm) and a focused area which looks at the areas from around the bandgap onwards. All of which are based on the $I4/mmm$ bandstructure displayed in Figure 4.3 . . . . .	126
4.10	Absorption of the three ground state Iodine structures, Cs ( $I4/mmm$ ), Rb( $C2/m$ ) and the K( $P2_1/c$ ). . . . .	127
4.11	The effect of hydrostatic pressure on the size of the $R_2^-$ breathing distortion and the $R_3^-$ Jahn-Teller distortion showing a steep reduction that occurs between 0 to 5GPa and the following measurements shown an almost 0 amplitude for the size of the breathing distortion from 10GPa onwards. . .	128
4.12	The effects of hydrostatic pressure on three distortions of interest in the $\text{Rb}_2\text{Au}_2\text{I}_6$ . The Tilt distortion, polar distortion and anti-polar distortion. . .	129
4.13	Size of the ionic contribution to the dielectric constant in the $zz$ direction with respect to the volume of the unit cell in the $\text{Rb}_2\text{Au}_2\text{Br}_6$ . . . . .	131
4.14	Graphic displaying the dielectric constant with respect to a phase diagram. The volumes were taken from the ground state volumes for the $\text{Rb}_2\text{Au}_2\text{Br}_6$ structure. . . . .	131

<i>List of Figures</i>	21
5.1	141
5.2	141
5.3	145
5.4	146
5.5	147
5.6	151
5.7	152
5.8	153
A.1	190

- B.1 Density of states of the  $\text{Rb}_2\text{Au}_2\text{I}_6$  I4/mmm structure. The top figure includes the Gold atoms in which there electrons sit within the  $d_{z^2}$  orbital and bottom figure includes the gold atom where the electrons sit within the  $d_{x^2-y^2}$  orbital. . . . . 194
- B.2 Density of states of the  $\text{Rb}_2\text{Au}_2\text{I}_6$  C2/m structure. The top figure includes the Gold atoms in which there electrons sit within the  $d_{z^2}$  orbital and bottom figure includes the gold atom where the electrons sit within the  $d_{x^2-y^2}$  orbital. . . . . 195
- B.3 Density of states of the  $\text{K}_2\text{Au}_2\text{I}_6$  I4/mmm structure. The top figure includes the Gold atoms in which there electrons sit within the  $d_{z^2}$  orbital and bottom figure includes the gold atom where the electrons sit within the  $d_{x^2-y^2}$  orbital. . . . . 196
- B.4 Density of states of the  $\text{Rb}_2\text{Au}_2\text{I}_6$  P2<sub>1</sub>/c structure. The top figure includes the Gold atoms in which there electrons sit within the  $d_{z^2}$  orbital and bottom figure includes the gold atom where the electrons sit within the  $d_{x^2-y^2}$  orbital. . . . . 197

# List of Tables

1.1	Atomic positions of the cubic $Pm\bar{3}m$ SrTiO <sub>3</sub> structure. . . . .	42
2.1	The 7 lattice systems and subsequent 14 Bravais lattice can be used to describe the symmetry of the crystal. . . . .	72
3.1	The effects of ion size on the the size of the Jahn-Teller and breathing distortions with respect to the cubic $Pm\bar{3}m$ . All Irreps are with with respect to the cubic $Pm\bar{3}m$ with the A-site cation at the origin. . . . .	94
3.2	Information on each phonon instability that is found in $I4/mmm$ Rb <sub>2</sub> Au <sub>2</sub> I <sub>6</sub> phase. All Irreps are with with respect to the cubic $Pm\bar{3}m$ with the A-site cation at the origin. . . . .	95
3.3	Irrep decomposition of the $C2/m$ Rb <sub>2</sub> Au <sub>2</sub> I <sub>6</sub> phase with respect to the cubic $Pm\bar{3}m$ (A-site cation at the origin) phase shows two extra distortions present. . . . .	97
3.4	Irrep decomposition of the $P2_1/c$ K <sub>2</sub> Au <sub>2</sub> I <sub>6</sub> phase with respect to the cubic $Pm\bar{3}m$ (A-site cation at the origin). . . . .	100
4.1	The increase in the gap for the breathing distortion is not insignificant but we do see an overall phase change with the Jahn-Teller. . . . .	113
4.2	Expansion of Table 3.4 with the inclusion of the optical band gap. The gap is influenced based on the size of the Breathing and Jahn-Teller distortions. . . . .	119

4.3	Band-gap changes based on the systematic change in the size of the anti polar ( $R_4^-$ ) distortion and the tilt ( $R_5^-$ ) distortion. . . . .	122
4.4	Effective masses of the charge carriers in the $Rb_2Au_2I_6$ $I4/mmm$ phase. from the $N \rightarrow \Gamma$ point. . . . .	122
4.5	Effective masses of the charge carriers in the $C2/m$ phase with the effective masses of the electron holes between the D2-A point and the effective masses of electron at the Y2 point. . . . .	122
4.6	Effective masses of the charge carriers from the high-symmetry $I4/mmm$ phase of the $K_2Au_2I_6$ with both the electron hole and electron effective masses appearing between $N \rightarrow \Gamma$ . . . . .	125
4.7	Effective masses of the charge carriers for the ground state low-symmetry structure of the $P2_1/c$ between the C2-Y2 for the holes and the $\Gamma$ for the electrons. . . . .	125
4.8	Dielectric response in the $xx$ , $yy$ , and $zz$ directions for the Cs compounds and the highest tolerance factor Rb in the $I4/mmm$ space group. We see a slow increase as the phonon distortion reduces in frequency (See the dielectric phonon tables in Appendix B). . . . .	130
5.1	Representation and magnitude of distortions from the $CsPbI_3$ high symmetry cubic $Pm\bar{3}m$ to the low-symmetry $Pnma$ structure. . . . .	144
5.2	Changes in band-gap for both the $I4/mmm$ and $Cmc2_1$ Ruddlesden-Popper phases with varying chemistry. Amplitudes are described for the phase transition $Pm\bar{3}m \rightarrow Cmc2_1$ . . . . .	148
B.1	Dielectric response to phonons for the $Cs_2Au_2Cl_6$ . . . . .	211
B.2	Dielectric response to phonons for the $Cs_2Au_2Br_6$ . . . . .	212
B.3	Dielectric response to phonons for the $Cs_2Au_2I_6$ . . . . .	213
B.4	Dielectric response to phonons in the $Rb_2Au_2Cl_6$ . . . . .	214

# Introduction

*"Nobody gets beyond a petroleum economy. Not while there's petroleum there."*

- Dan Simmons

**M**ore than ever there needs to be a change to how our world works. With exponential growth of humans across the world and a world population of 9.7 billion expected in 2050[1] *and* a real over reliance on fossil fuels (see Figure 1.2 and Figure 1.3), now more than ever do we need to start shifting to a more sustainable future.

The two figures from Our World in Data show explicitly how fossil fuels dominate the energy production of the world. It has unfortunately lead itself to destruction of habitats and what is accepted as scientists as the slow warming of the planet. Data from Jouzel *et al.* show the correlation between the CO<sub>2</sub> content of the atmosphere and the temperature as shown in figure 1.1[2]. What is clear is there needs to be a

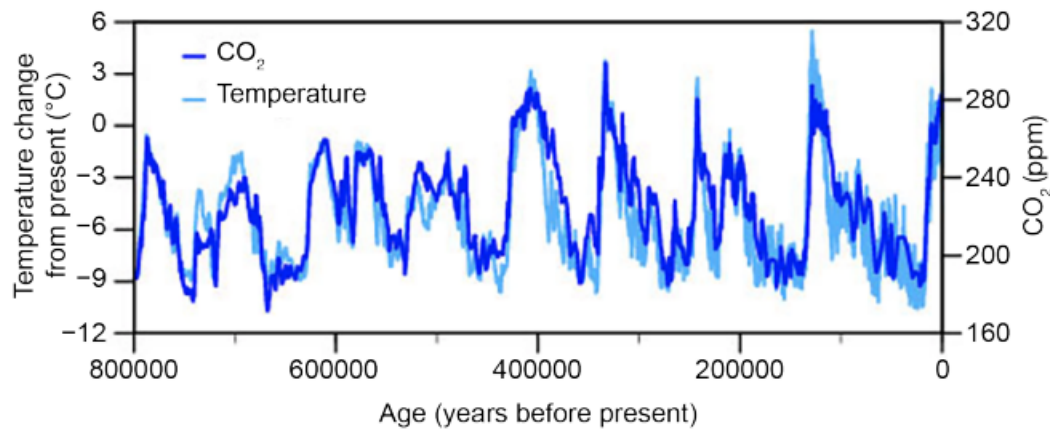


Figure 1.1: The correlation between the temperature change of the atmosphere in comparison to today's temperature and the amount of CO<sub>2</sub> in the atmosphere in PPM.

reduction in overall emissions of CO<sub>2</sub> in the atmosphere. There has been a general geopolitical effort to limit the emission of CO<sub>2</sub> through several 'conventions'. The two which stand out are the Kyoto Protocol which was adopted on the 11 December 1997 and entered force in 2005. There are currently 192 signatories to the Kyoto principle[4]. The second 'convention' that looked to secure a reduction in the overall emissions of CO<sub>2</sub> is the Paris climate agreement in Dec 2015, which was adopted by 195 countries with the aim of limiting temperatures to 2°C to pre-industrial levels,

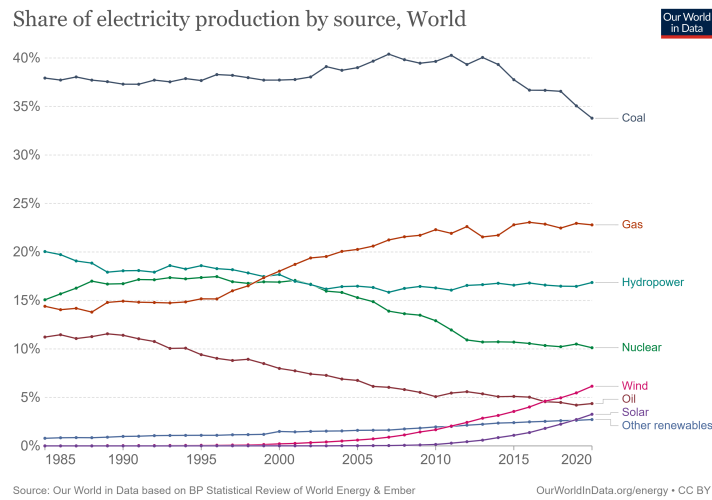


Figure 1.2: The share of electricity from different sources for the world. What we see is a *slow* decline in the use of fossil fuels but overall there is still a massive over reliance on coal. Generally across the world we see a more of reduction in the use of coal, but an increase in either oil or gas. Figure from [3].

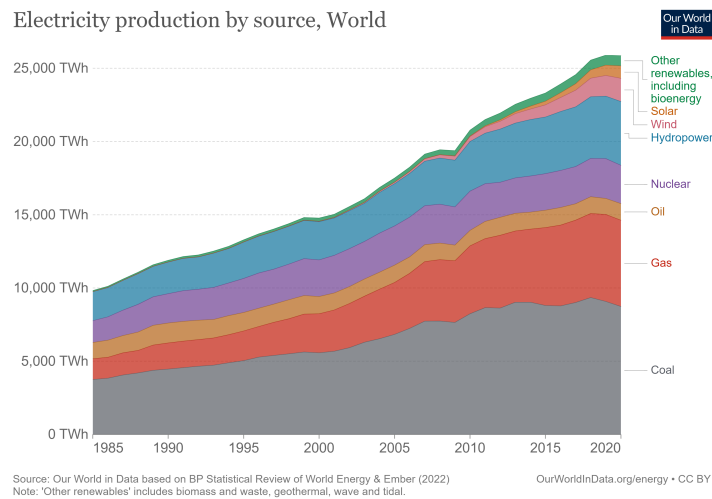


Figure 1.3: This graphic from Our World in Data shows explicitly that even though there has been reductions in the overall percentage of fossil fuels being burnt for fuel, the overall percentage is a constant increase in the amount that is being burnt due to the overall increase in human population on the Earth. Figure from [3].

which would require a carbon-neutral economy of the world by 2050[5]. Therefore there needs to be a shift of our energy production to more long-term sustainable renewable energy sources.

## 1.1 Photovoltaic History and Function

Solar power is one such renewable source that could be continued to secure the long-term energy needs of humankind. The power radiated by the sun is approximately  $3.86 \times 10^{26}$  W. In approximately 80 minutes energy from the sun equivalent to the total world energy use for a full year will radiate on the Earth, this estimates that approximately 7000 times the worlds energy use is radiated every year. The potential energy extraction is huge and unfortunately there are large economic, geopolitical and technological challenges ahead. Of course here we are going to focus on the technological challenges that face the extraction of energy from sunlight. The original idea of photovoltaics came from the photovoltaics effect where Alexandre-Edmond Becquerel observed that metal electrodes in an electrolyte solution produced small currents when light was shone onto it. He however could not explain this effect[6]. The late 1800s and early 1900s lead to huge developments in the area of the photoelectric effect and photovoltaics with a couple patents being taken out under the names of *solar cell*, *solar storage* patent numbers US527377A and US598177 respectively. The 1900s lead to the explanation of the photoelectric effect on a quantum basis by Albert Einstein. Einstein published *Über einen die Erzeugung und Verwandlung des Lichtes betreffenden heuristischen Gesichtspunkt* which translates to *On a Heuristic Viewpoint Concerning the Production and Transformation of Light* in 1905 which lead to the award of his Nobel prize in 1921. This understanding of the nature of light and its interaction with matter lead to a century of photovoltaic research which we take advantage of today. The first modern photovoltaic is generally considered to be a *p-n* junction silicon solar cell developed by Chapin *et al.*, with the first silicon solar cells being approximately 6% efficient[7].

Initially they were difficult to commercialise due to their extremely large cost but were

eventually and commonly used to power satellites. The principles of these solar cells work by a singular photon interacting with an electron in the valence band, this raises the electron to the conduction band where it is free to move under an external electric field. This electric field comes from the presence of the  $p-n$  junction (more about this later). The issues we have with photovoltaics is the arbitrary low efficiencies that we see with them for generally quite a high cost, therefore a lot of research over the past 10-20 years has gone into finding a cheaper and easier to make photovoltaic device with a relatively high Power conversion efficiency (PCE). As defined in the discussion of photovoltaics the power conversion efficiency is the ratio of the output power over the input power. Figure 1.4 shows the different types of solar cells that have been built from 1975 to 2020. The efficiency of photovoltaic solar cells vary depending on the way in which they are built. The current highest efficiency photovoltaic that has been produced is a four-junction III-V semiconductor. III-V semiconductors are an alloy of group 3 and group 5 elements, examples include GaAs[9], GaN[10] and InN[11]. This four-junction solar cell has a peak efficiency of 46%. This high level of efficiency comes from the absorption across a very large range of wavelengths (300-1750nm)[12]. One of the issues we have in using four-junction solar cells is the very large cost that is associated with the engineering of one. Therefore as mentioned before what we are looking for is a cheap alternative with a relatively large PCE.

This leads us on to promising photovoltaic cells that we are going to examine in this thesis, perovskite solar cells. Perovskite solar cells have only been examined for just over a decade and has become a promising photovoltaic due to its astronomical rise in PCE in such a short amount of time (see yellow circle with red outline on the NREL chart). One of the first perovskite solar cells, a organometal  $\text{CH}_3\text{NH}_3\text{Pb}(\text{Br},\text{I})_3$  registered a 3.8% efficiency[13]. From here there has been an acceleration in the different perovskite solar cells created, both organic and inorganic. The first fully inorganic perovskite solar cell was created in 2012 with a PCE of 0.88%[14] with a rapid increase in the PCE for halide inorganic perovskites as shown in Figure 1.5. The exciting point about perovskite solar cells is both the rapid increase in PCE and the extremely cheap production cost with production cost coming down to £0.18 per square foot[16] in

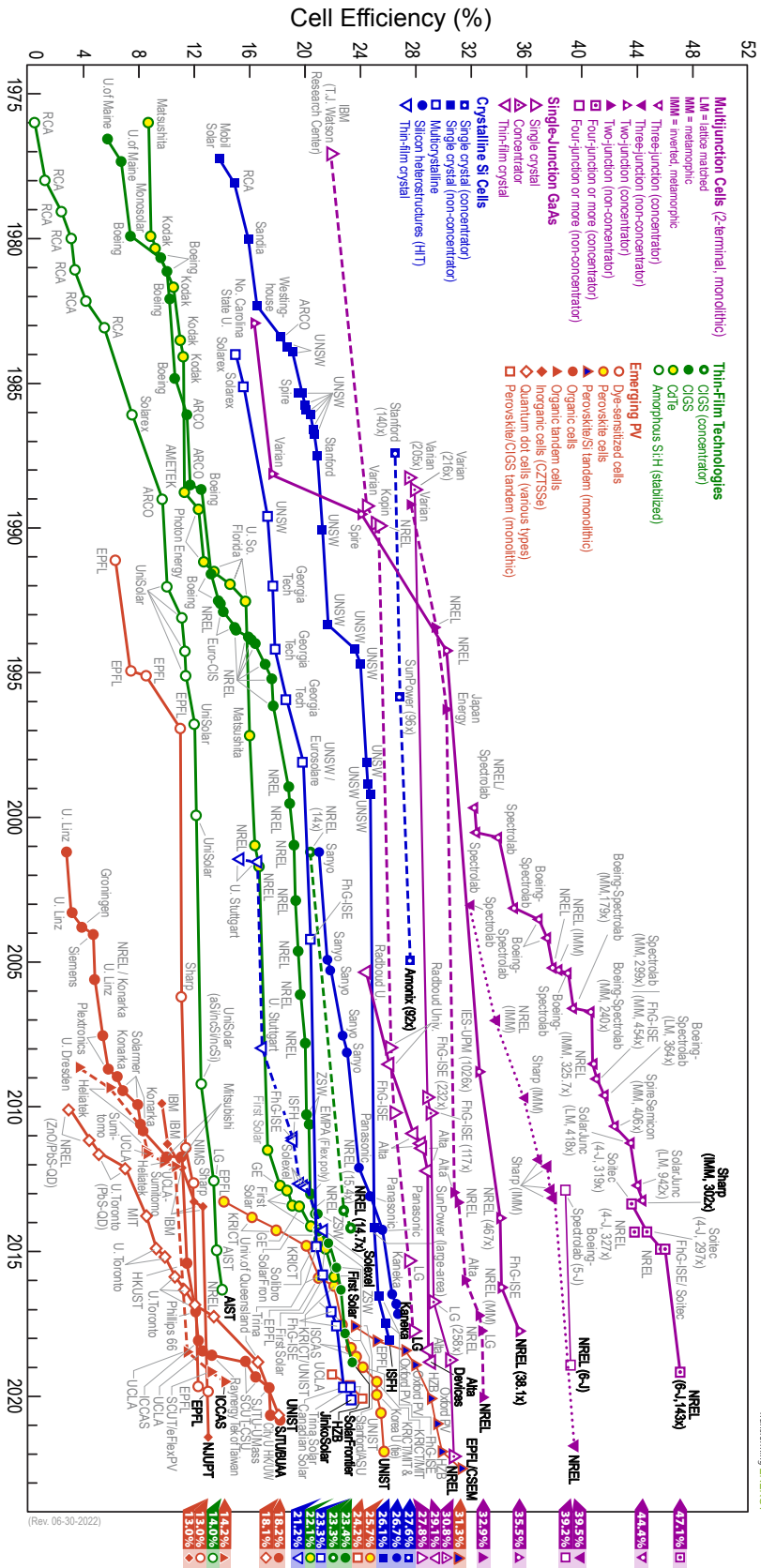


Figure 1.4: NREL summary of the different photovoltaic cells that have been produced through time with the associated efficiencies[8].

52 **Best Research-Cell Efficiencies**



Transforming ENERGY

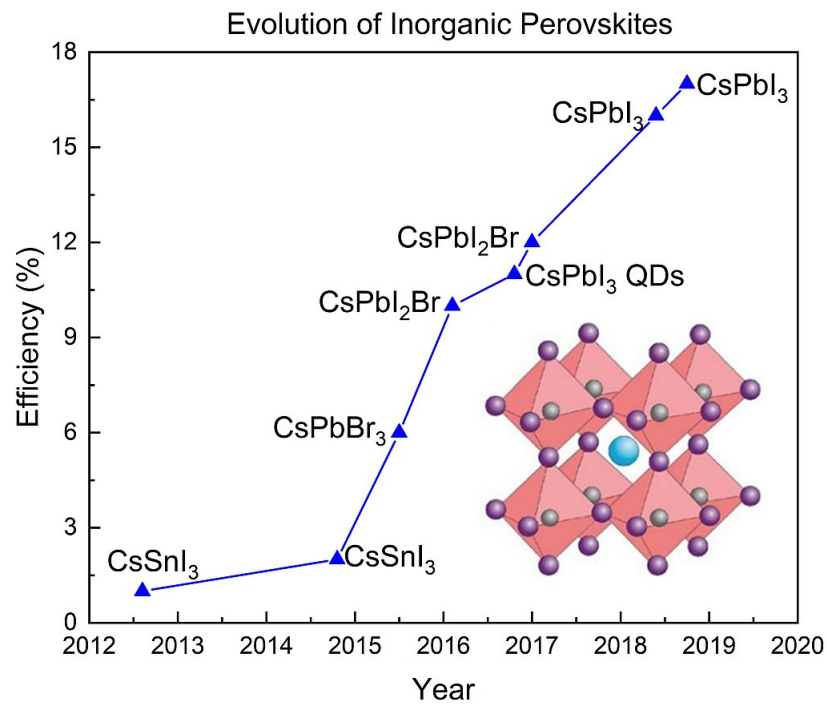


Figure 1.5: Evolution of the PCE of inorganic halide solar cells from the original CsSnI<sub>3</sub> up to the more recent CsPbI<sub>3</sub>. Figure from [15].

comparison to silicon. Perovskite solar cells have seen an improvement of approximately 20% increase from 3 to 23% over the space of a 4 year period[17] whereas silicon solar cells have seen a similar increase across the approximately 60 years that we have been studying them. Perovskite solar cells do however come with their own challenges:

1. the stability of perovskite solar cells. This has become a whole branch of research in itself and something we will not explicitly address in this thesis. Perovskite solar cells are known to degrade quickly and do not have particularly long lives. This degradation can happen under many conditions including moisture, oxygen, temperature and even quite *ironically* light[18, 19, 20, 21].
2. Material toxicity is a current issue with perovskite solar cells. A lot of the cur-

rent materials that have significantly higher PCE's have lead at the heart of the structure. This leads to some possible environmental problems with perovskite solar cells[22]

3. The hysteresis effect of photovoltaics. This effect can lead to over-inflated values of the PCE[23] due to the fact hysteresis affects the values of the open-circuit voltage and the short-circuit current density. The effect of hysteresis can also severely hamper the operational stability of the device[23].

These types of challenges are ones that are currently attempting to be addressed. We will briefly discuss challenge two throughout this thesis and was one of the reasoning in our review focusing on the changes in chemistry.

## 1.2 Solar Cells

In this section we will discuss more widely the physics and understanding of solar cells themselves. This leads into what specifically it is we are looking for when we explore the application of perovskites as solar cells later on. So what is a solar cell? A solar cell is a device that converts solar radiation into electricity. Currently solar cells are becoming more prominent over the world and even in the UK, there is however some push back due to their high carbon cost and general unreliability. Photovoltaic technology works on the premise of taking advantage of the quantum mechanical particle nature of light and the photoelectric effect which allows for the excitation of electrons to higher energy states[24]. Solar cells work on the premise of having an insulating material with a smaller gap where electrons can be excited to a higher energy state through small energy fluctuations (for solar cells, that energy fluctuation is light).

### Semiconductors and The Photovoltaic Effect

The general electronic structure is based on the premise of two types of bands. A *valence band* is the band of electron orbitals that electrons can move out of when

excited, these bands are completely occupied in the low energy state. It is generally the outermost electron orbital of an atom. The *conduction band* is the area in which electrons are free to move between different atoms, they are said to have undergone conduction which is where electrical power is transferred. Figure 1.6 shows the three<sup>1</sup> main types of materials electronic bandstructure. As shown in figure 1.6 different

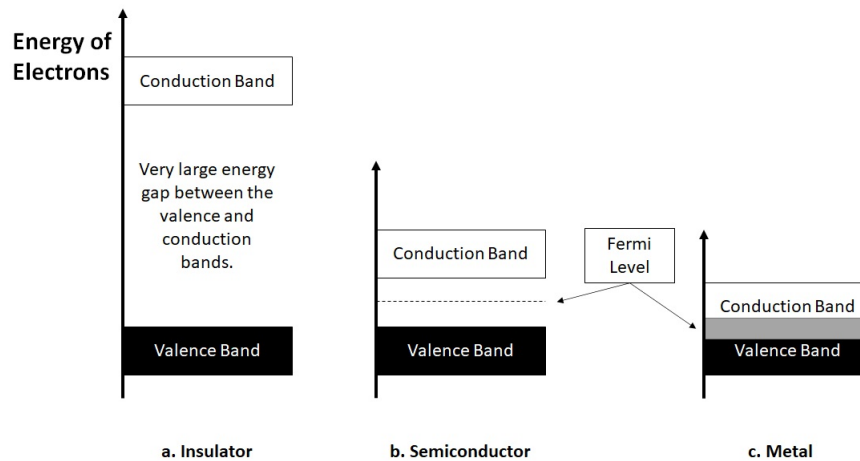


Figure 1.6: Basic description of a) an insulator b) a semiconductor and c) a metal.

materials will have altering electronic properties that are based on the organisation of the electronic bands in the material:

1. **Insulator:** An insulating material is one in which no/very small electrical current will flow. A prime example of an insulator is glass, glass is completely transparent to light due to the fact that none is absorbed through the material and no electrons are moved between the bands due to the band-gap being large, this is however only true for non-defective materials. Defective materials are not reliant on the valence and conduction band for charge transfer. Doping of glass with impurities can change the colour of the glass, this therefore would

<sup>1</sup>We generally think of the electronic properties falling into three distinct categories as mentioned above in which one is a metal but we can also see the electronic properties of a material fall into two other categories the semi-metal (a very small overlap of the VB and CB) and the half-metal (Where conduction only occurs with electrons of one spin orientation).

lead to a particular change in the band energy levels (more on doping later), the VB is completely filled which makes the system *inert*, in which the electrons are fixed and cannot be mobile throughout the system.

2. **Semiconductors:** Materials in which the difference between the conduction band (CB) and valence band (VB) is in between that of both an insulator and metal. Generally semiconductors fall into two categories. A wide-gap semiconductor in which the gap is usually above approximately 1.5eV. These semiconductors are more likely to work at much higher voltages. For smaller gap semiconductors (0.8-1.5eV range) Small fluctuations in the energy can lead to excitation to the CB, this can include a change in temperature for example a thermistor or the presence of light (Light dependent resistors, photovoltaics).
3. **Metals:** Metals are materials where the VB and CB completely overlap. In this case the electrons occupy both the VB and CB but both bands are partially filled, this leads to the ability for the charge carriers to be mobile through the structure.
4. **Fermi-Level:** In solid-state physics and when we analyse structures in DFT the fermi-level is the highest occupied energy level of a material at 0 degrees kelvin. I mention DFT as this *ab-initio* method is a ground-state (0k) theory.

Of course in reality the bands in a material are not simple rectangles but a full structure which maps out the allowed and forbidden energies for electrons in the material. Isolated atoms have electrons that can sit in discrete energy levels and are free to move between these energy levels when the energy is sufficient. When two or more atoms are bonded together their atomic orbitals will overlap or *hybridise*, creating new orbitals with different shapes and energies. Due to the sheer amount of atoms that are found in a crystal we find that a lot of the energy levels begin to coalesce to form a long energy band. Generally the valence bands we see in our bandstructures are based on the *valence* electrons (the outermost electrons used for bonding and conductivity). Inner electrons are generally not part of the conduction process due to

the bands not overlapping significantly. Band theory is an excellent tool in allowing us to determine some of the key electronic properties that materials have. Band-structures can generally have lots of band gaps throughout the material and when we describe *the* band-gap it is associated with gap between the valence band maximum and conduction band minimum and is usually wraps the Fermi level. The main focus of this review is of course the semiconductors. The basics of the description of semiconductors is found above but there are multiple aspects to which semiconductors are structured.

We can describe semiconductors in two types both an *intrinsic*-semiconductor, where the number of excited electrons is equal to the number of electron-holes and an *extrinsic*-semiconductor, which is doped by an external source. Doping is the process in which impurities are intentionally introduced into the material with the desired effect to change the electronic properties of the material. The photovoltaic effect arises from the excitation of electrons from the VB to the CB through a band-gap value which has a distinct energy value. This energy value can change material to material but is also based on the impurities in such a material. A distinct photon with energy equal to the band-gap will allow an electron to move up to the CB. This leaves behind a positively charged space, we designate this name as an *electron-hole*. An electron-hole acts as a positively charged carrier which can also move freely amongst the VB, through an electron taking its place and leaving behind another electron-hole.

Figure 1.7 shows a basic schematic of how an excitation can occur in a semi-conductor material. If the energy is sufficient for the electron to move through the forbidden region then the electron can move up to the conduction band and move freely between the different atoms, allowing for conduction. Electrons that are excited above the conduction band edge will lose their energy as they relax back to the edge of the conduction band, these electrons are termed *hot electrons* due to the loss of energy through thermal radiation. The band-gap is one of the most vital parts of the photovoltaic effect and a focus of this thesis. One of the benefits of perovskite solar cells is the complete versatility in adjusting the gap which makes them excellent candidates for this study.

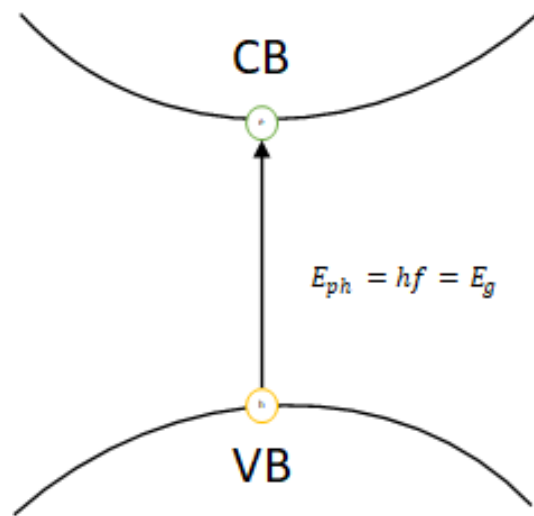


Figure 1.7: Simple schematic of the excitation of an electron from the valence band (VB) to the conduction band (CB).

Absorption of light is another central focus to the study of photovoltaics, light is not always emitted in singular wavelength photons (like a laser) but a wide spectrum of different energies, the spectrum of visible light. The spectrum that is used to compare between semiconductors is the AM 1.5 spectral irradiance[25] and is used to compare the effects of different photovoltaic devices. This model is commonly used as a spectrum which models the solar irradiance effectively and is vital in understanding the optimisation of band-gaps. Band-gaps have been important to the photovoltaic field for an extremely long time and one of the most referenced pieces of literature in the field is based on the Shockley-Queisser limit of efficiency. The Shockley-Queisser limit states that the efficiency of a single  $p$ - $n$  junction solar cell cannot exceed (under the 1.5 AM spectrum) 33.7% for a band-gap of approximately 1.4eV[26]. Solar cell efficiency loss is inevitable due to the electronic structure of the materials. We find that some of the light is reflected from the surface of the material and even when absorption occurs energy can be lost through heat. This occurs when the energy of the photon is much greater than the band-gap, in which electrons that have become

excited above and beyond the CBM will relax and lose energy to the energy as they move towards the edges. Energy can also be lost when the electron-hole recombination can occur. This allows us to aim for a particular band-gap when we are examining our perovskite solar cells. Shockley and Quessier made explicit reference to a  $p-n$  junction. This junction is created through the combination of two different types of doped semiconductor.

Doping is an effective method to increase the number of charge carriers within a material (the number of electrons or electron-holes). For traditional semiconductors doping creates N-type material when a group IV semiconductor material is doped with group V atoms and P-type is created when the same group IV materials are doped with group III elements. N-type materials increases the number of negative charge carriers and P-type increases the number of positive charge carriers.

Combining these two together creates a  $p-n$  junction. This junction's role is to separate the electron and hole carriers in a solar cell. There are several other ways to separate charges including selective contacts[27] or a combination of metal-insulator-semiconductor solar cells[28] where the use of an extremely thin insulator can allow measureable currents to tunnel between the semiconductor and metal layers. In the case of solar cells  $p-n$  junctions are the most widely used so will be examined here in the introduction. It is important to note that further in the thesis we move away from the idea of  $p-n$  junctions due to the exclusive way perovskites carry out charge separation. Development of such a junction requires the doping of acceptor atoms within the p-type region of the semiconductor and doping of donor atoms within the n-type atoms. These dopant atoms manipulate the band edges of both the p-type and n-type semiconductors to produce a voltage across the region between them. This is shown in Figure 1.9,

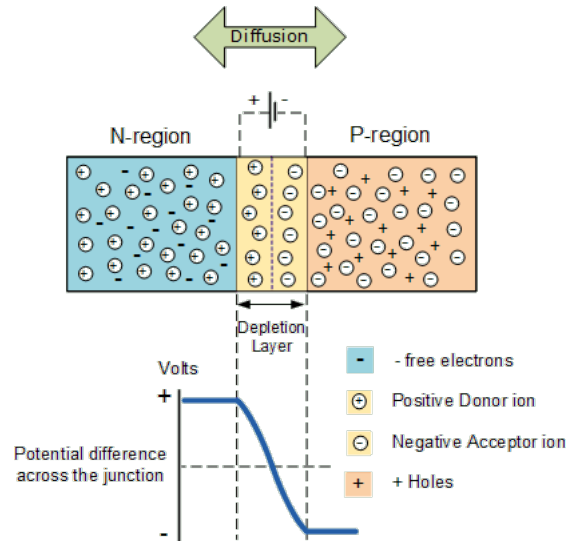


Figure 1.8: Schematic of a *p-n* junction showing the depletion zone and the formation of the electric field across the junction. This allows for the charges to be separated when excitation occurs. Schematic from [29]

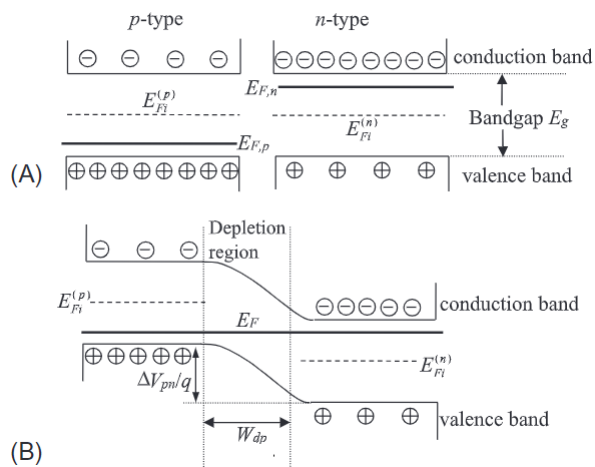


Figure 1.9: A) Energy band diagrams of p-type and n-type semiconductors. B) The energy diagram of a pn-junction which is in equilibrium. Similar to figure 1.8 we can see a potential barrier appear between the two types of semiconductor. Figure from [30].

Where, the  $E_{Fi}^{n,p}$  is the fermi level for the intrinsic semiconductor,  $E_{F,p}$  and  $E_{F,n}$  are the fermi levels for the associated semiconductors,  $W_{dp}$  is the width of the depletion region and finally  $\Delta V_{pn}/q$  is the potential barrier across the pn-junction. Because of the strong electric field in the depletion region, there are no free electrons or holes. If light with sufficiently high enough energy is shone onto the material we see the separation of an electron-hole pair within the depletion region, there then is migration of the electrons to the right and the holes to the left with a photocurrent being produced. Figure 1.8 shows the basic schematic of a  $p$ - $n$  junction. This junction provides the opportunity for charge carriers to be separated.

Operation of a solar cell allows us to measure certain characteristics that allow us to understand the electrical properties of such photovoltaic devices. They can include:

- The open-circuit voltage ( $V_{OC}$ ): The voltage that occurs under illumination when there is no metallic contact between the two ends of the junction of the solar cell.
- Short-circuit current density ( $J_{SC}$ ): The current density that flows through between the two terminals of the photovoltaic cell when the resistance is zero (also defined as when the voltage between the two ends of the junction is zero).
- The operational voltage and operational current ( $V_{MPP}$ ,  $J_{MPP}$ ): The voltage and current density generated by the solar cell when it is operating at its maximum power output.
- Fill factor ( $FF$ ): The ratio of the power generated by the solar cell and the maximum theoretical power that can be generated from the  $J_{SC}$  and  $V_{OC}$ .

$$FF = \frac{J_{MPP}V_{MPP}}{J_{SC}V_{OC}} \quad (1.2.1)$$

- Efficiency ( $\eta$ ): is the percentage ratio of the operating power of the solar cell and the theoretical maximum power of the solar cell. This can be calculated using the

parameters discussed here or by measuring both the input power and output power of the solar cell.

$$\eta = \frac{J_{MPP} V_{MPP}}{P_L} = \frac{J_{SC} V_{OC} FF}{P_L} \quad (1.2.2)$$

where  $P_L$  is the power of the light that is being shone onto the surface of the solar cell.

Figure 1.10 shows the how each of these characteristics interact with each other. This

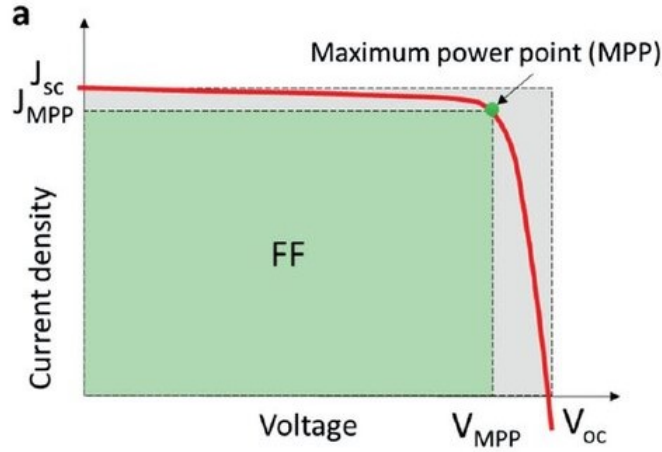


Figure 1.10: Basic JV curve which shows the different characteristics of a photovoltaic device ( $V_{OC}$ ,  $J_{SC}$ ,  $FF$ ,  $P_{MPP}$ .), Figure from [31]

line of this graph is obtained from the following[32]

$$I = I_L - I_0 \left[ \exp\left(\frac{qV}{nkT}\right) \right], \quad (1.2.3)$$

where  $V$ , is the solar cell forward voltage,  $q$  is the electron charge,  $n$  is the intrinsic charge density,  $k$  is Boltzmann's constant,  $T$  is the absolute temperature,  $I_L$  is the light generated current and  $I_0$  is the dark generated current. These quantities become important for the comparison of the solar cells, not only between the different compositions but between the theoretical and operational results that can be extracted. We will not explicitly be analysing the effects of these measurable parameters of solar

cells but they may be discussed when looking at the literature surrounding each of the systems that we will be analysing in this thesis.

### 1.3 Perovskites

We have touched upon the purpose of looking at perovskite solar cells. conventional silicon solar cells, which are currently commercially and widely available currently carry out a job particularly well. However, as previously mentioned silicon solar cells are limited in their power-conversion efficiency and come with an extremely high carbon cost. Although abundant and cheap to extract, the carbon cost of carrying out the raw-to-useable material is high with the average customer needing to have a solar cell running for approximately 3-4 years to pay back the carbon cost of producing it. This is also not taking into account the other rare-earth materials that are involved in manufacturing. Perovskite structures are based on the original perovskite  $\text{CaTiO}_3$  which was discovered by by Gustav Rose and named after the Russian mineralogist Lev Alekseevich Perovski [33]. The original structure follows the  $(\text{ABX}_3)$  and B-site cations can be substituted to give a variety of different physical and electronic properties, this provides perovskites and perovskite like materials with a wonderfully diverse portfolio of uses. The idealised perovskite structure is cubic in nature and is adopted by a large range of different perovskites. An example of a cubic  $Pm\bar{3}m$  is  $\text{SrTiO}_3$  (at  $T = 298\text{K}$ ) which follows the following:

$\text{SrTiO}_3$ ; cubic;  $a=0.3905\text{nm}$ ;  $Z=1$ ; space group:  $Pm\bar{3}m$  (No. 221)

Atom Label	No. of Atoms	Position
Sr	1	0, 0, 0
Ti	1	1/2, 1/2, 1/2
O	3	1/2, 1/2, 0; 1/2, 0, 1/2; 0, 1/2, 1/2

Table 1.1: Atomic positions of the cubic  $Pm\bar{3}m$   $\text{SrTiO}_3$  structure.

The interesting point of the perovskite structures is the corner sharing octahedra that are produced in its formation. If we think about our  $\text{SrTiO}_3$  structure then we have the formation of  $\text{TiO}_6$  octahedra with the Ti-cation placed in the centre of the *cage*. These octahedra are corner sharing with other octahedra and thus can rotate and tilt, this is

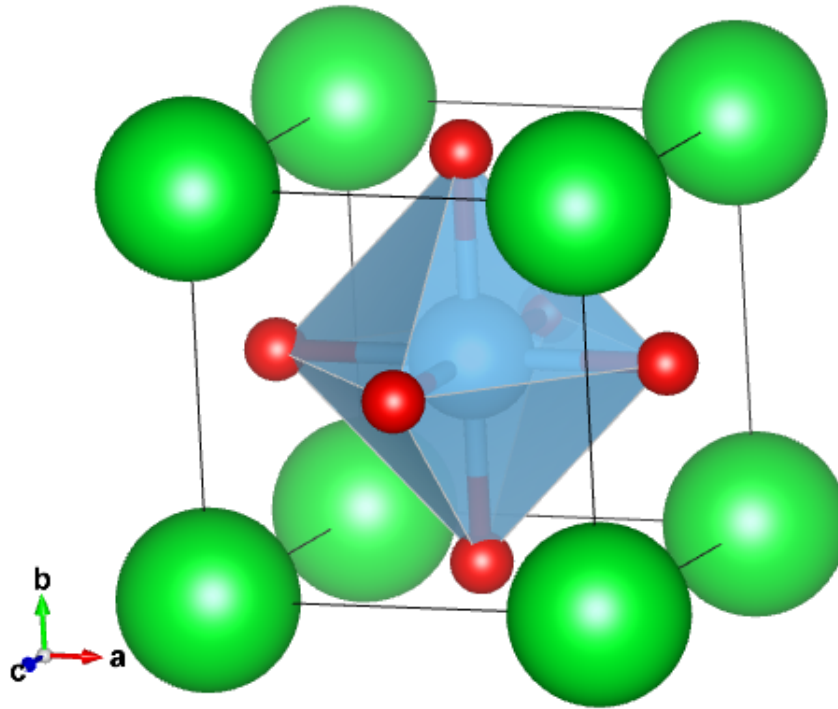


Figure 1.11: Structure of the  $\text{SrTiO}_3$  Perovskite which shows the corner sharing octahedra at the centre of the structure. The Strontium atoms surround the octahedra. Atomic positions from [34]

a vital part of the research that we have undertaken and it can wildly change the properties of the materials. Another aspect that can change the properties is the chemistry of the materials. Perovskites are also diverse in their ability to cater for both an inorganic and organic A-site cation for example methylammonium ( $\text{CH}_3\text{NH}_3$ ) or formamidinium ( $\text{CH}(\text{NH}_2)_2$ ). In this thesis we will be looking at exclusively metal-halide perovskites which follow the same stoichiometry but the X-site anion is a group VII element. Because our halide has an  $\text{X}^-$  oxidation state our cations will need a net charge of +3 and usually always follow the (+1,+2) valency state. In metal halide perovskites, the B-site cation is usually filled with a  $\text{Pb}^{2+}$  cation but as we show in Chap-

ter 5 this can be filled with  $\text{Sn}^{2+}$  [35, 36] and  $\text{Ge}^{2+}$  [37]. This is generally due to the instability of the material. As mentioned previously, the stability of inorganic perovskite materials is one of the challenges we currently face with degradation occurring almost instantly in some materials in certain conditions. Interestingly, a lot of the different tin and germanium perovskites that we see are paired with an organic A-site cation and there seems to be a real lack of inorganic metal halide compounds with tin and germanium. In chapter 3 we also look at a new and up and coming structure which has been in research recently with the B-site cation being Gold. In all of the chapters in this thesis the A-site cation will be a group I element mainly (Cs, Rb, K). Structurally we can determine how likely our system is to be perovskite by looking at the Goldschmidt tolerance factor [38]:

$$a = \sqrt{2}(R_a + R_x) = 2(R_b + R_x)$$

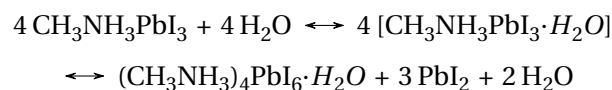
$$\tau = \frac{R_a + R_b}{\sqrt{2}(R_b + R_x)}, \quad (1.3.1)$$

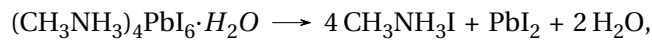
Where  $R_a$ ,  $R_b$  and  $R_x$  are the ionic radii of each atom. For the purpose of this thesis we used the Shannon ionic radii [39]. We have used the tolerance factor and the Shannon ionic radii as a method of comparison between different structures in this thesis with the radii of the halides being quite poor. The tolerance factor itself is a ratio of the ionic radii. The Goldschmidt tolerance factor is one of the ways in which we can predict certain sterical characteristics of perovskite materials. For example, if the tolerance factor is larger than 1 then we can see a tetragonal like structure examples include  $\text{BaTiO}_3$  [40]. This tolerance factor arises from the fact that either the A-site cation is too big or the B-site cation is too small. Usually for a tolerance factor slightly that are above this region will drive the appearance of a polar distortion. Generally, for tolerance factors of 0.9-1.0 we can see structures that are cubic, much like the aforementioned  $\text{SrTiO}_3$  mentioned previously. When the tolerance factor becomes considerably smaller we begin to see the appearance of tilted perovskite distortions. This arises due to the A ions being too small to fit within the spaces between the B-site regions in the structure. For example in the  $\text{Cs}_{1-x}\text{Rb}_x\text{Pb}(\text{Cl}, \text{Br})_3$  phases we see an increase in the size of the tilt distortion when the tolerance factor is decreased [41].

In this thesis we will be studying metal halide perovskites and these materials have a very brief but rich history, unlike conventional semiconductors like Si, GaAs, CdTe which are covalently bonded compounds halide perovskites are ionically bonded crystals. What this does allow is flexibility in the formulation of such a system with solid-solutions of various cations and anions that are created (See the  $\text{Cs}_{1-x}\text{Rb}_x\text{Pb}(\text{Cl}, \text{Br})_3$  above).

This allows for the tuning of optoelectronic properties of the materials to be done much easier and gives engineers and researchers the opportunity to apply a single system to multiple applications. For example in the organometal halide perovskite  $\text{HC}(\text{NH}_2)_2\text{PbBr}_{1-y}\text{I}_y$  where the mixture of iodine and bromine can lead to a change in the absorption edge across a variety of wavelengths (550nm for pure bromine to 850nm for pure iodine)[42]. It is not just anion mixing which has been shown to improve the optoelectronic properties of the material, A-site cation mixing has been shown to improve stability. For example the A-site cation mixture of  $\text{Cs}_{0.05}\text{FA}_{0.95}\text{PbI}_3$  shows resistance to degradation to moisture in comparison to pure  $\text{FAPbI}_3$ . This was then extended where Rb was used instead of Cs and the improvement in resistance to humidity improved significantly[43]. Mixing of both A- and X-site ions has shown to improve the PCE of perovskite solar cells quite significantly with  $\text{MA}_{0.17}\text{FA}_{0.83}\text{Pb}(\text{I}_{0.83}\text{Br}_{0.17})_3$  allowing a PCE of 21.2%. Not only did this improve the efficiency of the material in comparison to their non-mixed counterparts but the mixing of the A-site cation lead to improved stability with the solar cell operating stably for more than 1000 hours[44].

Although organometal halide perovskites show promise in terms of their PCE statistics, the organic cation is believed to be the leading issue with long-term stability and with a toxic substance like lead, stability is a real problem. Degradation of the perovskite solar cells can lead to the the formation of  $\text{PbI}_2$  and this is very common when exposed to moisture[45]:





Therefore there has been a lot of work being put into removing the A-site organic cation and looking for full inorganic. The group 1 elements are generally favoured for replacement of the organic cations (Cs, Rb, K), Rb and K compounds are currently in the realms of theoretical work with the CsPbI<sub>3</sub> compound having been explored quite rigorously. These materials do not come without their issues for example at room temperature the CsPbI<sub>3</sub> compound wants to relax into what's called the *yellow* phase ( $\delta$ -CsPbI<sub>3</sub>) which is orthorhombic and does not generally as photoactive as the cubic *black* phase ( $\alpha$ -CsPbI<sub>3</sub>). Issues of the black phases stability at room temperature has been attempted to be addressed with the introduction of MA or FA into the crystal structure which leads us back into the realms of low stability or substituting out the I with Cl or Br which leads to larger band-gaps which can be not suitable to optical light absorption[46, 47, 48].

As previously mentioned there is a huge amount of flexibility when it comes to perovskite structures in the variety of ions both organic and inorganic. Not only with the almost *swap out, swap in* idea with elements. *Theoretically* we can do this, by means of density functional theory or classical dynamics but we might not necessarily be able to create it in a lab. This chemical flexibility however does allow us to see a wide variety of different properties and there is a lot of work going into trying to enhance the chemical flexibility of perovskites even further[49]. Another flexibility is the steric flexibility that perovskites have, these can include several different steric changes of the atoms. Perovskites can be subject to all different types of steric changes based on physical chemical change to electronic substitution change. With some perovskites, more generally with the transition metal perovskites, different occupations of the *d*-orbitals can lead to the Jahn-Teller distortions[50, 51, 52], cation ordering[53, 54] or octahedral tilts[55]. This leads to an even larger variety of electronic properties and this is something we will explore over the next couple of chapters. In this little subsection we have explored some of the fantastic progress perovskites have made in the world of photovoltaics over the very brief but explosive 15

---

year history from the writing of this thesis. In this thesis however we will be exploring inorganic perovskite materials. In our first two results chapters we will be looking at a previously synthesised and more recently explored gold double perovskite structure. In the final chapter we will explore the optoelectronic and ferroelectric properties of Ruddlesden-Popper Layered  $\text{Cs}_3\text{Pb}_2\text{I}_7$ . There is exciting results to be explored for the gold double perovskites with a plethora of different distortions which are all inter-linked through a primary and secondary order parameter. It is however, an exciting time for the world of photovoltaic perovskites and we have seen huge amounts of research put forward for the development of these materials in the hope of soon to be commercialisation.

## 1.4 Ferroelectrics

Ferroelectricity is a physical property of a material that can occur in selected materials that is characterised by the spontaneous electric polarisation *without* the presence of an external electric field. Ferroelectric materials are a subclass of pyroelectric (materials that exhibit electric polarisation when the temperature changes) and piezoelectric materials (materials that exhibit electric polarisation under mechanical stress). All of these materials are under the umbrella term dielectrics (A material that can be polarised by an external electric field). Ferroelectric materials exhibit a switchable polarisation in the presence of an external electric field, something which is not attributed to other parent classes of polarisable materials. Ferroelectricity was discovered by J. Valasek in 1920 with his study on Rochelle salts[56], with many more materials having been discovered as ferroelectric recently.

The ferroelectricity that arises in crystals is due to the breaking of inversion symmetry in the crystal structure. This gives rise to a non-centrosymmetric system. Ferroelectricity is generally a displacive effect (but ferroelectricity can arise from molecular FE's whereby the dipolar molecules align) where ions in the unit cell of a material lead to an asymmetry in the electron density. Examples include the off-centering of the  $\text{Ti}^{4+}$  ion within the octahedral cage of the  $\text{BaTiO}_3$  which leads to the ferroelectric properties. This off-centering of the  $\text{Ti}^{4+}$  is driven by a pseudo second-order Jahn-Teller distortion[57], whereas in  $\text{PbTiO}_3$  ferroelectricity appears due to a lone pair of electrons within the structure. The reversible polarisation leads to the hysteresis properties of the material. Quite a large amount of polar structures of ferroelectric materials arise due to small external changes in a non-polar polymorphs. These changes could be strain, temperature, etc. Figure 1.12 shows the hysteresis of a ferroelectric material. Where,  $P_{\text{sat}}$  is the saturation polarisation, the maximum value for the polarisation that can be produced by the material,  $P_r$  is the remnant polarisation, the size of the polarisation when an electric field is removed and finally  $E_c$  which is the coercive field - the field at which the polarisation can be reduced to zero. Typically materials demonstrate ferroelectricity below a certain phase transition temperature

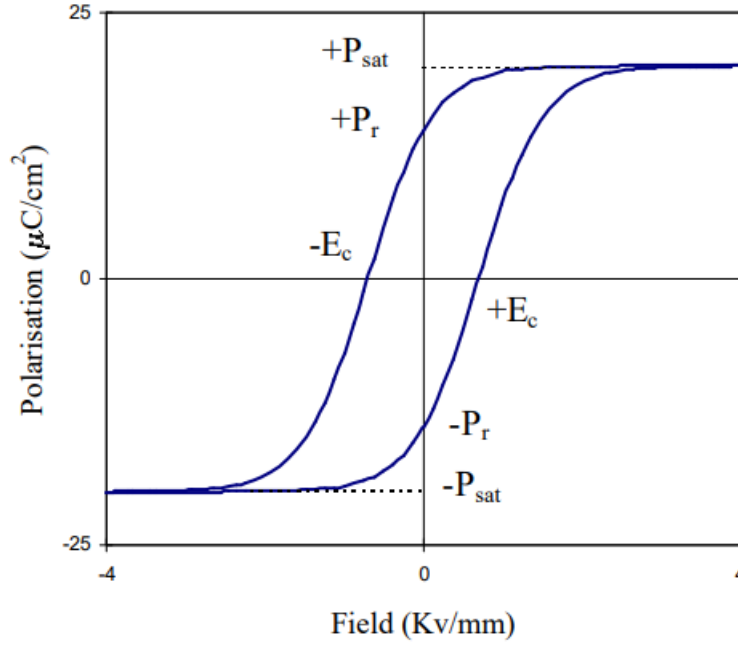


Figure 1.12: Ferroelectric hysteresis loop with some key points for the loop.  $\mathbf{P}_{sat}$  is the saturation polarisation,  $\mathbf{P}_r$  is the remnant polarisation and  $E_c$  is the coercive field. Figure from [58].

which is called the *Curie temperature*,  $T_c$ . Usually in the case of perovskite materials, moving above this transition temperature signifies a change in the structure as the system moves to a higher-symmetry phase and moves to exclusively a dielectric material. This is usually associated with a phase transition to a centrosymmetric space group. We have briefly talked about the displacement of ions in a bulk system and this is what drives the appearance of ferroelectricity within the material. The concept of an electric dipole is central to the application of electrostatics. For small finite systems like isolated atoms or molecules this dipole can easily be modelled. The dipole moment  $\mathbf{d}$ , of a collection of charges  $q_i$  at positions  $\mathbf{r}_i$  is defined as:

$$\mathbf{d} = \sum_i q_i \mathbf{r}_i, \quad (1.4.1)$$

If we think of a continuous charge density throughout a material we can use the expression:

$$\mathbf{d} = \int Q(\mathbf{r})\mathbf{r}d\mathbf{r}, \quad (1.4.2)$$

where,  $Q(\mathbf{r})$  is the charge density. We can then calculate our bulk polarisation by thinking of the size of the electric dipole per unit volume:

$$\mathbf{P} = \frac{\mathbf{d}}{\Omega}, \quad (1.4.3)$$

Where  $\Omega$  is the volume of the unit cell. Unfortunately this method does not work well for systems in bulk. This arises due to the position of the unit cell that we choose within our bulk system. If we take a system of repeating units of anions and cations spaced  $a/2$  apart from each other such that the unit cell is of length  $a$  we can notice that the system is symmetrical. If we take the positive ion and look either side we see no difference, our system has inversion symmetry and thus non-polar. This leads to a couple of problems as shown in Figure 1.13. This model highlights an issue. If we take



Figure 1.13: 1-Dimensional chain of alternating ions with negative and positive charge. The dashed lines show two different unit cells of same length  $a$

any unit cell in our 1-D chain of ions then we see a non-zero polarisation as shown below:

$$\begin{aligned} \mathbf{P} &= \frac{1}{a} \sum_i q_i \mathbf{r}_i \\ &= \frac{1}{a} \left( -1 \times \frac{a}{4} + 1 \times \frac{3a}{4} \right) \\ &= \frac{1}{a} \frac{2a}{4} \\ &= \frac{1}{2} \end{aligned} \quad (1.4.4)$$

The next problem is that if we look at the second unit cell we find:

$$\begin{aligned}
 \mathbf{P} &= \frac{1}{a} \sum_i q_i \mathbf{r}_i \\
 &= \frac{1}{a} \left( 1 \times \frac{a}{4} - 1 \times \frac{3a}{4} \right) \\
 &= \frac{1}{a} \times -\frac{2a}{4} \\
 &= -\frac{1}{2}
 \end{aligned} \tag{1.4.5}$$

We find that we have opposing values for the polarisation in the bulk system and the polarisation is dependent on the reference system that is used. This is where the *modern theory of polarisation* came in. We find that for an inversion symmetric system the series of ions will lead to a symmetrical version of the polarisation calculated dependent on the unit cell that was chosen. These polarisation quantities are symmetrical about a midpoint in our case is 0. The purpose of this method is to be able to measure a polarisation across an infinite crystal, unfortunately equations 1.4.2 and 1.4.3 cannot lead to a way of defining the polarisation in an infinite crystal. We therefore use the modern theory of polarisation to solve this issue. The modern theory of polarisation maps back to a point charge picture with Wannier centres for the electrons[59]. Experimentally this is not a problem as we measure the change in polarisation and as such this is what we look to do here, calculate *the change* in the polarisation. We find that all non-polar systems still contain polarisation lattices. The difference in this case is if we now displace one of our ions in each unit cell by some arbitrary value  $d$  then we find:

$$\begin{aligned}
 \mathbf{P} &= \frac{1}{a} \sum_i q_i \mathbf{r}_i \\
 &= \frac{1}{a} \left( -1 \times \frac{a}{4} + 1 \times \left( \frac{3a}{4} + d \right) \right)
 \end{aligned} \tag{1.4.6}$$

$$= \frac{1}{2} + \frac{d}{a} \tag{1.4.7}$$

and for the second unit cell:

$$\begin{aligned}\mathbf{P} &= \frac{1}{a} \left( +1 \times \left( \frac{a}{4} + d \right) - 1 \times \frac{3a}{d} \right) \\ &= -\frac{1}{2} + \frac{d}{a}\end{aligned}\tag{1.4.8}$$

If we now look at the difference between the non-polar and polar systems:

$$\Delta\mathbf{P} = \left( \frac{1}{2} + \frac{d}{a} \right) - \frac{1}{2} = \frac{d}{a}\tag{1.4.9}$$

And we find the identical value for the other unit cell. We now have calculated the size of the polarisation in the asymmetric system as a difference between the polar and non-polar polarisation lattices.

In this thesis however, we will not be examining the macroscopic polarisation of the systems we will study and we will look more at a crystallographic method of highlighting the origins of ferroelectricity in inorganic metal halides. We model this crystallographic method using invariants analysis which we model as a Landau-like model. Invariants analysis can be used to determine the free energy of a material about its phase transition and allows to determine through what methods various distortions in our material can arise. A phase-transition is the transformation of a system from one phase (in our case usually a change in space group, and thus ionic order) to another. The phase transition changes the properties of the material as a result of some external factors which could include temperature or pressure. For example above the Curie temperature we see materials lose their ferroelectric properties and will become dielectric, for example, BaTiO<sub>3</sub> loses its ferroelectric properties and becomes dielectric above 120°C [60]. The application of invariants analysis can help us learn about the second-order (continuous) phase transitions. The model for a proper ferroelectric can be described as:

$$(F - F_0) = a(T - T_c)P^2 + bP^4,\tag{1.4.10}$$

where  $F_0$  is the free-energy of the undistorted, high-symmetry structure,  $T_c$  is the Curie temperature and  $a$  and  $b$  are constants. Graphically this is described as the

trade mark potential double well (See figure 3.10). In the Landau theory, phase transitions occur when one of the constants changes sign (moves from positive to negative). In a ferroelectric phase transition the relevant distortions are displacive (the movement of ions throughout the crystal). Most displacive transitions are caused by the softening of particular phonon distortions and the *softening* and finally *freezing* of the distortions drives the appearance of such distortion, the softening of the polar distortion can be described as:

$$\omega^2 \propto \chi^{-1}, \quad (1.4.11)$$

where  $\omega^2$  is the square of the phonon frequency and  $\chi$  is the Landau parameter[61].  $\chi$  in the case of equation 1.4.10 represents the polarisation  $P$ . In Chapter 4 we look at the ionic dielectric response of the phonons and look to tune this fundamental property. In this thesis we will look at both proper and improper ferroelectricity. In our proper system, polar softening leads to a ground state ferroelectric structure through the primary order parameter, the polar mode. In an improper ferroelectric non-polar modes soften which leads to two non-polar distortions appearing but induce a polar mode via mode coupling, in this particular case the polar mode is a secondary order parameter (appears due to coupling with primary order parameters).

### Photoferroics

Because of the diverse range of devices that perovskites can be part of, ferroelectricity is a generally desired property in a lot of these devices[62], examples can include FeRAM[63], capacitors[64] and photovoltaics. In terms of photovoltaics there has been an increasing amount of research put into the idea of a ferroelectric photovoltaic (Photoferroics). A photoferroic is a material that combines the light harvesting properties of a photovoltaic and the properties of a ferroelectric material, these are sometimes aptly named FE-PV (Ferroelectric-Photovoltaics). This idea was first visualised by Vladimir Fridkin in 1985 with the idea of a *photoferroic crystal* for light absorption[65]. But photoferroics have remained within the realm of research for many years. The initial photoferroic was SbSI which as a ferroelectric had a polari-

sation  $25\mu\text{C}/\text{cm}^2$  with a band-gap of 1.9-2.0eV[66] but with an efficiency of approximately 3%[67] the material never moved from its infancy in terms of commercialisation. Photoferroics have been kept in the realm of research for a couple of reasons, firstly, their poor efficiencies and generally very poor conductivity throughout the crystal[68]. However in recent years there has been an upturn in the field of photoferroics with the perovskite halides and oxides showing promise in both solar light absorption and charge separation (of which we will explore some examples soon). Also photoferroic performance has tried to be explained using certain mechanisms which attempt to agree with experimentation.

The first of these mechanisms is the Bulk photovoltaic effect (BPE). BPE is only observed in non-centrosymmetric systems, the simplest model described by Belinicher and Sturman which they called the photogalvanic effect where asymmetric scattering of charge carriers leads to a net flow of randomly drifting charge carriers and a photocurrent[69]. The second of these BPE mechanisms is modelled on the idea that the electrostatic potential is asymmetric due to asymmetry of electron charge density around the ion of the material, again of which only appears in non-centrosymmetric crystals. As shown in Figure 1.14. Electrons absorb energy from photons of light to excite them above the ground state  $E_0$  to a total energy  $E$ . If  $E < V_1$  then the excited electron remains trapped in the potential well and will lose energy back to the ground state and not move. If  $E \gg V_2$  then the electron can move away over the potential barrier isotropically, finally if the energy sits between both potential wells  $V_1 < E < V_2$  then charge carriers are scattered by the large potential well to the left (with some being able to quantum tunnel). Others will flow to the right over the top of the potential barrier  $V_1$ . This leads to an overall photocurrent to the right. This mechanism allows for a photocurrent based on the absorption of light which is aligned with the asymmetries in the potential wells that form. Finally the third mechanism for BPE is initiated by the splitting of the conduction band in the presence of non-centrosymmetric crystal.

This effect commonly known as Dresselhaus or Rashba splitting[70]. This effect is driven by spin-orbit coupling so it is more commonly seen in materials in which some

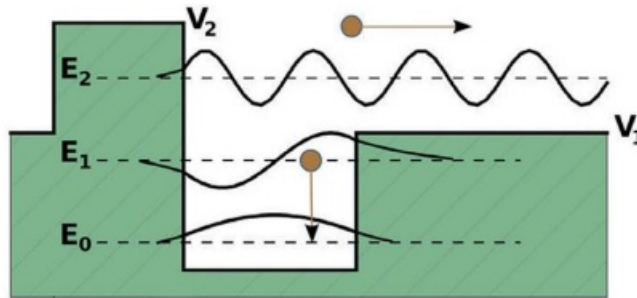


Figure 1.14: Visual description of a possible mechanism of the BPE in ferroelectric photovoltaics. Three energy scenarios above the ground state which show the photocurrent moving to the right over the asymmetric potential wells that form in non-centrosymmetric crystals. Figure taken from [68]

of the elements are considerably heavier and bigger relativistic properties are more prominent (for example lead). In this effect the probability of electrons being excited across the valence band is constant, but dependent on the polarisation of the light depends on the momentum of the electrons that are excited. This excitation leads to either a positive or negative crystal momentum which leads to a net current in one direction. This effect has been directly observed with MAPI, with Even *et al.* discussing the importance of the Spin-orbit coupling in perovskite photovoltaics with the band offsets driving the electrons towards the electrodes [71]. The asymmetry of the electron density also results in excitation of electrons from the valence to conduction band which is separated in real space. This *shifting* of electrons along the material is designated the title *shift current*, which has been experimentally shown in various structures: BaTiO<sub>3</sub>[72], SbSI[73] and GaAs[74] to name a few. Specifically in GaAs we can see the effects of the electron density of the highest point in the valence band and the lowest point in the conduction band, showing a clear real space separation. Figure 1 of [75] shows the shift of electrons from the Arsenic ion in the valence band to the Ga ions in the conduction band. In traditional p-n junction based solar cells, hot electrons/holes typically relax to the band-edges as described by Figure

1.7 and this leads to a loss of energy, this subsequently leads to a much smaller PCE and limits the open-circuit voltage  $V_{oc}$  to the size of the band-gap. For a photoferroic which exhibits the bulk photovoltaic effect, the driving force carrier separation is not the "*in-built electric field*" but the evolution of the electron wavefunction[76]. These leads to a rapid propagation to the electrodes, reducing the *hot carrier* effect and thus the  $V_{oc}$  no longer depends on the band-gap (Above band-gap photovoltages). Due to the fact that the method of charge separation depends on the asymmetry of the bulk material, single phase materials can be used, this also leads into the fact that p-n junctions require charge separation to occur in a small region in the material, the depletion zone, whereas the the charge separation can occur in the bulk of the material for a photoferroic.

One of the issues we have with ferroelectric perovskites is that a lot of ferroelectric materials are high band-gap oxides[77, 78, 79]. The most famous of these is BaTiO<sub>3</sub> in which has a very large polarisation of  $0.26\mu\text{C}/\text{cm}^2$ [80] but also has a large band-gap[81]. This has lead to the exploration of looking for perovskite materials which have suitable band-gaps and engineering ferroelectricity into these materials[82]. Ferroelectricity is a very sought after property in photovoltaics due to the ability to engineer an extremely large photovoltaic effect[83] with above band-gap photovoltages[68] and enhanced charge-separation[84]. Examples of this can include the family of solid oxide solutions  $[\text{KNbO}_3]_x[\text{BaNi}_{0.5}\text{Nb}_{0.5}\text{O}_{3-\delta}]_{1-x}$  in which based on the value of  $x$  we see a wide range of direct bandgaps ranging from 1.1-3.8eV. Interestingly the  $x=0.1$  composition is both polar at room temperature and has a direct bandgap of 1.39eV[85]. Li *et al.* also showed that a tin based hybrid-layered perovskite also showed ferroelectric properties,  $(\text{C}_4\text{H}_9\text{NH}_3)_2(\text{NH}_3\text{CH}_3)_2\text{Sn}_3\text{Br}_10$  exhibits a large spontaneous polarisation of  $11.76\mu\text{C}/\text{cm}^2$  at room temperature with enhanced energy conversion efficiency[86]. Ferroelectricity in metal-halide perovskites and specifically MAPbI<sub>3</sub> (MAPI) have been under fierce debate. Some are in favour of the ferroelectric properties of MAPI arising from the movement of vacancies under an electric field[87], Other research suggests that even though the results of some DFT calculations from Fan *et al.* suggest that the lowest energy structure was a tetragonal ferroelectric phase,

experimental results suggested that the same tetragonal structure at room temperature is not ferroelectric[88]. On the other hand some work has suggested that MAPI is ferroelectric, work by Rakita *et al.*[89] has suggested that MAPI shows ferroelectric characteristics much like simple-harmonic generation and therefore it is non-centrosymmetric.

## 1.5 Outline and Aims of Thesis

This thesis is a computational study of inorganic halide metal perovskites. We aim to develop a comprehensive story of the origins of ferroelectricity within these inorganic structures. Chapter 2 will summarise the key methodologies which underpin the work we have completed in this review, this includes the theory of Density Functional Theory (DFT), Periodicity and Hellman-Feynman Theorem. Embedded within each research chapter we explore other theories which have are more focused within each body of research. We then present our findings in each of the three research chapters. Chapter 3 presents a look at the structural complexity of the gold double perovskites with an aim at looking at the interplay between the various distortions that appear as we alter the chemistry. The aim of the results in this chapter is to take you on a journey of the high symmetry cubic structure down to the double tilted low symmetry structure and show how the primary distortions introduced from the cubic to tetragonal phase influences the appearance of all of the other distortions. We explore the possibility of a polar phase and discuss its appearance through a pseudo-triggered mechanism and show the influence of both the strain and Jahn-Teller distortions on this non-centrosymmetric phase.

Chapter 4 Looks to take the discussions of the previous chapter and analyse how this influences the optoelectronic properties of these materials. We look to explore the origin of the bandgap of the material and how the gap is tuned using distortions which is directly linked to the chemical composition. We explore the effects of tilting on the effective masses which will affect the charge mobility through the structure. We explore the effects of chemical substitution on the absorption of the material and

explore the absorption gaps that appear in the spectra. Finally we look at the effects of pressure on the system and find some wonderful results showing some excellent cooperative coupling between all distortions with the hope of developing a polar phase. We use the phonon contributions of the ionic dielectric response to tune a large dielectric constant in the material.

In Chapter 5 looks at a different system and another method of inducing ferroelectricity into the material. We explore the Ruddlesden-Popper inorganic metal halide perovskite which is known for having a relatively suitable bandgap for optical light absorption and introduce ferroelectricity into the structure with a method called *Hybrid improper ferroelectricity* a form of ferroelectricity which arises due to two non-polar distortions coupling to break inversion symmetry and couple trilinearly to the polar distortion. We expand upon this to explore the effects of chemical substitution on the size of the polar distortion and the bandgaps that appear. We explored this as a another method of charge separation within photovoltaic perovskites. Overall, we hope to show the link between structure and electronic properties and the benefits of which spending time in determining the origins of different electronic properties.

# Theoretical and Computational Methods

*Computation is not the same as thought and emulation is not the same as  
imagination. - Abhijit Naskar*

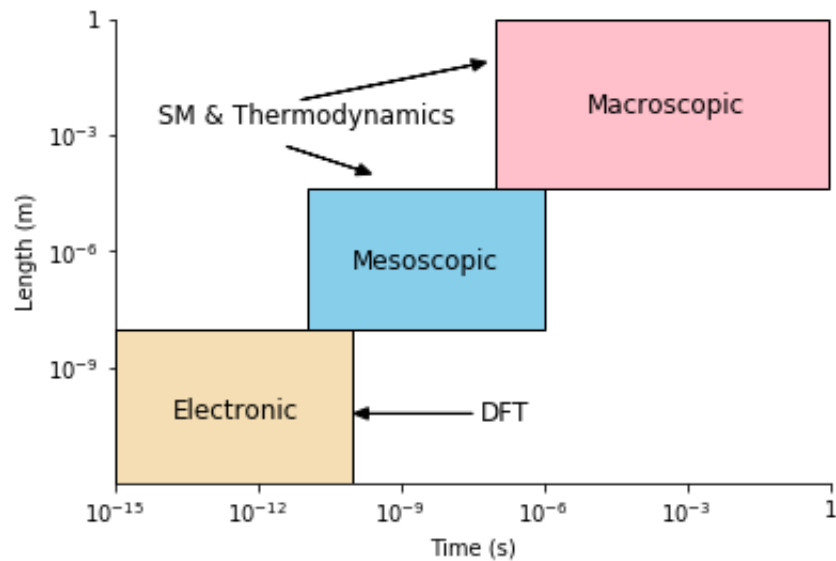


Figure 2.1: The different methods that are employed in condensed matter physics when looking at particular time and length scale regimes. Figure is taken from [90].

**I**N recent years there has been considerable computational work undertaken in the field of materials science. Materials modelling is an incredibly useful technique that has brought forwards our attempts at predicting the properties of materials. This can be especially useful in attempting to predict the properties of materials that have not been synthesised yet or materials that are expensive to make experimentally. In this thesis the main methodology will be the application of Density Functional Theory - a first principles computational technique that can accurately model the properties of a lot of different materials. In this chapter we will be focusing on the theory that backs up the method and the different input parameters that can affect the accuracy of the calculations.

## 2.1 Density Functional Theory

Density Functional Theory (DFT) is a theoretical method of determining the ground state structure of materials. Unfortunately it is very difficult to solve the Schrödinger

equation for any more than a 1-body system. The wave function of the system becomes exponentially more complicated as we increase the size of the system due to the interactions between the particles in the system. This problem is defined as the many-body problem and as such Density Functional Theory makes a set of approximations that change dependent on the problem that is faced by theorists. DFT can therefore be a relatively simple computational modelling method that can help determine the electronic structure of a material and as such the associated properties of the material.

The fundamental most "*basic*" equation for a non-relativistic quantum mechanical many-body system is defined as:

$$\hat{H}\Psi = E\Psi, \quad (2.1.1)$$

where  $\hat{H}$  is the Hamiltonian operator,  $\Psi$  being the many-body wave function and  $E$  is the energy of the system. The Hamiltonian of the system can be defined as a combination of contributions from the kinetic energy of the electrons  $E_{k(e)}$  and nuclei  $E_{k(n)}$  and the coulomb potential between the electrons  $U_{ee}$ , the nuclei  $U_{nn}$  and between the electrons and nuclei  $U_{en}$ . The Hamiltonian can then be defined as the combination of the interactions between particles:

$$\hat{H} = \hat{E}_{k(e)} + \hat{E}_{k(n)} + \hat{U}_{ee} + \hat{U}_{nn} + \hat{U}_{en}, \quad (2.1.2)$$

These simple terms can be expanded to determine the energies and potentials associated with atomic coordinates, mass and nuclear charge:

$$\left[ -\sum_i \frac{\hbar^2}{2m_e} \nabla_i^2 - \sum_I \frac{\hbar^2}{2M_I} \nabla_I^2 + \frac{1}{2} \sum_{i \neq j} \frac{e^2}{4\pi\epsilon_0} \frac{1}{|\mathbf{r}_i - \mathbf{r}_j|} + \frac{1}{2} \sum_{I \neq J} \frac{e^2}{4\pi\epsilon_0} \frac{Z_I Z_J}{|\mathbf{R}_I - \mathbf{R}_J|} - \sum_{i,I} \frac{e^2}{4\pi\epsilon_0} \frac{Z_I}{|\mathbf{r}_i - \mathbf{R}_I|} \right] \Psi = E\Psi, \quad (2.1.3)$$

Where the upper-case letters are associated with the nuclei and lower-case letters associated with the electrons.  $M_I$  is the mass of the  $I$ th nucleus,  $\mathbf{R}_I$  the atomic coordinates of the  $I$ th nucleus and  $Z_I$  is the nuclear charge also associated with the  $I$ th nucleus, and lower-case letters are then extended to its electron counterparts. It's

quite obvious here to see the level of complexity when we start to add more nuclei and electrons to our systems. Fortunately there are several approximations that can be applied to this complicated equation which can help us.

### Clamped Nuclei and Born-Oppenheimer Approximations

In order to determine a way of solving the unsolvable approximations need to be applied to our system. One approximation is quite a simple one - The nuclei of our system are considerably more massive than the electrons and therefore their movement is negligible in comparison to the electrons. We can therefore set  $M_I = \infty$  in equation 2.1.3. This implies that the kinetic energy of the nuclei is negligible and thus can be removed from the equation. The coulomb interaction between nuclei can also be deemed a constant:

$$E = E_{tot} - \frac{1}{2} \sum_{I \neq J} \frac{e^2}{4\pi\epsilon_0} \frac{Z_I Z_J}{|\mathbf{R}_I - \mathbf{R}_J|}, \quad (2.1.4)$$

This then allows us to rewrite equation 2.1.3 as:

$$\left[ -\sum_i \frac{\hbar^2}{2m_e} \nabla_i^2 + \frac{1}{2} \sum_{i \neq j} \frac{e^2}{4\pi\epsilon_0} \frac{1}{|\mathbf{r}_i - \mathbf{r}_j|} - \sum_{i,I} \frac{e^2}{4\pi\epsilon_0} \frac{Z_I}{|\mathbf{r}_i - \mathbf{R}_I|} \right] \Psi = E\Psi, \quad (2.1.5)$$

We can then expand upon this by using the Born-Oppenheimer Approximation which is the assumption that the motion of nuclei and electrons can be treated independently. Proposed by Max Born and J. Robert Oppenheimer in 1927[91], this allows us to solve for the positions of the electrons whilst keeping the nuclei positions constant. Described mathematically by:

$$\Psi(\mathbf{r}_i, \mathbf{R}_j) = \Psi_e(\mathbf{R}_j, \mathbf{r}_i) \Psi_n(\mathbf{R}_j) \quad (2.1.6)$$

This shows the decoupling of the electronic wavefunction  $\Psi_e(\mathbf{r}_j)$  and the nuclei wavefunction  $\Psi_n(\mathbf{R}_j)$  from the many-body wavefunction  $\Psi(\mathbf{r}_i, \mathbf{R}_j)$ . Of course even with the decoupling of the two the equation in 2.1.3 and subsequently 2.1.5 it is still incredibly difficult to solve. Thankfully Hohenberg & Kohn [92] developed a way in which this complex equation can be reformulated.

### Hohenberg & Kohn Theorem

Hohenberg & Kohn put forward the following:

**Theorem:** The external potential  $v(\mathbf{r})$  is a unique functional of the ground state electron density  $n(\mathbf{r})$ . This theorem was proven using a method called *reductio ad absurdum*. A proof whereby you show that the opposite (in our case the idea that a external functional is not unique to the ground state electron density) would lead to a contradiction. If we are to prove this as *reductio ad absurdum* there must exist another external potential  $v'(\mathbf{r})$  with a different wavefunction  $\Psi'$  but has the same ground state density of the initial external potential  $v(\mathbf{r})$ ,  $n(\mathbf{r})$ . We can make the clear assumption that the two many-body wavefunctions are different,  $\Psi \neq \Psi'$ . We can therefore describe the energy and Hamiltonian's of the two systems as a function of their wavefunctions:

$$E' = \langle \Psi' | H' | \Psi' \rangle < \langle \Psi | H' | \Psi \rangle = \langle \Psi | H + v' - v | \Psi \rangle, \quad (2.1.7)$$

where the right hand side of the equation is can hold due to the fact that the difference between the two different Hamiltonian's is the difference in the external potential. We can therefore describe the energy  $E'$  as:

$$\begin{aligned} E' &< \langle \Psi | H + v' - v | \Psi \rangle \\ &= \langle \Psi | H | \Psi \rangle + \langle \Psi | v' - v | \Psi \rangle \\ &= E + \int [v'(\mathbf{r}) - v(\mathbf{r})] n(\mathbf{r}) d\mathbf{r}, \end{aligned} \quad (2.1.8)$$

Due to the fact that our description of the system is symmetrical we can exchange the two primed and unprimed values:

$$E < E' + \int [v(\mathbf{r}) - v'(\mathbf{r})] n(\mathbf{r}) d\mathbf{r}, \quad (2.1.9)$$

Combine the two equations together and we arrive at:

$$E + E' < E' + E, \quad (2.1.10)$$

This of course is a contradiction and therefore the Hohenberg & Kohn theorem is supported that the external potential  $v(\mathbf{r})$  is a unique functional of the ground state

electron density  $n(\mathbf{r})$ .

A full understanding of the Hohenberg & Kohn theorem leads to use a description of a simplistic description a system by knowing:

1. In the ground state the electron density  $n(\mathbf{r})$  uniquely describes the external potential of the nuclei  $V_n$ .
2. In any state the external potential  $V_n$  can describe the many-body wavefunction  $\Psi$  of the system.
3. The many-body wavefunction can accurately describe the total energy of the system  $E$ .

Compiling of the above together we can show that  $n(\mathbf{r}) \rightarrow V_n \rightarrow \Psi \rightarrow E$ . This shows that the energy of the system  $E$  must be a functional of the electron density  $E = F[n]$ .

### Kohn-Sham Equations

The Hohenberg-Kohn Theorem has shown us how the Energy of a system can be described as a functional of the electron density. It does not however, explain how to construct such a functional. The Kohn-Sham method therefore involves the calculation of the kinetic energy of a non-interacting system using independent wavefunctions. We can describe such a functional as:

$$F[n] = \int d\mathbf{r} n(\mathbf{r}) V_n(\mathbf{r}) + \langle \Psi[n] | \hat{T} + \hat{W} | \Psi[n] \rangle \quad (2.1.11)$$

We can see from the functional above that the wavefunction is dependent on the electron density but the kinetic and coulomb operators are not. Kohn & Sham[93] therefore split these terms into the kinetic and coulomb energies of *independent electrons*

and include any other energies to make up the difference:

$$\begin{aligned}
 E &= F[n] \\
 &= \underbrace{\int d\mathbf{r} n(\mathbf{r}) V_n(\mathbf{r})}_{\text{External potential}} - \underbrace{\sum_i \int d\mathbf{r} \psi_i^*(\mathbf{r}) \frac{\nabla^2}{2} \psi_i(\mathbf{r})}_{\text{Kinetic energy}} + \underbrace{\frac{1}{2} \int \int d\mathbf{r} d\mathbf{r}' \frac{n(\mathbf{r}) n(\mathbf{r}')}{|\mathbf{r} - \mathbf{r}'|}}_{\text{Hartree energy}} + \underbrace{E_{xc}[n]}_{\text{XC energy}} \quad (2.1.12)
 \end{aligned}$$

The idea of the equation (From Guistano[94]) was to collate all of the terms that we do know and try and estimate the difference with the extra term  $E_{xc}[n]$ , the *exchange-correlation energy*. If we did know this term then it would be simple to calculate the total energy of the system in its ground state. If we apply the Hohenberg-Kohn variational principle which states that "*the ground state electron density  $n_0$  is precisely the function which minimises the total energy*"[92]:

$$\left. \frac{\delta F[n]}{\delta n} \right|_{n_0} = 0 \quad (2.1.13)$$

to equation 2.1.12:

$$\left[ -\frac{1}{2} \nabla^2 + V_n(\mathbf{r}) + V_H(\mathbf{r}) + V_{xc}(\mathbf{r}) \right] \psi_i(\mathbf{r}) = \epsilon_i \psi_i(\mathbf{r}), \quad (2.1.14)$$

where  $-\nabla^2/2$ ,  $V_n$  and  $V_H$  are the kinetic energy, external and Hartree potentials respectively.  $V_{xc}(\mathbf{r})$  being:

$$V_{xc}(\mathbf{r}) = \left. \frac{\delta E_{xc}[n]}{\delta n} \right|_{n_r} \quad (2.1.15)$$

we arrive at the Kohn-Sham equations where  $V_{xc}$  is called the *exchange-correlation potential*. These equations are incredibly powerful and are useful in trying to determine ground state properties of many systems in DFT. Unfortunately the accuracy of such properties must entirely depend on the accuracy of the exchange-correlation functional, which unfortunately we do not know what this is and considerable work has gone into trying to construct such a functional over the last 50 years.

### Local Density Approximation (LDA)

The simplest functional is one which is described as part of the local density approximation (LDA)[95, 96] which looks at the most basic way of analysing the exchange

and correlation energies of a system the *homogeneous electron gas*. This is modelled in a similar way to a free electron gas in which the electrons are confined to a box and we take the potential as constant. Therefore the exchange-correlation energy in a homogeneous electron gas is constant and consistent at any point throughout the box. Using this approximation the exchange-correlation energy can be described as:

$$E_{xc}^{LDA}[\rho] = \int n(\mathbf{r})\epsilon_{xc}(n)d\mathbf{r} \quad (2.1.16)$$

where  $n$  is the electronic density and  $\epsilon_{xc}$  is the exchange-correlation energy per particle of homogeneous electron gas of change density  $n$ , which can also be split into the two different energies:

$$\epsilon_{xc} = \epsilon_x + \epsilon_c \quad (2.1.17)$$

$$\epsilon_x = -\frac{3}{4}\left(\frac{3}{\pi}\right)^{\frac{1}{3}}n^{\frac{1}{2}}(\mathbf{r}) \quad (2.1.18)$$

This exchange energy can be described by the energy released when two or more electrons with the same spin exchange their positions, this also ties into the correlation energy which is a measure of how much movement one electron is influenced by the presence of all of the others. The correlation energy can be accurately calculated for a homogeneous electron gas through Monte-Carlo simulations.

### Beyond the Local Density Approximation

Over the past 65 years since the first basic principles of Density Functional Theory there have been considerable advances in the accuracy of exchange correlation functionals. Unfortunately it is difficult to combine the energies of every kind of interaction that appears in molecules without sacrificing computational expense. Therefore, we create different exchange correlation functionals that can be used for specific tasks. Moving up the Jacobs Ladder (Figure 2.2) the next step in chemical accuracy is the Generalised Gradient Approximation (GGA).

The Generalised Gradient Approximation (GGA) improves on the Local Density Approximation by applying the derivative of the electronic density to the exchange-

correlation energy:

$$E_{XC}^{GGA}[n(\mathbf{r})] \approx \int n(\mathbf{r}) E_{xc}(n(\mathbf{r})|\nabla n(\mathbf{r})|) d\mathbf{r} \quad (2.1.19)$$

The  $E_{XC}^{GGA}$  initially was split into energies associated with exchange and then correlation. An example was the B88[97] functional which was then combined with a selection of correlation functionals LYP[98], P86[99].

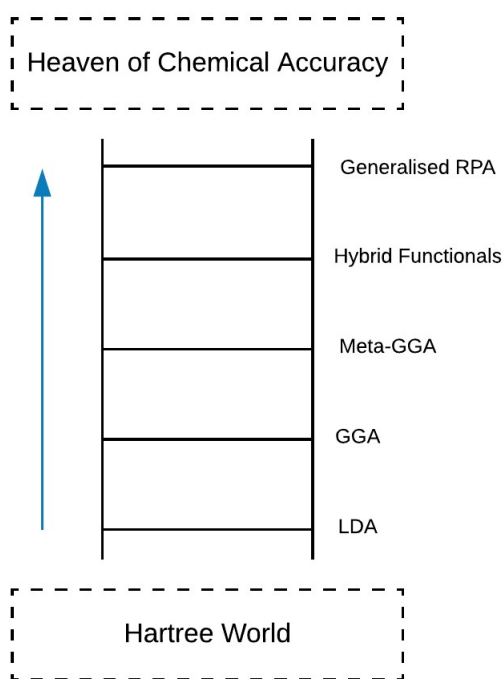


Figure 2.2: Jacobs ladder of exchange-correlation functionals linking the Hartree world to the heaven of chemical accuracy. Higher up the ladder leads to increased computational expense but with increased chemical accuracy.

Higher levels of the Jacob's ladder introduce more computationally expensive non-local functionals of the orbitals. Meta-GGA's are essentially an extension to GGA's of which the non-interacting kinetic energy is applied as an additional input:

$$E_{XC}^{MGGA}[\rho] = \int d\mathbf{r} \rho(\mathbf{r}) \epsilon_{XC}(\rho(\mathbf{r}), \nabla \rho(\mathbf{r}), \tau_S(\mathbf{r})), \quad (2.1.20)$$

where  $\tau_S(\mathbf{r})$  is described as the non-interacting kinetic energy density and can be evaluated through:

$$\tau_S(\mathbf{r}) = \frac{1}{2} \sum_{i\mathbf{k}} |\nabla \phi_{i\mathbf{k}}(\mathbf{r})|^2, \quad (2.1.21)$$

such meta-GGA's can be described through exchange-correlation functionals M06L[100], TPSS[101] and SCAN[102]. The final two rungs are venturing into high computational cost, hybrid functionals are a class of approximations that incorporate a portion of exact exchange from Hartree-Fock theory with the rest of the functional constructed from other sources. This contribution of exact exchange leads to improvements in a variety of molecular properties including energies, bond lengths and phonon frequencies. An example is the PBE0[103] hybrid functional which mixes the PBE exchange energy with Hartree-Fock:

$$E_{XC}^{PBE0} = \frac{1}{4} E_x^{HF} + \frac{3}{4} E_x^{PBE} + E_c^{PBE} \quad (2.1.22)$$

where  $E_x^{PBE}$  and  $E_c^{PBE}$  are the exchange and correlation functionals respectively and  $E_x^{HF}$  is the functional of the Hartree-Fock exact exchange:

$$E_X^{HF} = -\frac{1}{2} \sum_{i,j} \int \int \psi_i^*(\mathbf{r}_1) \psi_j^*(\mathbf{r}_2) \frac{1}{r_{12}} \psi_j(\mathbf{r}_1) \psi_i(\mathbf{r}_2) d\mathbf{r}_1 d\mathbf{r}_2 \quad (2.1.23)$$

The exact ratio of the mixing is specified by fitting functional predictions to experimental data. The final rung of Jacob's ladder addresses the Random Phase Approximation (RPA). The RPA actually predates Density Functional Theory and was not implemented until the late 1970's. RPA exchange-correlation energies is the sum of the correlation energy and the Hartree-Fock energy from all DFT orbitals. Evaluating over both unoccupied and occupied orbitals allows for much more accurate energies and properties including lattice constants, atomization constants[104] and heats of formation[105] to name a few.

Throughout this thesis we used the PBESol exchange-correlation functional due to its accuracy in determining lattice constants. Seeing as the research is aimed in analysis of the different structures the functional was primarily aimed at determining accurate structures for the wide variety of materials that we were examining. It is know that the

electronic properties of the material itself can be more accurately determined using the more computationally expensive hybrid functionals. There is also no discernible difference in the shape of the bands between the structures that we analysed and that found by a hybrid functional, with the only difference being that of the gap[106].

### Self-Consistent Equations

With a full understanding Hohenberg & Kohn and Kohn-Sham we can look at solving and determining the ground state energies of the system of interest. This involves a self-consistent process. The first step is initialising the electron density, this electron density is used to calculate an effective potential, the subsequent effective potential is used to solve the Kohn-Sham equations which subsequently creates a new electron density. If this density is within the tolerance that was given in the DFT code then the code will output the final results of the energy, forces, pressures etc.

$$\left[ \frac{1}{2} \nabla^2 + V_{eff}(\mathbf{r}) \right] \phi_i(\mathbf{r}) = \epsilon_i \phi_i(\mathbf{r}) \quad (2.1.24)$$

$$V_{eff}(\mathbf{r}) = V_n(\mathbf{r}) + V_H(\mathbf{r}) + V_{xc}(\mathbf{r}) \quad (2.1.25a)$$

$$V_n(\mathbf{r}) = - \sum_I \frac{Z_I}{|\mathbf{r} - \mathbf{R}_I|} \quad (2.1.25b)$$

$$V_H(\mathbf{r}) = \int \frac{n(\mathbf{r}')}{|\mathbf{r}' - \mathbf{r}|} d\mathbf{r}' \quad (2.1.25c)$$

$$V_{xc}(\mathbf{r}) = \frac{\delta E_{xc}[n]}{\delta n}(\mathbf{r}) \quad (2.1.25d)$$

$$n(\mathbf{r}) = \sum_i |\phi_i(\mathbf{r})|^2 \quad (2.1.25e)$$

Equation 2.1.24 is defined as our single-particle Schrödinger equation and the subsequent equations a-e represent the individual components in the "master equation". Equation 2.1.24 can be solved as a standard eigenvalue problem, however, in order to solve for both the eigenvalues and eigenfunctions the total potential  $V_{tot}(\mathbf{r})$  needs to be known. Unfortunately because the Hartree and exchange-correlation potential depend on the electron density and the density depends on the eigenfunctions

(equation [2.1.25e](#)) it is not possible to solve by conventional means. Due to the fact that all of the equations are interlinked with each other the equation must be solved self-consistently.

Self-consistent equations involve taking an estimation for electron density solving the equations and returning a new density, if it is not the same then we repeat the process until the two densities are equal. Figure [2.3](#) is a basic schematic for this self consistent method:

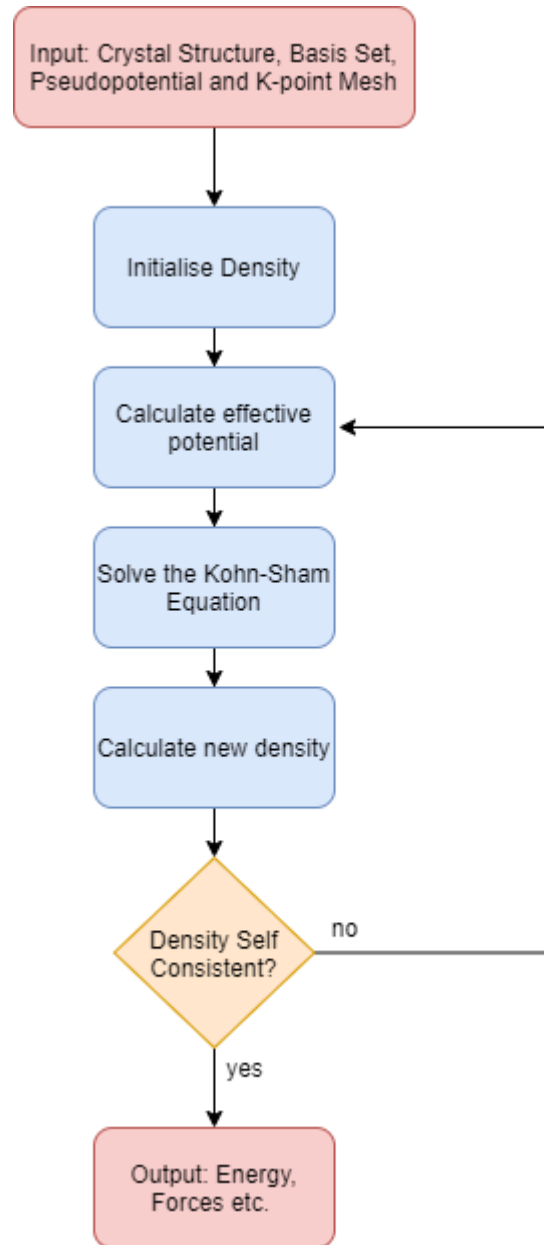


Figure 2.3: An adapted flow chart of the one found in chapter 3 of [94] showing the self-consistent method of calculating the electronic density.

## 2.2 Periodicity, Basis Sets & Pseudopotentials

### Periodicity and Reciprocal Space

When we use density functional theory in condensed matter physics it is useful to think of a material as a series of repeating unit cells with periodic boundary conditions. The idea of using periodic boundary conditions allows us to define our properties as bulk due to the fact that in a crystalline solid the majority of the atoms are within the bulk and not at the surface. Periodic boundary conditions also help the simplicity of the calculation by modelling an entire crystalline structure just on the atoms in one unit cell. The unit cells can be described by seven lattice systems; cubic, tetragonal, Orthorhombic, Hexagonal, Monoclinic and Triclinic. These lattice systems can be described only by six parameters: three lattice parameters ( $\mathbf{a}_1$ ,  $\mathbf{a}_2$ ,  $\mathbf{a}_3$ ) and three angles between them ( $\alpha$ ,  $\beta$ ,  $\gamma$ ).

The seven lattice systems can then subsequently be divided due to the atomic positions in the lattice system. These can be described by fourteen Bravais lattices (Table 2.1), this can then correspond to the 230 space groups that can describe crystal systems. Crystal systems can also be described by both a *direct* and *reciprocal* lattice.

Lattice System	Bravais Lattice Types
Cubic	Primitive, Body-Centered, Face Centered
Tetragonal	Primitive, Body-Centered
Orthorhombic	Primitive, Body-Centered, Face-Centered, Base-Centered
Hexagonal	Hexagonal
Monoclinic	Primitive, Base-Centered
Triclinic	Trigonal and Triclinic

Table 2.1: The 7 lattice systems and subsequent 14 Bravais lattice can be used to describe the symmetry of the crystal.

Reciprocal lattices are a representation of the direct lattice in Fourier ( $\mathbf{k}$ ) space. If we define our reciprocal lattice as ( $\mathbf{b}_1$ ,  $\mathbf{b}_2$ ,  $\mathbf{b}_3$ ) then we can show the relationship of the

direct and reciprocal lattice as:

$$[b_1, b_2, b_3]^T = 2\pi[a_1, a_2, a_3]^{-1} \quad (2.2.1)$$

$$a_i \cdot b_j = 2\pi\delta_{ij}, \quad (2.2.2)$$

where  $\delta_{ij}$  is defined as a Kronecker-delta symbol (1 if  $i = j$  and 0 when  $i \neq j$ ). With the knowledge of the Kronecker-delta function it is implied that every reciprocal lattice vector is orthogonal (normalized to  $2\pi$ ) [107]. *Direct* and *reciprocal* space are equivalent in the fact that the lattice vector can be expressed as a linear combination of the basis vectors with numerical coefficients:

$$\mathbf{K} = \alpha_1(\mathbf{a}_1, \mathbf{b}_1) + \alpha_2(\mathbf{a}_2, \mathbf{b}_2) + \alpha_3(\mathbf{a}_3, \mathbf{b}_3) \quad (2.2.3)$$

When analysing structures there is one unit cell which is particularly useful. *The Brillouin Zone* is formed from breaking up sections of the reciprocal lattice and is formally constructed by drawing perpendicular bisectors to the shortest reciprocal lattice vectors. This volume is then called *the brillouin zone*. The brillouin zone is particularly useful for analysis of the electronic properties of a crystal structure where we can map out the bandstructure of a material as the bands pass through each of the critical points in a brillouin zone. Upper greek letters are generally used for points inside the first brillouin zone, whereas roman letters account for points and lines on the surface of the brillouin zone. An example of a bandstructure is found below in Figure 2.4.

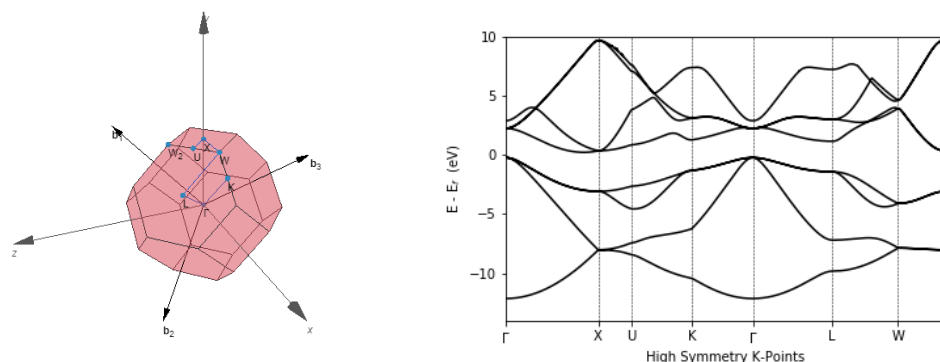


Figure 2.4: PBE bandstructure of a silicon crystal to show the bands passing through the critical points of the Brillouin zone. K-Path ( $\Gamma \rightarrow X \rightarrow U \rightarrow K \rightarrow \Gamma \rightarrow L \rightarrow W \rightarrow X$  from SeeK-Path[108]).

## Basis Sets

Basis sets are used in theoretical and computational methods to represent the electronic wavefunction. This method is used to determine a numerical solution to the Kohn-Sham equation by transforming our differential equations into algebraic ones which can be easily calculated with a computer. Dependent on the system that is studied will determine which of the basis sets that are used. Fortunately there is only two main basis sets which is used in computational chemistry: Plane-wave and atomic orbitals. In this thesis we will be using exclusively a plane-wave basis set due to the simplicity of the calculations and the overall cheap cost of the basis set in comparison to the atomic orbitals.

## Plane Waves

When studying electronic structures of crystal systems we can be investigating systems with electrons in the order of  $10^{38}$ . With crystal systems being periodic we can describe accurately the electronic properties of a material through a single unit cell system. Bloch's theorem shows that the wavefunction of an electron can be expressed in terms of a plane wave and a periodic function[109]. As such Bloch's theorem can

be described by:

$$\psi_n(\mathbf{r}) = u_n(\mathbf{r})e^{i\mathbf{k}\cdot\mathbf{r}} \quad (2.2.4)$$

where the plane wave has wave vector  $\mathbf{k}$  and  $u_n(\mathbf{r})$  describes the periodic part of the wavefunction where  $u_n(\mathbf{r}) = u_n(\mathbf{R} + \mathbf{r})$  and  $\mathbf{R}$  is one of the lattice vectors. Plane wave basis sets are chosen to best describe the wavefunction in the periodic cell.  $u_n(\mathbf{r})$  can then be written as:

$$u_n(\mathbf{r}) = \sum_{\mathbf{G}} c_{n,\mathbf{G}} e^{i\mathbf{G}\cdot\mathbf{r}} \quad (2.2.5)$$

where  $c_{n,\mathbf{G}}$  are the plane wave coefficients and  $\mathbf{G}$  is the reciprocal lattice vector. By combining these two equations the wavefunction can then be written as an infinite sum of plane waves:

$$\psi_n(\mathbf{r}) = \sum_{\mathbf{G}} c_{n,(\mathbf{k}+\mathbf{G})} e^{i(\mathbf{k}+\mathbf{G})\cdot\mathbf{r}} \quad (2.2.6)$$

Whilst Bloch's theorem allows us to observe an infinite system by calculating a finite number of wavefunctions, plane-wave density functional theory codes use the definition of the  $\mathbf{G}_{max}$  to describe this effect. The size of  $\mathbf{G}_{max}$  determines entirely on the balancing factors of computational cost and accuracy. This increase and decrease in accuracy thus determines how many terms we use to describe the planewave expansion. We therefore employ methods such as convergence tests in which we can find the maximum accuracy for minimum cost. This is usually tested against the properties of interest (energy, pressure, forces etc.) In planewave cutoff DFT codes the kinetic energy cutoff is described as the kinetic energy of the planewave with the largest reciprocal lattice vector:

$$E_{cut} = \frac{|\mathbf{G}_{max}|^2}{2} \quad (2.2.7)$$

The idea of an energy based cut-off allows for easy comparison between different calculations and when attempting convergence calculations.

## Pseudopotentials

In order to assist in computational time and expense it is possible to redefine the complicated inner non-valence core electrons and a consistent effective potential

called a pseudopotential. Non-valence electrons are subject to various effects of motion when close to the atomic nucleus and can make it incredibly difficult to determine the wavefunction of the inner electrons. Therefore we use a *fake* potential which averages the energy over a particular radius in order to speed up our calculations. It is important to highlight the computational expense vs. computational accuracy when designing pseudopotentials and there are a variety of different ones to choose from. For the purpose of this research we will be using only the PAW (projector augmented-wave) pseudopotentials[110]. From Figure 2.5 we can see that below the cutoff radius

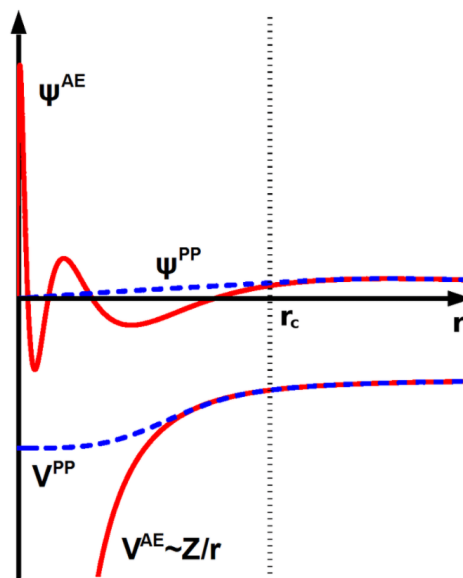


Figure 2.5: Schematic of the wavefunctions and potentials of both the all-electron and pseudopotential[111], above the cutoff radius  $r_c$  the wavefunction and potentials match.

the pseudopotential does not accurately match the all-electron wavefunction and potential, it does however act as an average across the values below  $r_c$ . Whilst we do lose some accuracy of our calculations the amount of computational expense is reduced. In some calculations the cutoff radius is increased to increase the speed of convergence and therefore it is less accurate to produce realistic properties of the material.

These are generally called softer pseudopotentials.

## 2.3 Density Functional Perturbation Theory

### Hellman-Feynmann Theorem

The Hellmann-Feynman Theorem describes how the derivative of the energy with respect to some order parameter relates to the expectation value of the derivative of the Hamiltonian with respect to the same order parameter. It is a vital theorem in Density Functional Theory which can map out the forces on every atom in a unit cell by calculation of the spatial distribution of the electrons from the Schrödinger equation. The theorem states:

$$\frac{dE_\lambda}{d\lambda} = \left\langle \psi_\lambda \left| \frac{d\hat{H}_\lambda}{d\lambda} \right| \psi_\lambda \right\rangle \quad (2.3.1)$$

This theorem was developed and proven by many people including Pauli, Hellmann and Feynman[112, 113, 114]. Feynman especially extended this to the calculation of intramolecular forces[114] in a molecule whereby equilibrium geometries could essentially be calculated. Firstly for a molecule with  $n$  electrons of which can vary between 1 and  $N$  with coordinates  $\mathbf{r}_i$  and  $m$  nuclei of which can vary between 1 and  $M$  with a nuclear charge of  $Z_\alpha$  at coordinates  $\mathbf{R}_\alpha = (X_\alpha, Y_\alpha, Z_\alpha)$  the Hamiltonian can be described as:

$$\hat{H} = \hat{T} + \hat{U} - \sum_{n=1}^N \sum_{\alpha=1}^M \frac{Z_\alpha}{|\mathbf{r}_n - \mathbf{R}_\alpha|} + \sum_{\alpha}^M \sum_{\beta>\alpha}^M \frac{Z_\alpha Z_\beta}{|\mathbf{R}_\alpha - \mathbf{R}_\beta|} \quad (2.3.2)$$

We can then describe a molecular force on a given nucleus by the negative of the derivative of the energy with respect to the given coordinate, which is described above in 2.3.1:

$$F_{X_\gamma} = -\frac{\partial E}{\partial X_\gamma} = -\left\langle \psi \left| \frac{\partial \hat{H}}{\partial X_\gamma} \right| \psi \right\rangle \quad (2.3.3)$$

If we then place our Hamiltonian into this equation and differentiate:

$$\frac{\partial \hat{H}}{\partial X_\gamma} = \frac{\partial}{\partial X_\gamma} \left( - \sum_{n=1}^N \sum_{\alpha=1}^M \frac{Z_\alpha}{|\mathbf{r}_n - \mathbf{R}_\alpha|} + \sum_{\alpha}^M \sum_{\beta>\alpha}^M \frac{Z_\alpha Z_\beta}{|\mathbf{R}_\alpha - \mathbf{R}_\beta|} \right) \quad (2.3.4)$$

$$= - Z_\gamma \sum_{n=1}^N \frac{x_n - X_\gamma}{|\mathbf{r}_n - \mathbf{R}_\gamma|^3} + Z_\gamma \sum_{\alpha \neq \gamma}^M \frac{X_\alpha - X_\gamma}{|\mathbf{R}_\alpha - \mathbf{R}_\gamma|^3} \quad (2.3.5)$$

applying this to 2.3.1 will return us a force for the component associated with  $X_\gamma$  on the nucleus in terms of the electronic density which can be solved through the self-consistent method, the nuclear charge and electronic coordinates:

$$F_{X_\gamma} = Z_\gamma \left( \int d\mathbf{r} \rho(\mathbf{r}) \frac{x_n - X_\gamma}{|\mathbf{r}_n - \mathbf{R}_\gamma|^3} - \sum_{\alpha \neq \gamma}^M Z_\alpha \frac{X_\alpha - X_\gamma}{|\mathbf{R}_\alpha - \mathbf{R}_\gamma|^3} \right) \quad (2.3.6)$$

Ultimately by reducing the forces to zero we can find the minimum energy associated with the molecule. Its important to note also that Pulay forces can arise in structures with an incomplete basis set, this can cause slow convergence and accuracy issues with lattice parameters. Pulay forces can be reduced by increasing the plane-wave cutoff when using such a DFT code.

## DFPT Methodology

Density functional perturbation theory (DFPT) is a methodology which perturbs the quantum mechanical description of a system by adding *minor*<sup>1</sup> disturbances. By taking the simplest answer for a system (usually the ground state), we can add small disturbances to the Hamiltonian which can give rise to certain properties which account as *corrections*. DFPT is an excellent methodology in being able to determine the vibrational, thermodynamic or spectroscopic properties of a material. Using everything that we have discussed previously we can determine perturbation theory is based on:

$$V_\lambda(\mathbf{r}) = V_0(\mathbf{r}) + \sum_i \lambda_i v_i(\mathbf{r}), \quad (2.3.7)$$

<sup>1</sup>The perturbations have to be small due to several complications which are involved in large disturbances. These large disturbances not only can be difficult to calculate by sometimes bring about non-numerical answers or cannot be answered via perturbation

we also know that the minimum energy from density functional theory is found by:

$$E(\lambda) = \left( F[n] + \int V_\lambda(\mathbf{r}) n(\mathbf{r}) d\mathbf{r} \right) \quad (2.3.8)$$

$$\int n(\mathbf{r}) d\mathbf{r} = N, \quad (2.3.9)$$

where  $N$  is the number of electrons. This is what we know from DFT. We also know from the Hellman-Feynmann theorem that the derivative of the minimum energy is found by:

$$\frac{\partial E(\lambda)}{\partial \lambda_i} = \int n_{\lambda_i}(\mathbf{r}) v_i(\mathbf{r}) d\mathbf{r} \quad (2.3.10)$$

Finally DFPT is based on the second order perturbation of a ground state:

$$\frac{\partial^2 E(\lambda)}{\partial \lambda_i \partial \lambda_j} = \int \frac{n_{\lambda_j}(\mathbf{r})}{\lambda_j} v_i(\mathbf{r}) d\mathbf{r}, \quad (2.3.11)$$

where  $\lambda_i, j$  is the perturbation. Determining in what is needed to be extracted in terms of results will determine the different type of perturbation theory methodology which is employed. For example:

- 1<sup>st</sup> **order**: forces, stresses, dipole moment ...
- 2<sup>nd</sup> **order**: phonon dynamical matrix, elastic constants, dielectric susceptibility, Born effective charges, piezoelectricity and internal strain

As shown above when looking for a ground state structure the phonon dynamical matrix is needed and thus DFPT must be employed. It is possible to go to third-**order** perturbations but for this thesis we do not need any of these. In this thesis we have made use of DFPT as our method of looking at phonons due to its low time and computational cost. Other methods can include the finite displacement method but this requires more structures to be processed to give an accurate result. Both methods were employed in the lead up to the results that were

## 2.4 Post-Processing Methods

Density Functional Theory is the first step in understanding the structures that we have put forward in this thesis. Once we have a suitable candidate for our ground

state structures there are several steps that are taken to determine the properties of the structure. We can continue to use Density Functional Theory to measure the various electronic properties of the materials or we can use other post-processing tools to calculate structural distortions. By combining both these methods together we can observe how the structural distortions can affect the electronic properties. In this research we carried out the post-processing using various online tools including ISODISTORT[115], FINDSYM[116] and INVARIANTS[117].

All three of these programs were vital in us being able to determine the origins of distortions within different structures. The distortions in our structures are labelled via Irreducible Representations (IRREPS). Irreps are used to represent the *degrees of freedom* that are present in the parent structure (In our case this was almost exclusively the  $Pm\bar{3}m$  structure) and thus have a rigid and clear description of what is happening during a parent-daughter transition. Irreps in our cases will be exclusive to particular distortions due to our parent space group being consistent across calculations and analysis. Therefore two structures that have identical irreps will have identical stereochemical distortions. The three programs carry out unique roles in our ability to understand the distortions present in the structures.

FINDSYM is used to determine the space group of our structures and are used in the creation of a crystallographic information file (CIF) which describes the symmetry present in the structure. ISODISTORT is a program in which identifies the irreps which drive the phase transition between a parent-daughter structure. This further allows us to identify the particular ions which are moving for each distortion and subsequently identifies any changes in the lattice parameters of the structure. ISODISTORT also allows us to change the size of the distortions which was vital in our understanding of how electronic structures change based on the size of the distortions. INVARIANTS was the final program used, its purpose, to determine how certain irreps and thus distortions couple together. This allowed us to determine which distortions drive phase transitions between parent-daughter structures and allowed us to recognise which distortions can lead to subsequent more interesting electronic distortions.

## Process

The process involves taking the raw data of the structures created and putting them into DFT to relax. This relaxation is done with strict convergence criteria which focuses on the energy, forces and internal pressure of the system. The initial calculations was looking for the ground state structure/energies of the system, from this it is possible to look for subsequent structures using the DFPT method. This is also where we employed other methodologies to find the electronic properties of the structures, more commonly the bandstructures of the materials. Once all parent and daughter structures have been created the post-processing symmetry analysis can be carried out.

As described by 2.6 the first step is to employ the online program FINDSYM which allows us to determine the space group of the structure that is being used. This would also produce a CIF File for subsequent use in the following programs. CIF files are then used in ISODISTORT to determine the irreps that appear within the phase transition of the parent-daughter structures. INVARIANTS in combination with ISODISTORT will produce the coupling terms that we describe further on in the thesis.

## 2.5 Conclusion

In this section we have discussed the underlying theory involved in the creation of the results of this work. Density Functional Theory plays the key role in our understanding of the structural-electronic diversity we can create with perovskite like materials. We delved into our understanding of the key principles involved with DFT including the exchange-correlation functional and its clear importance in the calculations, the different types of pseudopotentials that can be employed and the quite beautiful way in which we can take a single unit cell and apply this across an infinite bulk system through Blochs' Theorem. We finally discussed some of the post-processing tools used including Hellman-Feynmann Theorem, DFPT and the symmetry analysis tools.

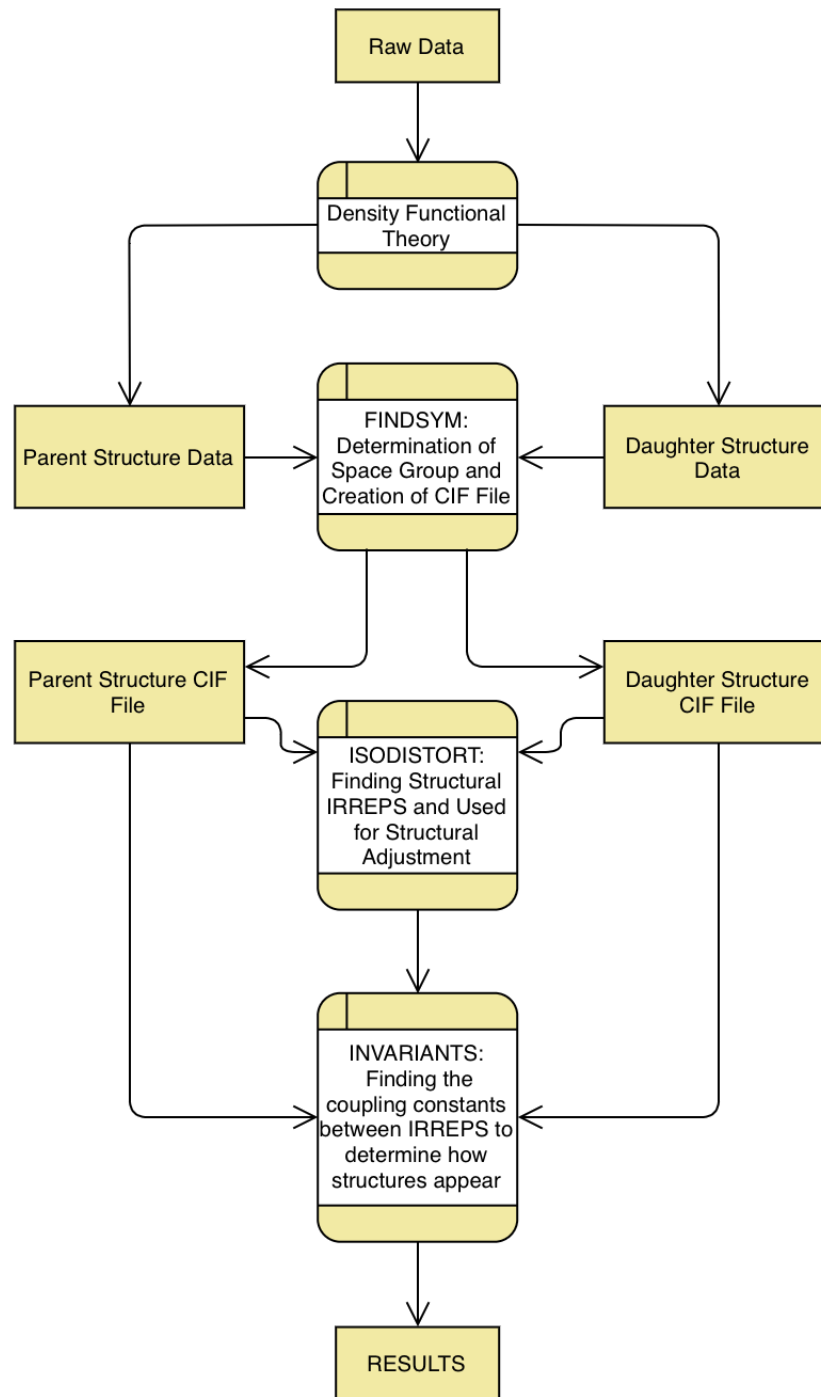


Figure 2.6: Flow chart of the process of taking raw data through DFT to the completed structural analysis of ground state structures.

# The Structural Complexity of Gold Halide Double Perovskites

*No matter what you look at, if you look at it closely enough, you are involved in the  
entire universe.*

- Michael Faraday

### 3.1 Introduction

**T**he nature and structural order of perovskites and perovskite like materials allow for incredibly diverse and complex electronic properties. The corner sharing octahedra allow for diverse structural changes which subsequently lead onto interesting electronic properties. There has been extensive research carried out on layered perovskite structures and all show interesting.

#### Competition vs. Cooperation

In all perovskite and perovskite like structures there is generally a certain degree of competition or cooperation between structural distortions. Competition between structural distortions can be defined as the two distortions working against each other (distortion A competes with distortion B and *wins*, therefore distortion A becomes prevalent and distortion B is less likely to appear). In cooperation the two distortions will work in tandem with each other (distortion A appears and thus distortion B is more likely to appear. If one increases in size the other will also). Of course, this is an over simplified model but these rules will apply to most distortions in all perovskite structures. The two distortions that are known to compete with each other is the tilt/rotation of the octahedra and any one of the different variants of polar distortion and will rarely coexist in the same crystal. Understanding the phenomena has become an active area of research and there are many examples of the competition between these two distortions.

Work carried out by J. Gazquez *et al.* on the  $\text{LaAlO}_3/\text{SrTiO}_3$  system excellently described the competition between Antiferrodistortive (AFD) tilts and rotations and the polar ferroelectric modes and then using quantum confinement to selectively stabilise either of the modes[118]. We can also examine various ferroelectric distortions like  $\text{PbTiO}_3$  and  $\text{BaTiO}_3$  where tilt distortions do not appear. This competition is not confined to simpler  $\text{ABX}_3$  structures, but layered structures, for example, are also subject to competition between polar and non-polar distortions. In the Ruddlesden-

Popper ( $A_2B_3X_7$ ) layered  $Li_2SrNb_2O_7$  structure both the polar ( $A2_1am$ ) and antipolar ( $Pnam$ ) phases are energetically lower than the centrosymmetric ( $Amam$ ) and phase transitions between the two phases at 90K[119]. Like with the competition between the tilt and polar mode there also exists competition between polarisation, magnetism and strain[120]. There has been some exploration in the research world of competition/cooperation in the field of double perovskites. For example, in the vacancy ordered double perovskites there is an increase in cooperative octahedral tilting when there is a reduction in the tolerance factor of the structure[121]. On the other hand although there is generally a large competition between the octahedral rotations and ferroelectricity in perovskite compounds work from Aschauer and Spaldin have shown that at much larger angles for the rotations, the ferroelectric instability can be strengthened[122].

### Gold Double Perovskites

In both this and the next chapter we will be focusing on the Gold Halide double perovskites. The Gold double perovskites follow the structure  $A_2Au_2X_6$  ( $A=Cs, Rb, K$ ;  $X=Cl, Br, I$ ). These structures were primarily chosen due to their promising photovoltaic properties but as we explored more we found a rich and complex structural world in which through tuning of the size of the distortions through external parameters such as the E-fields, ion size and pressure we could create materials that could be used for photoferroics. The gold double perovskite structures have recently garnered more attention due to their exciting photo-electronic properties. Debbichi *et al.* explored such electronic properties and found a more than suitable band-gap of 1.31eV with excellent absorption in both single and poly-crystal structures[123]. Although a lot of the recent research has been computational such structures have been synthesised e.g,  $Cs_2Au_2I_6$  ( $I4/mmm$ )[124],  $Cs_2Au_2Br_6$  ( $I4/mmm$ )[125],  $Rb_2Au_2I_6$  ( $C2/m$ )[126],  $Rb_2Au_2Br_6$  ( $I2/m$ )[127] and  $K_2Au_2I_6$  ( $P2_1/n$ ) [128]. The work conducted by these experimentalists already show a diverse range of structural phases that can appear through changing ion size and thus tolerance factor. All structures were originally

analysed based on the tetragonal  $I4/mmm$  phase which arises from two main distortions when analysis of the cubic phase takes place (the coupling between these two distortions will be carried out in more detail further on in the chapter).

For the purpose of this study we will focus specifically on the octahedral complexes.

For any given octahedral complex we have five  $d$  atomic orbitals ( $d_{xy}, d_{xz}, d_{yz}, d_{z^2}, d_{x^2-y^2}$ ) and these can subsequently then be split into two categories due to the octahedral crystal field. The first three correspond to the  $t_{2g}$  symmetry label and the final two correspond to the  $e_g$ , the  $e_g$  and  $t_{2g}$  split in the gold double perovskites when we remove the degeneracy either through elongation of the  $z$ -axis bonds or compression of the  $z$ -axis bonds.

In the double perovskite structure in this study we find disproportional charges on the Gold sites and this causes a Jahn-Teller like distortion to appear. One site contains a  $d^8$  and the other a  $d^{10}$ , and this therefore forces a change in the geometry of the octahedral cages. Au(III)  $d^8$  atoms will therefore allow for a square-planar molecular shape, this leads to the  $z$  ligands moving further from the Au-atom with the  $x$ - $y$  moving closer. This forces the  $z$ -component orbitals to lower in energy and the  $x$ - $y$  to increase as we see orbital splitting. Electrons will fill from the lowest energy to highest orbitals however on the  $d^8$  gold site the  $d_{x^2-y^2}$  will not be filled due to the large destabilisation and its more favourable to the electrons to sit in the  $d_{xy}$ . Not only does this cause a geometric distortion to remove the degeneracy into the square-planar (Figure 3.2), but it also means that our system is diamagnetic as all of the electrons in the orbitals will be paired spin up-spin down.

Figure 3.1 shows the schematic of the  $I4/mmm$  phase which contains only Jahn-Teller like distortion and a breathing distortion. Not only is the Jahn-Teller distortion present in these kind of materials but a breathing distortion also. A breathing distortion occurs geometrically from the linear expansion or contraction of the octahedral cage, it occurs in strongly correlated materials due to strong interaction between electrons. This causes charges to localise on different sites thus causing the geometric expansion and contraction of our octahedral cages. This effect has been shown to

trigger metal-insulator transitions in the rare-earth Nickelates[129].

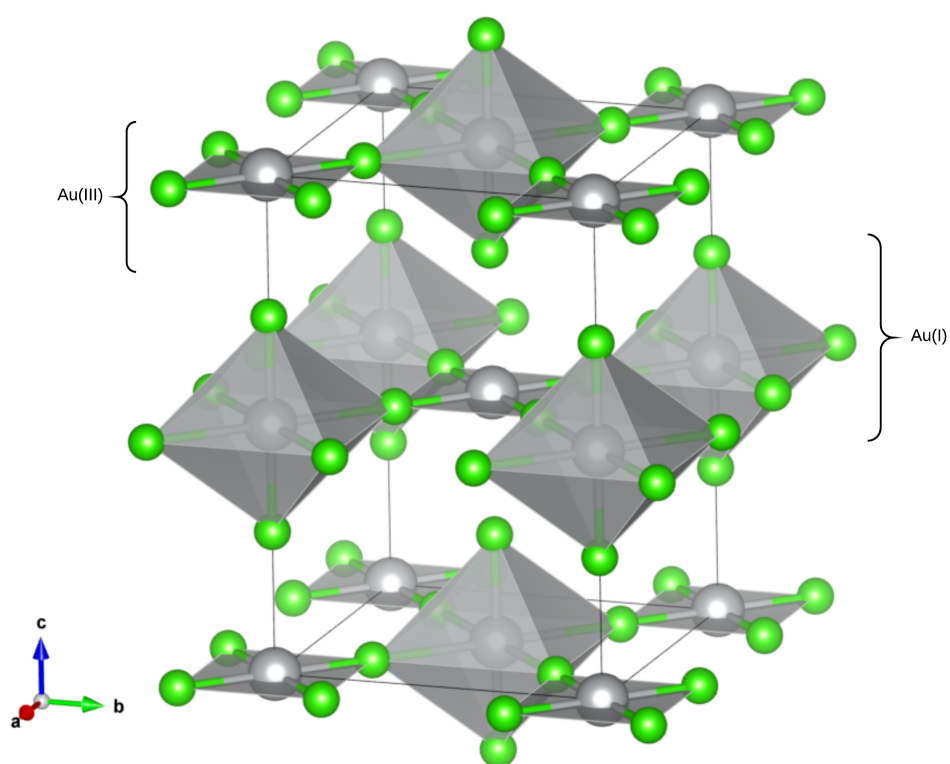


Figure 3.1: Low-symmetry  $I4/mmm$  phase which shows clearly the Jahn-Teller like effect in the  $A_2Au_2X_6$  structure with a rock-salt like ordering of the square-planar and octahedral geometries.

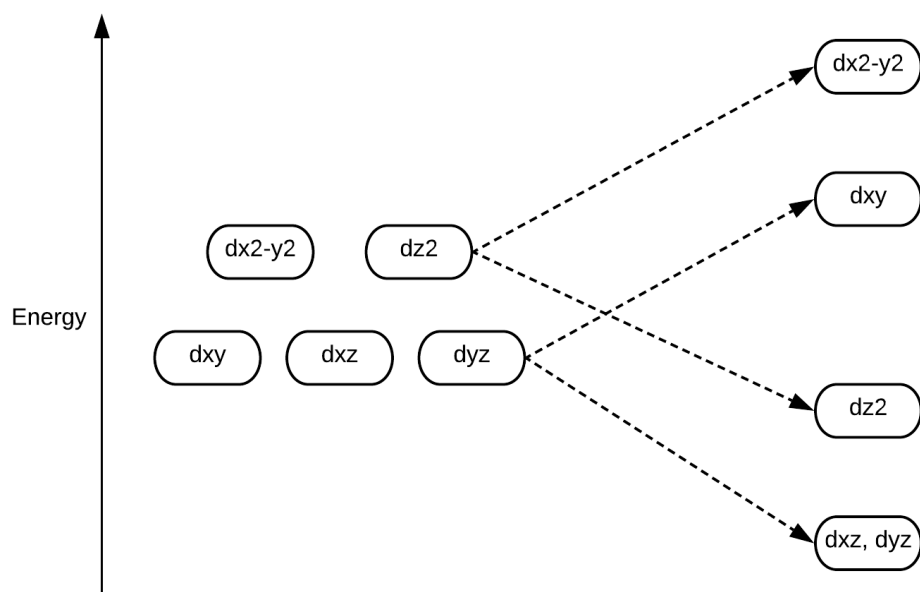


Figure 3.2: Schematic of the field splitting from the octahedral ( $O_h$ ) geometry to the square-planar ( $D_{4h}$ ), clearly showing the destabilisation of the  $d_{x^2-y^2}$  orbital.

## 3.2 Computational Methods

We employed ab initio methods based on Density Functional Theory (DFT) in combination with post-analysis tools. Here, the VASP (Vienna ab initio Simulation Package) DFT code was utilised [130, 131, 132, 133] with PAW (Projector Augmented Wave) pseudopotentials[110, 134], and the Generalised Gradient Approximation (GGA) exchange-correlation functional PBESol[135]. The 5s5p6s, s1d10, s2p5 electrons were treated as valence for the A, Au and X-sites respectively. An energy cutoff of 700eV was used for the plane-wave basis, and a  $2 \times 2 \times 3$  MonkhorstPack grid [136] for the 20-atom unit cell. Symmetry mode analysis was performed with AMPLIMODES[137, 138], ISODISTORT[139] and FINDSYM[116]. We employed the Density Functional Perturbation Theory (DFPT) method to determine dynamical instabilities and calculate static ionic dielectric constants[140] with energies minimised to  $10^{-9}$  eV and forces minimised to  $10^{-6}$  eV/Å. Throughout this body of work the parent space group was kept consistent ( $Pm\bar{3}m$ ). This was done for two reasons: 1) all of the subsequent daughter phases were derived from the cubic  $Pm\bar{3}m$  and 2) the subsequent irrep labels which correspond to our structural distortions would be consistent no matter what daughter phase was being investigated. This would subsequently mean that comparisons could be made between key structural distortions that appear in all daughter phases. Bandstructure, density of states and effective masses within the next chapter were determined using the sumo package[141].

## 3.3 Results

### Analysis of the Tetragonal Phases and Phonons

As previously discussed there has been some extensive experimental and computational work carried out on the different structures of the gold double perovskites. We begin our journey here at the most basic and fundamental structure. The simple cubic  $\text{CsAuI}_3$  ( $Pm\bar{3}m$ ), where Density Functional Perturbation Theory (DFPT) was im-

plemented to analyse the phonons. Three dynamical instabilities are present at the M (0.5,0.5,0), R (0.5,0.5,0.5) and X (0,0.5,0) point[142]. Figure 3.3 shows the phonon dispersion across the four high symmetry points and the structural instabilities are the three points that are below the zero-line. When the eigenmodes are frozen into

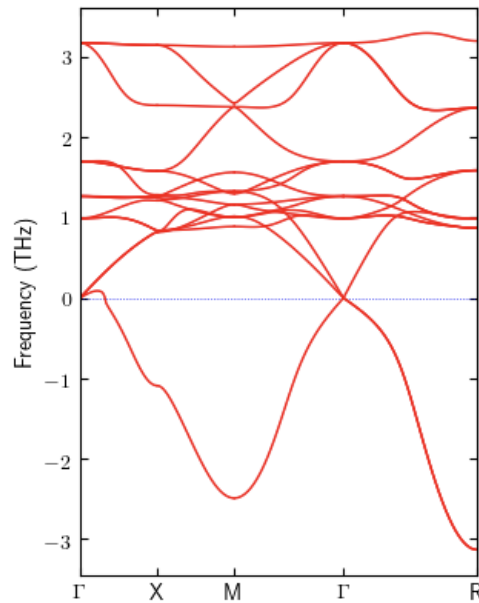


Figure 3.3: Phonon dispersion of the CsAu<sub>3</sub> structure. A 2x2x2 supercell was used to highlight the key symmetry points R, X and M.

the cubic structure a full DFT structural relaxation was carried out and this showed us that the structure with the R-point dynamical instability has the lowest energy (we speak more about the determination of the ground state phase later). This structure is identical to the  $I4/mmm$  phase that was synthesised by Matsushita *et al.* [124]. Analysis through ISODISTORT shows that there are four individual distortions that are present. Due to the transition from cubic to tetragonal there are both hydrostatic and tetragonal strains present (labelled with the  $\Gamma_1^+$  and  $\Gamma_3^+$ , respectively) and two R-point distortions, one of which is the primary mode and drives the phase transition and the other is a secondary mode. Figure 3.4 shows the octahedral distortions

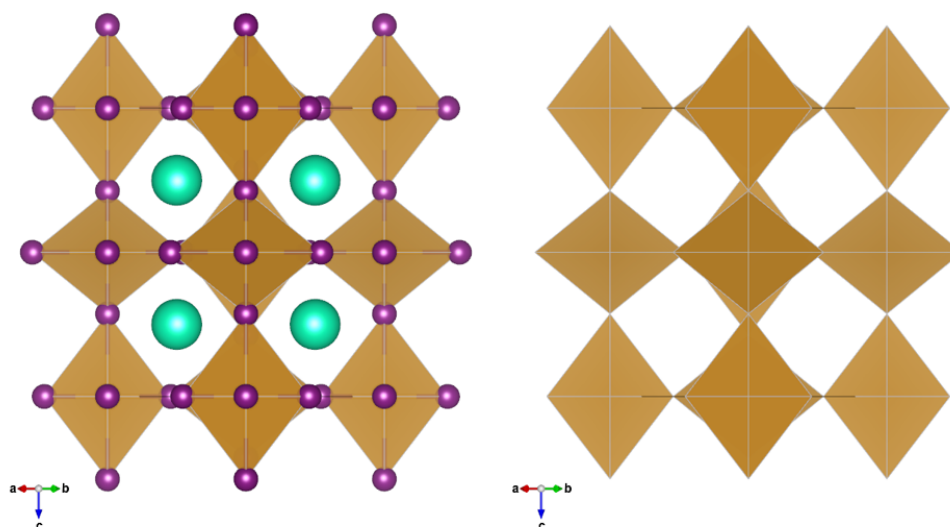


Figure 3.4: The  $\text{Cs}_2\text{Au}_2\text{I}_6$  structure (*left*) with all of the atoms included and (*right*) with the atoms removed for clarity on the octahedral structure (where the A-site cation caesium is represented by blue. The purple anions are represented by iodine and the gold cations sit within the gold octahedral cages).

present in the  $I4/mmm$  phase. This elongation and compression in a rock-salt order is associated with a Jahn-Teller like distortion (labelled  $R_3^-$ ) where on the  $d^8$  gold sites we see four short bonds in the  $x - y$  direction and two long in the  $z$  direction and on the  $d^{10}$  gold sites we see a smaller lengthening of the bonds in the  $x - y$  direction and a small shortening in the  $z$  direction. Through ISODISTORT we can see another distortion which is characterised by expansion and compression of the octahedral cages as a whole (breathing distortion  $R_2^-$ ). This distortion arises in transition metal chemistries where charges localise on different sites. Breathing distortions appear often in transition metal oxides such as the rare-earth nickelates[129]. Analysis of the amplitudes of these distortions shows that this breathing distortion is very small and is difficult to visualise. We can however, see changes in the size of the bond-lengths which proves to us that this distortion is a physical phenomena rather than from numerical noise. In order to determine the true sizes of the distortions in the structures we used two methods to determine the true ground state energy was implemented.

As previously mentioned a full structural relaxation was implemented to determine the lowest energy state but we also plotted the energy for various sizes of the volume to determine the lowest energy point in relation to the volume. The curve was then fitted to the Murnaghan equation of state[143, 144]:

$$E(V) = E_0 + B_0 \frac{V}{B'} \left( \frac{(V_0/V)^{B'}}{B'-1} + 1 \right) - \frac{B_0 V_0}{B'-1} \quad (3.3.1)$$

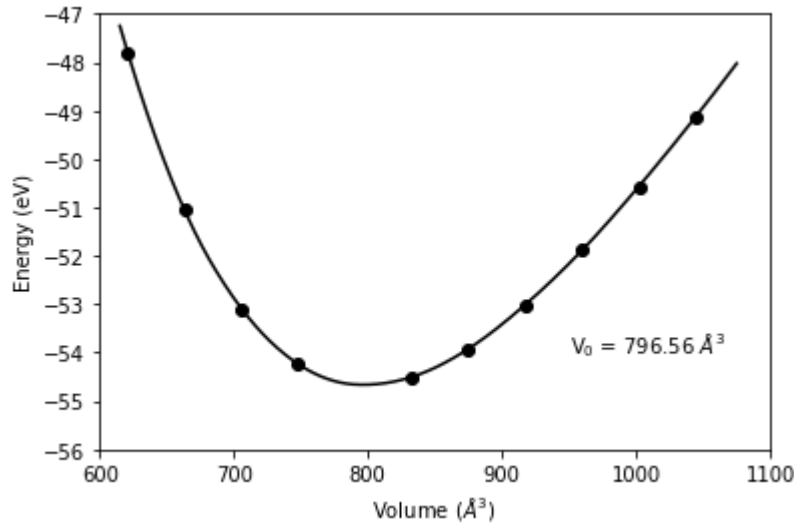


Figure 3.5: Volume-Energy curve of the  $\text{Cs}_2\text{Au}_2\text{I}_6$   $I4/mmm$  phase which is fitted to Murnaghan equation of state. The optimal volume of our structure is displayed above as  $V_0$ .

Figure 3.5 shows the relationship between the volume of the unit cell and the overall energy of the system. Here  $V_0$  corresponds to our ground state volume. The difference in the volume between this methodology and the volume in structural relaxation methodology is negligible. The energies however will be slightly different due to the additional movement of the ions within that now rigid unit cell. The main reason for making this comparison is to determine the accuracy of our input parameters for DFT whilst also striking the balance for computational expense. This Murnaghan method is also more rigid when looking at structures in which there is not any exper-

imental parameters to compare to. It was important to understand which of these two R-point distortions was primary and as such through DFT calculations we were able to determine that the  $R_3^-$  Jahn Teller distortion is the one primary distortion. It is this distortion which drives the phase transition  $Pm\bar{3}m \rightarrow I4/mmm$  with the breathing distortion appearing as a secondary order parameter. Condensing the  $R_3^-$  mode singularly into our cubic structure we observe the phase transition occurs with the introduction of the  $R_2^-$  breathing distortion. Through ISODISTORT we froze the  $R_2^-$  mode into the system without the  $R_3^-$  distortion we found that the distortion disappears completely. This combined with the INVARIANTS analysis below we can deduce that the Jahn-Teller  $R_3^-$  is the primary order parameter. In the following chapter we will show the effects of metal  $\rightarrow$  non-metal electronic phase transition which happens when we introduce these modes individually. INVARIANTS analysis shows the coupling terms between these distortions and we highlight the coupling term which lowers the energy sufficiently to drive this phase transition:

$$F \propto -C_{01} Q_{R_3(a,0)^-}^3 - Q_{R_2(a)^-} + A_{10} Q_{R_3(a,0)^-}^2 - Q_{R_2(a)^-}^2 \quad (3.3.2)$$

Here we have highlighted the coupling term which drives this phase transition (Full equation in Appendix A). Interestingly this coupling term is identical to the one which drives the ferroelectric phase transition in the  $YMnO_3$  where the  $K_3$  rotation distortion couples cubic-linearly to the ferroelectric mode[145]. As we will see further on this Jahn-Teller distortion acts as the catalyst for all of the other distortions that appear in the different structures.

Our first step was to look at changing the ion size in the structure to subsequently see how the amplitude of the distortions changed. Phonon calculations were carried out on the  $Cs_2Au_2(I, Br, Cl)_6$   $I4/mmm$  phases and it was found all structures were dynamically stable with the  $I4/mmm$  phase being the ground state structure for all. Table 3.1. shows the effects of ion size on the size of the distortions. Comparison of ion sizes is done through the tolerance factor[38]:

$$t = \frac{r_A + r_X}{\sqrt{2}(r_B + r_X)} \quad (3.3.3)$$

Analysis of the  $\text{Rb}_2\text{Au}_2\text{Cl}_6$  structure also gives us a dynamically stable  $I4/mmm$  but

Chemistry	Tolerance Factor	Irreps	Amplitude (Å)
$\text{Cs}_2\text{Au}_2\text{Cl}_6$	0.92	$\begin{pmatrix} R_2^- \\ R_3^- \end{pmatrix}$	$\begin{pmatrix} 0.10 \\ 0.79 \end{pmatrix}$
$\text{Cs}_2\text{Au}_2\text{Br}_6$	0.91	$\begin{pmatrix} R_2^- \\ R_3^- \end{pmatrix}$	$\begin{pmatrix} 0.06 \\ 0.69 \end{pmatrix}$
$\text{Cs}_2\text{Au}_2\text{I}_6$	0.90	$\begin{pmatrix} R_2^- \\ R_3^- \end{pmatrix}$	$\begin{pmatrix} 0.03 \\ 0.61 \end{pmatrix}$

Table 3.1: The effects of ion size on the the size of the Jahn-Teller and breathing distortions with respect to the cubic  $\text{Pm}\bar{3}m$ . All Irreps are with with respect to the cubic  $\text{Pm}\bar{3}m$  with the A-site cation at the origin.

as we move beyond this and our tolerance factor gets smaller we see a change in the ground state structure of lower tolerance factor structures from the  $I4/mmm$  to the  $C2/m$ . By adjusting the different structures systematically by changing individual elements and thus ion size in the structure we can adjust the tolerance factor. It is clear that a lower tolerance factor can enable the appearance of different distortions in a perovskite structure. This was employed as our method of choice to try and determine if more distortions would subsequently appear. This also allowed an exploratory method to observe all of the different gold perovskite structures that can appear experimentally and the distortions that appear in them. We employed a method of substituting elements in our structure and looked at the subsequent phonons that appear in the  $I4/mmm$  phase. We then looked at the energies associated with freezing in the eigenmodes and compared ground state energies to find the subsequent ground state structures.

### Analysis of the Tilted Phase

As we decrease the tolerance factor we begin to see some of the competition between the polar and tilt phases appear. For example when we analyse the  $\text{Rb}_2\text{Au}_2\text{I}_6$   $I4/mmm$  phase phonons we find a series of distortions as shown in Table 3.2. Each of these eigenmodes were frozen into the system and relaxed to find the ground state

energy. These energies were then compared to find the ground state structure. As shown in Table 3.2 the  $C2/m$  structure had the lowest overall energy. When decom-

Frequency ( $\text{cm}^{-1}$ )	$\Delta E$ (eV)	Irreps	Space Group
-2.39	-2.11	$X_5^+, M_5^-$	$P2_1/m$
-3.35	-11.51	$R_4^-, R_5^-$	$C2/m$
-5.83	-2.64	$R_5^+$	$Cm$
-6.74	-0.06	$M_3^-$	$P4_2/nmc$
-10.48	-7.67	$R_4^-$	$Immm$
-15.15	-0.60	$\Gamma_4^-, R_5^+$	$I4mm$

Table 3.2: Information on each phonon instability that is found in  $I4/mmm$   $\text{Rb}_2\text{Au}_2\text{I}_6$  phase. All Irreps are with respect to the cubic  $Pm\bar{3}m$  with the A-site cation at the origin.

posing the Irreps in the  $C2/m$  phase we see two distortions added, namely the  $R_4^-$  and  $R_5^-$  which correspond to an anti-polar distortion and tilt distortion respectively. The  $R_4^-$  mode has an order parameter direction (a,b,b) with the tilt distortion  $R_5^-$  with an order parameter direction of (0,a,-a). I will discuss further the importance of the order parameter directions later on when we discuss the coupling between the modes. Through DFT and ISODISTORT we determined that the primary order parameter is the  $R_5^-$  tilt distortion with the  $R_4^-$  arising as a secondary order parameter. This was carried out in a similar way to the breathing and Jahn-Teller distortions in the cubic to tetragonal phase transition, by artificially reducing these distortions to 0 and relaxing the structure. We see that with the  $R_5^-$  distortion the  $R_4^-$  reappears but with the opposite we see the  $R_5^-$  also disappear. The size of the distortions as shown in Table 3.3 show the same picture with the tilt distortion being considerably larger than that of the anti-polar. Visualising the  $C2/m$  phase (Figure 3.7 we can see clearly the tilt distortions. Here a singular tilt distortion around the two in-plane axes corresponding to a glazer notation of ( $a^- a^- c^0$ ).

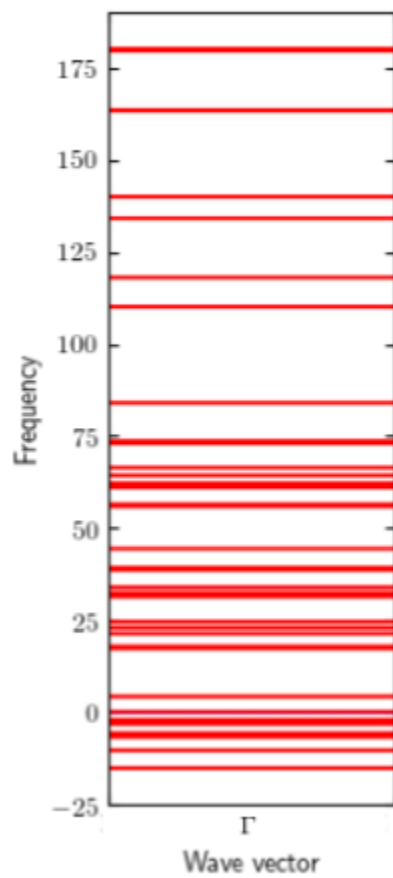


Figure 3.6: Phonon dispersion curve for the  $\text{Rb}_2\text{Au}_2\text{I}_6$  structure showing clear instabilities present in the structure - Instabilities with the corresponding irreducible representations are shown in Table 3.2. Structurally due to size of the crystal itself the phonons are all at the  $\Gamma$  point.

Chemistry	Tolerance Factor	Irreps	OPD	Amplitude (Å)
$\text{Rb}_2\text{Au}_2\text{I}_6$	0.87	$R_2^-$	$(a)$	$(0.06)$
		$R_3^-$	$(a, b)$	$(0.73)$
		$R_4^-$	$(a, b, b)$	$(0.16)$
		$R_5^-$	$(0, a, -a)$	$(0.73)$

Table 3.3: Irrep decomposition of the  $C2/m$   $\text{Rb}_2\text{Au}_2\text{I}_6$  phase with respect to the cubic  $Pm\bar{3}m$  (A-site cation at the origin) phase shows two extra distortions present.

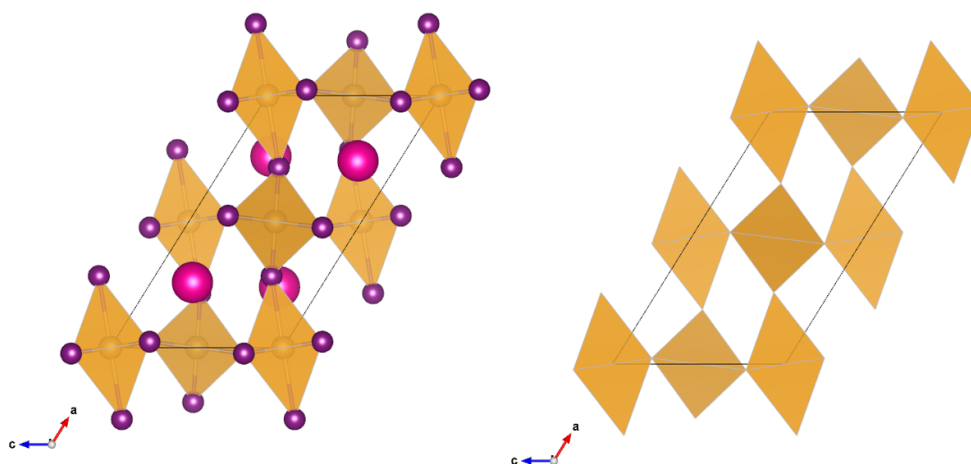


Figure 3.7: Schematic of the  $\text{Rb}_2\text{Au}_2\text{I}_6$   $C2/m$  phase showing the tilt distortions present. The A-site pink cations represent the Rubidium, the X-site purple anions represent the iodine and the B-site gold cations are found inside the gold octahedral cage.

We subsequently carried out an INVARIANTS analysis of the phase transition between the high symmetry  $Pm\bar{3}m$  structure and the low symmetry  $C2/m$  structure:

$$\begin{aligned}
 (F - F_0) \propto & \\
 & + \gamma_{3(a),(b),4} (Q_{R_4-(a)}^3 Q_{R_5^-} - Q_{R_4-(a)} Q_{R_4-(b)}^2 Q_{R_5^-}) \\
 & - C_{123(c),4} Q_{R_2^-} Q_{R_3^-} Q_{R_4-(a)} Q_{R_5^-} - C_{23(c,d),4} Q_{R_3^-} Q_{R_4-(a)} Q_{R_4-(b)} Q_{R_5^-} \quad (3.3.4)
 \end{aligned}$$

In comparison to the previous INVARIANTS analysis we did for the  $Pm\bar{3}m \rightarrow I4/mmm$  phase transition we see a much more complex interplay between the distortions for the  $Pm\bar{3}m \rightarrow I4/mmm$  phase transition. Whereas in the previous section we had coupling between singular order parameters of our two distortions the  $R_2^-$  and the  $R_3^-$  in this INVARIANTS analysis we see a complex coupling between distortions that act in different directions, see equation A.2.2 for the coupling between the  $a$  and  $b$  directions of the  $R_4^-$  for example. In the full expansion we observe the cubic-linear coupling term which enables the structural phase transition from the cubic to tetragonal structure, this is the coupling term which ultimately leads to the appearance of the  $R_4^-$  and  $R_5^-$  modes. Highlighted in our free-energy expansion are the two quad-linear terms. One quad linear term couples with the  $R_2^-$ ,  $R_3^-$ ,  $R_5^-$  and the  $R_4^-(a)$ , with the second being with the  $R_3^-$ ,  $R_4^-(a)$ ,  $R_4^-(b)$  and  $R_5^-$ . I have included the majority of the key coupling terms in the free-energy expansion above but for the full expansion with all of the key order parameters directions please refer to equation in Appendix A.

Unfortunately due to the presence of this structural phase transition in the phonon dispersion it is not possible to outright produce a strong polar structure. Further exploration of different structures shows that as we move even further down in tolerance factor we still fall into the same  $C2/m$  structure. For all structures from  $\text{Rb}_2\text{Au}_2\text{Br}_6$  down to  $\text{K}_2\text{Au}_2\text{Br}_6$  we observe them in the  $C2/m$  phase with all order parameter directions identical. The final step of our exploration was examining the final structure  $\text{K}_2\text{Au}_2\text{I}_6$ . Much like the other two structures that we have done a rigorous analysis (due to the fact they are experimentally proven) the  $\text{K}_2\text{Au}_2\text{I}_6$  falls into an even more complex phase, the  $P2_1/c$  space group.

### Low Symmetry Phase

When our tolerance factor gets sufficiently low enough we can observe an overtly more complex structure. This phase has not been explored in great detail but experimentally it has been produced[128]. Figure 3.8 shows the increased number of distortions present in the  $K_2Au_2I_6$ . The distortions present in this structure have a large reliance on each other, as we discuss below. Not only do the four distortions initially discussed appear in this structure but a sequence of further distortions also appears. As shown above there is a large amount of distortions present in the ground

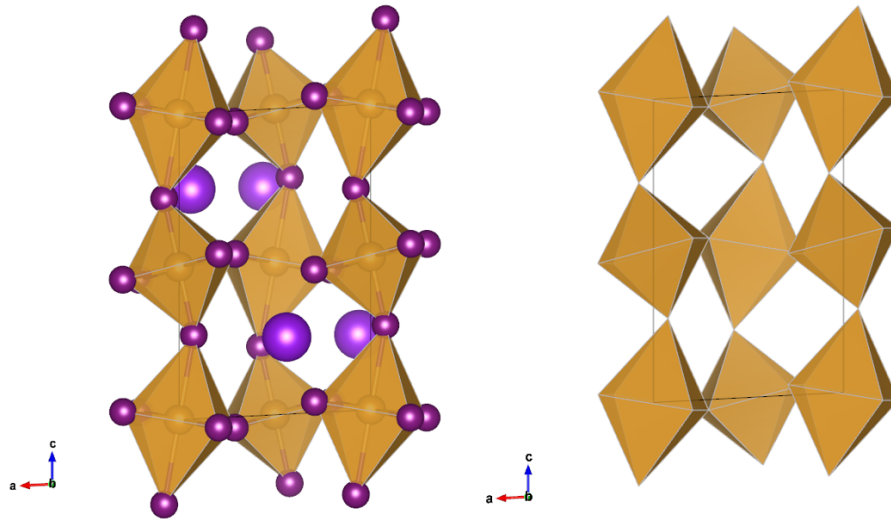


Figure 3.8: Schematic of the  $K_2Au_2I_6$  structure with the very clear anti-polar and tilt distortions present. Analysis of the modes shows the appearance of two tilt distortions.

state structure, this obviously therefore leads to a large Landau expansion with a lot of different terms coupling together. Our distortions in the low symmetry  $P2_1/c$  phase exhibit the following order parameter directions:  $R_2^-(a)$ ,  $R_3^-(a,b)$ ,  $R_4^-(a,0,0)$ ,  $R_5^-(a,0,0)$ . Here we can see some differences in this phase in comparison to previously explored phases: this includes the introduction of a non-zero change in the  $R_3^-(a,b)$ . We also

Chemistry	Tolerance Factor	Irreps	Amplitude (Å)
$\text{K}_2\text{Au}_2\text{I}_6$	0.83	$\begin{pmatrix} R_2^- \\ R_3^- \\ R_4^- \\ R_5^- \\ X_5^+ \\ M_5^+ \end{pmatrix}$	$\begin{pmatrix} 0.21 \\ 1.17 \\ 0.02 \\ 1.64 \\ 0.23 \\ 0.12 \end{pmatrix}$

Table 3.4: Irrep decomposition of the  $P2_1/c$   $\text{K}_2\text{Au}_2\text{I}_6$  phase with respect to the cubic  $Pm\bar{3}m$  (A-site cation at the origin).

see some differences in both the  $R_4^-$  and  $R_5^-$  with the much simpler (a,0,0) OPD for both of these phases. However, there is an introduction to two more distortions, both the  $X_5^+$  (a,0;b,0;0,0) and the  $M_5^+$  (a,b;0;0,0,0) distortion. Our landau expansion below shows the interaction between these different modes and OPD's. However due to the large amount of distortions a lot of the bi-quadratic terms have been omitted.

$$\begin{aligned}
 (F - F_0) = & \\
 & + C_{1,2,3,4} Q_{R_2^-} Q_{R_3^-(b)} Q_{R_4^-} Q_{R_5^-} + C_{2,2,3,4} Q_{R_3^-(a)} Q_{R_3^-(b)} Q_{R_4^-} Q_{R_5^-} \\
 & + C_{1,3,6,6} Q_{R_2^-} Q_{R_4^-} Q_{M_5^+(a)} Q_{M_5^+(b)} \\
 & + C_{1,3,6,6} Q_{R_3^-(a)}^2 Q_{X_5^+(a)} Q_{X_5^+(b)} \tag{3.3.5}
 \end{aligned}$$

As we can see from our landau expansion of the phase transition there are five particular sets of coupling that are of interest. First of all we see our trademark linear-cubic coupling term between the  $R_2^-$  and  $R_3^-$  (See Appendix A for full expansion), secondly we see the quad-linear coupling term between the  $R_3^-(a)$ ,  $R_3^-(b)$ ,  $R_4^-$  and  $R_5^-$ . Thirdly the appearance of the  $M_5^+$  both (a) and (b) is driven by the quad-linear coupling term between the  $R_2^-$  and  $R_4^-$  distortions with the final distortion appearing through a quadratic bi-linear coupling term between the  $R_3^-(a)$  and the (a) and (b) components of the  $X_5^+$ . We see an overall reduction in the complexity of the  $R_4^-$  and  $R_5^-$  with the OPD of both in only one direction. This could be due to symmetry requirements in order to induce the following tilt and anti-polar distortion. Distortions that are needed due to the tolerance factor reducing very significantly. Overall

there is a depth of distortions that are present in these structure which leads to a set of interesting electronic properties which will be discussed in the following chapter.

### Phase Diagram

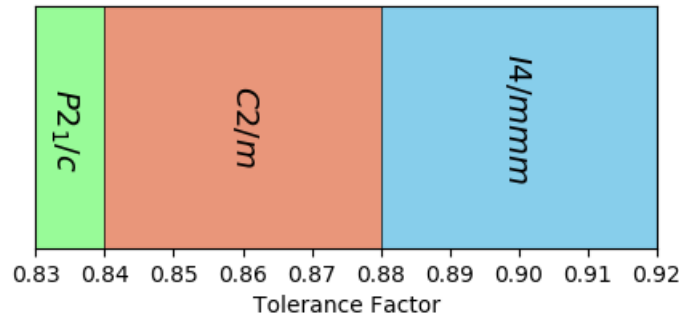


Figure 3.9: Basic phase schematic for the Gold double perovskite-like structures

Figure 3.9 shows how the space group changes with respect to the tolerance factor. We find that higher tolerance factors lead to a tetragonal space group, with lower tolerance factors introducing tilt distortions into the ground state structures. Analysis of all phases between the  $\text{Cs}_2\text{Au}_2\text{Cl}_6$  and the  $\text{Rb}_2\text{Au}_2\text{Br}_6$  show the symmetry does not change and phonon calculations shown that these systems are dynamically stable. As the tolerance factor becomes smaller we see the introduction of various other distortions including both polar and tilt. What this does highlight is the competition between these two types of distortions as the condensing of the tilt and anti-polar mode in the  $\text{Rb}_2\text{Au}_2\text{Br}_6$  and  $\text{Rb}_2\text{Au}_2\text{I}_6$  leads to the polar distortion hardening to a point it is no long an instability. Due to the general nature of the  $\text{K}_2\text{Au}_2\text{X}_6$  ( $\text{X} = \text{Cl}, \text{Br}$ ) and from analysis of literature it seems these structures have not been synthesised (most probably due to poor stability and degradation over a short amount of time) so we just looked at the ground state for these two. Finally we get to the lowest symmetry structure with two tilt distortions present which leads to a complex interplay between all of the distortions present in all structures up until this point. It is unfortunate that we were not able to find a ferroelectric ground state within these structures but due

to the instability appearing in the  $\text{Rb}_2\text{Au}_2\text{Br}_6$  and below we felt it would be interesting to explore this and in the next chapter we will explore ways we can use the polar instability to aid in charge separation.

## Polar Phase

### Proper

We find that when we look at the dynamical instabilities for the  $I4/mmm$   $\text{Rb}_2\text{Au}_2\text{Br}_6$  we find an instability that corresponds to a polar phase. This instability was initially a combination of the  $\Gamma_4^-$  polar distortion and the anti-polar  $R_5^+$  distortion. We of course wanted to determine the origin of this polar distortion and analyse its physical properties. After freezing in the eigenmodes and carrying out a full relaxation through DFT we do see that the polar distortion becomes very small and could be numerical noise, within the error of DFT. We do however also find that the size of the  $R_5^+$  also becomes considerably smaller. This could suggest two things, firstly, the system is proper ferroelectric and the polar distortion is real and the anti-polar distortion is a consequence of symmetry within DFT and therefore does not appear. Secondly, that both are real and the polar distortion appears through a trilinear coupling term. Here we discuss both options, It was therefore important to determine whether this distortion was physically real, or erroneous. Figure 3.10 shows how the energy of the system changes with respect to artificially changed strains and the Jahn-Teller distortion (the initial primary order parameter). In Figure 3.10 we highlight a couple of factors which lower the overall energy of the polar distortion. The top figure shows how the energy of a relative  $\Gamma_4^-$  distortion changes based on the percentage size of the strain with the Jahn-Teller, breathing and anti-polar removed. This strain includes both of the hydrostatic ( $\Gamma_1^+$ ) and the tetragonal ( $\Gamma_3^+$ ) strains. The percentage is relative to the maximum value of both based off of the  $I4/mmm$   $\text{Rb}_2\text{Au}_2\text{Br}_6$  structure. What we can see from this figure is how the energy is lowered sufficiently to drive the appearance of the  $\Gamma_4^-$  polar distortion. The bottom distortion shows the 90, 95 and 100% strains again but this time supplemented with varying size of the Jahn-Teller distortion, again showing

the lowering of the energy, but this time to a much lesser effect. Descriptively this is showing us that the both strains contribute to the lowering of the energy considerably more than the Jahn-Teller distortion itself.

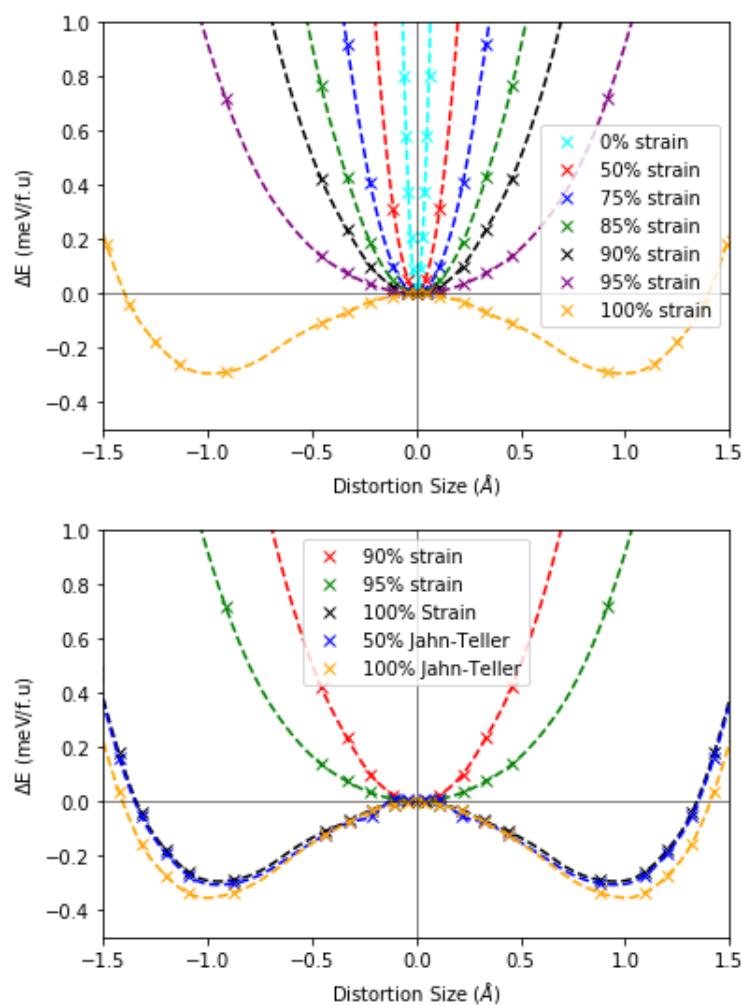


Figure 3.10: The change in the energy landscape as the the size of the polar distortion is varied. The bottom of the double well is characterised by the real distortion size of the  $\Gamma_4^-$  mode.

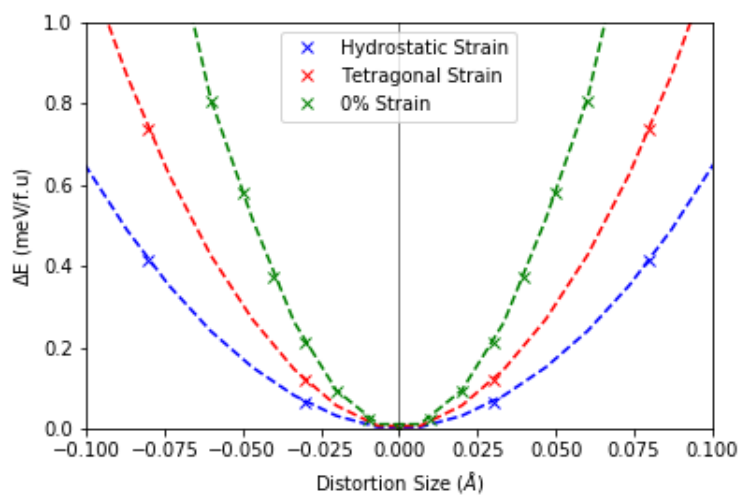


Figure 3.11: Contribution to the lowering of the energy through both the hydrostatic and tetragonal strain.

This was an interesting point as the Jahn-Teller distortion itself is what drives the appearance of the subsequent strains that appear in our structure. Referring back to our initial equation 3.3.2 where the lowering of the symmetry from the cubic to the tetragonal is driven by the appearance of the Jahn-Teller distortion. We therefore put forward the idea that the appearance of this polar distortion in the *proper* case as described earlier is driven by a pseudo-triggered mechanism. Through INVARIANTS analysis we show:

$$(F - F_0) \propto + \gamma_{13} Q_{\Gamma_{1+}} Q_{\Gamma_{4-}}^2 + \gamma_{23} Q_{\Gamma_{3+}} Q_{\Gamma_{4-}}^2 + \gamma_{14} Q_{\Gamma_{1+}} Q_{R_{3-}}^2 + \gamma_{23} Q_{\Gamma_{3+}} Q_{R_{3-}}^2 + \gamma_{34} Q_{\Gamma_{4-}} Q_{R_{3-}}^2 \quad (3.3.6)$$

The full INVARIANTS analysis can be found in Appendix A. We see a cooperative linear-quadratic term between both types of strain and the polar distortion in the  $I4mm$  phase and the subsequent linear-quadratic terms between the strains and the Jahn-Teller distortion. We can summarise this as:

$$R_3^- \rightarrow \Gamma_{1,3}^+ \rightarrow \Gamma_4^- \quad (3.3.7)$$

Triggered transitions usually occur via a cooperative bi-quadratic coupling term e.g, the rare-earth nickelates in which an ever increasing size of the octahedral rotations brings about a breathing distortion of the octahedral cages[129]. Our structure is not strictly speaking a triggered mechanism (hence the *pseudo*) because of this very reason. Our polar distortion in this mechanism does not arise due to cooperative coupling between the polar and Jahn-Teller distortions  $Q_{\Gamma_4^-} Q_{R_3^-}^2$  but more likely through  $Q_{\Gamma_1^+} Q_{\Gamma_4^-} Q_{R_3^-}^2$ . We could however think that the strain is subsumed within the  $R_3^-$  and thus effectively bi-quadratic. We mentioned briefly that both hydrostatic and tetragonal strains contribute towards the appearance of this polar distortion. It is the hydrostatic however that contributes more to the appearance (See Figure 3.11).

### Improper

As we have discussed previously in this section of the chapter, we wanted to explore both possibilities of the origin of the polar distortion within this structure. If we do take the improper method as the true method for the appearance of the polar distortion then through INVARIANTS analysis we see:

$$(F - F_0) \propto +Q_{\Gamma_4^-} Q_{R_2^-} Q_{R_5^+} + Q_{\Gamma_4^-} Q_{R_3^-} Q_{R_5^+} \quad (3.3.8)$$

The coupling terms in our INVARIANTS analysis here shows that there are several combinations of distortions that drive the appearance of the polar distortion. We see two trilinear coupling terms involving the polar distortion and the anti-polar distortion with both the breathing and Jahn-Teller distortions simultaneously. In terms of the coupling parameters it can make it difficult to ascertain which of the primary distortions, the breathing or the Jahn-Teller drives the appearance of the polar distortion. Even in this case however, we can make the assumption that the Jahn-Teller as the primary distortions can drive the appearance of the polar mode. It is however difficult to ascertain whether method is entirely correct due to the fact that the size of the anti-polar distortion is very small. With the results we discuss in the next chapter however, it would be possible to conclude that the anti-polar distortion is a secondary distortion (if it is real) and a result of symmetry through the fact the dielectric constant increases significantly near the phase transition of the  $I4/mmm$  to  $I4mm$ , but I thought it was necessary to explore both options.

### 3.4 Conclusions

In this chapter we have focused on the complexity of the gold double perovskite structures. We see some interesting changes as we change the size of the ions in our structure. From the cubic to  $I4/mmm$  phase we see the introduction of a breathing and Jahn-Teller distortion. Through both INVARIANTS analysis and DFT we determined that the primary order parameter is the Jahn-Teller distortion ( $R_3^-$ ). Not only does the  $R_3^-$  drive the phase transition from the cubic  $Pm\bar{3}m$  to the  $I4/mmm$  whilst the  $R_2^-$

breathing distortion comes through as a secondary order parameter. Through DFT we artificially reduce either distortion to zero and re-relax these structures we find that the  $R_2^-$  reappears when the  $R_3^-$  is non-zero and the  $R_3^-$  does not reappear when the  $R_2^-$  is non-zero. This in combination with the INVARIANTS analysis we see that the  $R_3^-$  phase drives the appearance of the  $R_2^-$  distortion through a cubic-linear coupling term. In the next chapter we will explore the effects of these distortions on the electronic properties of the material. As we reduce our tolerance factor we begin to see some of the complexity we spoke about initially set in. All structures which contain caesium fall into the  $I4/mmm$  phase with only the  $R_2^-$  and  $R_3^-$  present. This is also applied to the  $\text{Rb}_2\text{Au}_2\text{Cl}_6$ . However, once the tolerance factor falls lower than this then we start to see the transition to the  $C2/m$  phase. In this phase we see an additional  $R_4^-$  and  $R_5^-$  distortion which corresponds to an anti-polar and tilt distortion respectively. INVARIANTS analysis of this structure shows a quad-linear interaction which allows the appearance of both the anti-polar and tilt distortion together. Finally as reduce the tolerance factor down far enough we see the introduction of the  $P2_1/c$  phase for the  $\text{K}_2\text{Au}_2\text{I}_6$ . This includes an additional two more modes the  $X_5^+$  and a  $M_5^+$ , both of which correspond to another anti-polar and an additional tilt distortion. We see a large complexity of modes in the  $\text{K}_2\text{Au}_2\text{I}_6$  with the OPD not as complex in the  $R_4^-$  and  $R_5^-$ . We do however see a trilinear coupling term which allows the large amount of different modes to be included in our structure.

Overall we observe three phases in our nine distortions that we have analysed (see Figure 3.9) with increasingly more complexity. Finally in all of the structures which exhibit the  $C2/m$  and  $P2_1/c$  space group we observe an instability which is polar albeit which is not energetically favourable. Analysis of this polar distortion however does show some interesting properties. The polar phase couples with both the hydrostatic and tetragonal strains in our structure which drives its appearance. These strains however do not appear without the introduction of the Jahn-Teller and Breathing distortions - therefore leading us to the idea of pseudo-triggered mechanism. This leads us into the next chapter where we will observe the electronic properties of these materials and the effects each of these distortions have. Overall, we have explored

in rigorous detail the effects of tolerance factor on a group of structures which have shown excellent electronic properties in the literature and what we have really tried to do is show the origin of these of these electronic properties of which we will explore in greater detail in the next chapter.

# Tuning the Optoelectronic and Dielectric Properties of Gold Double Perovskites

*We can easily forgive a child who is afraid of the dark; the real tragedy of life is when  
men are afraid of the light.*

- Plato

## 4.1 Introduction

**I**N the previous chapter we have explored the diverse and rich nature of the perovskite materials in terms of their structural arrangement and the different distortions that can appear. It is well known through research that these structural and chemical properties can give rise to a large array of different properties that can be used in a variety of different fields. Many perovskites have applications in the general area of optics, including photovoltaics, lasers[146], x-ray detectors[147], scintillators[148] and uses in photoelectrolysis[149]. Here we will discuss different optoelectronic properties associated with the gold double perovskites and put forward some ideas on which would be the optimal structure for photovoltaic purposes. We will also discuss various other double perovskite materials which exhibit similar charge-ordering include oxides and halides. The optoelectronic properties of perovskite-like materials is wide and diverse. The work by Manser *et al.* show the plethora of properties that are present in MAPI[150]. In this chapter we will explore the effects of chemical substitution on the bandstructure, the dielectric properties and the absorption properties of double perovskites.

Bandstructures are the most straightforward way to describe the photovoltaic properties of materials due to the ever important properties of bandgaps, band shapes and thus charge carrier effective masses. Huge amounts of work has been focused on the popular metal-organic MAPI[151, 152] and the optoelectronic properties of this material due to its favourable band-gap and high power-conversion efficiencies. The optoelectronic properties of MAPI derive from the  $6s^2$  configuration of the Lead in MAPI[153], and this is something that we explore further on in this chapter when we look at the different materials which fall into the  $I4/mmm$  ground state with identical irreducible representations. The majority of structures that are observed when it comes to photovoltaic performance contain the B-site cation Lead, this is due to its overall reduction in the size of the band-gap which leads to better solar light absorption. Pritriana *et al.* discuss extensively the role of alkali metal-lead halides as

potential photovoltaic devices[154]. There is a lot of research currently moving away from the idea of lead based systems which is why we are looking to study the gold double perovskite structures. Chapter 5 will look back at the inorganic lead halide structures.

### Dielectric Response through Phonons

The dielectric response of perovskites has been examined quite extensively since the first idea of a perovskite photovoltaic surfaced. Photovoltaics as mentioned in the introduction need to be able to separate charges effectively in order for currents to flow. Unfortunately some materials are not polar (as discussed in the previous chapter) and therefore other methods for charge separation is being explored. High dielectric constants lead themselves to higher power conversion efficiencies (PCE's). It has been shown that higher dielectric constants within perovskite solar cells or solar cells in general reduces the influence between weakly bound electron-hole pairs[155]. Various perovskites have shown large dielectric constants, some work by Juarez-Perez *et al.* have shown that the dielectric constant for MAPI can reach up to 1000 with a power conversion efficiency of 17.9% [156]. High dielectric constants have also been shown to reduce excitonic effects through dielectric screening of the coulomb potential of the bound state electron-hole pair[157, 158].

The dielectric constant can also have effects on other perovskites such as  $ACu_3Ti_4O_{12}$  (where A = +1, +2, +3 cation) have shown enormous dielectric constants but does not seem to be underlying ferroelectric behaviour[159]. At the end of this chapter we will explore the dielectric behaviour of the gold double perovskites which is based on the underlying behaviour of a polar distortion which appears around the  $Rb_2Au_2X_6$  (X = Cl, Br, I) structures. The methodology which was employed is outlined below.

With no application of an electric field, there is a lattice contribution to the dielectric tensor, and as such can be written by:

$$\epsilon = \sum_m \frac{4\pi e^2}{M_0 \Omega} \frac{\tilde{Z}_{m\alpha}^* \tilde{Z}_{m\beta}^*}{\omega_m^2}, \quad (4.1.1)$$

which includes contributions from the zone-centre polar modes  $m$ .  $\Omega$  is the volume of the primitive unit cell,  $M_0$  is the reference mass taken a 1 amu (1 atomic mass unit) and  $\tilde{Z}_{m\alpha}^*$  is the mode effective charge,

$$\tilde{Z}_{m\alpha}^* = \sum_{i\gamma} \tilde{Z}_{\alpha\gamma}^*(i) \sqrt{\frac{M_0}{M_i}} \hat{e}_m(i\gamma), \quad (4.1.2)$$

where  $\hat{e}_m(i\gamma)$  is the dynamical matrix eigenvector for atom  $i$ . The born-effective charges can be calculated via:

$$\tilde{Z}_{\alpha\gamma}^*(i) = \frac{\Omega}{|e|} \frac{\partial P_\alpha}{\partial u_{i\gamma}}, \quad (4.1.3)$$

Where  $P_\alpha$  is the polarisation in a given direction and  $u_{i\gamma}$  is the small mode amplitude. In practice we extracted the born-effective charges from the VASP code and used the phonon distortions from our calculations.

## 4.2 Results

In this section we will discuss the effects of chemical substitution on the different optoelectronic properties of the material. We will primarily focus on the bandstructure, band-gap, effective masses and absorption of the structures. We will also look at the key distortions in a couple of structures to see how these distortions themselves affect the optoelectronic properties of the different materials. After a discussion of the bandstructures we will look at the dielectric effect that is present in the  $\text{Rb}_2\text{Au}_2\text{Br}_6$  structure and we look to exploit a larger dielectric constant out of the material through the use of hydrostatic pressure. As this chapter followed was part of the same results that was found in chapter 3 the computational methods are the same as those found in section 3.2.

### Cubic $\rightarrow$ I4/mmm

Whilst in the cubic phase of every material we see a metallic phase for our gold structures, we also do however know that the introduction of both the  $R_2^-$  and  $R_3^-$  distortions leads to an insulating phase so here we explore the effect on the introduction of

both of these distortions. Figure 4.1 shows the effect of the introduction of the Jahn-Teller ( $R_3^-$ ) phase in incremental size. When the Jahn-Teller distortion is small then we see a metallic phase and when the distortion size is just over 50% of the size which is found in the ground state structure then we see an a gap begin to open up. Overall, we do not see such an effect with the breathing distortion in our structures with the gap changing on a much smaller scale. As shown in Figure 4.2 we see a shift in the fundamental structure of the conduction band with the introduction of the breathing distortion to the structure. This change sees the introduction of a singular band form as our conduction band minimum (CBM), which others have seen to call an intermediate band (IB), but this is up for debate[106, 160]<sup>1</sup>. Introduction of both of the two types of distortion leads to the ground state structure of many of the higher tolerance factor structures the  $I4/mmm$  phase. This fits well with the idea that sup-

Distortion Size ( $R_2^-$ ) (%)	Band-Gap (eV)
25	0.61
50	0.83
75	1.07

Table 4.1: The increase in the gap for the breathing distortion is not insignificant but we do see an overall phase change with the Jahn-Teller.

pression of the breathing distortion suppresses the band-gap. This is seen in BaBiO<sub>3</sub> structure where the reduction in the size of the octahedral breathing distortion is sufficient to close the gap [161]. The opening of band-gaps is also seen in the CaFeO<sub>3</sub> and YNiO<sub>3</sub> structures[78] and more commonly in the RNiO<sub>3</sub>, where R represents the rare-earth nickelates[162]. The size of the gap can be tuned by tuning the composition of HoFe<sub>1-x</sub>Cr<sub>x</sub>O<sub>3</sub>[163]. It has been well documented that Jahn-Teller distortions influence the size of the band-gap with work being shown back in 1979 in the Jahn-Teller vacancy-ordered Silicon that a size of gap can be influenced through the size of the Jahn-Teller distortion[164]. More recently research has supported the idea that

<sup>1</sup>I will continue to use the term intermediate band in *italics* to describe the presence of the single/-double band that acts as our CBM for the  $I4/mmm$  structures. As shown further on this *intermediate band* becomes alot more prominent.

some Jahn-Teller distortions seem to lift energy levels and create the insulating/semi-conducting phases like the boron-rich structures which contain the  $B_{12}$  icosahedra structure[165, 166]. Mn-Ni co-doped  $BaTiO_3$  shows an influence in the gap with the Jahn-Teller active  $Mn^{3+}$  doped phase[167].

Overall we see the influence of the Jahn-Teller distortion in the overall appearance of the gap in our tetragonal  $I4/mmm$  phase, which provides us with the basis of the semiconducting material that we have been examining, as we shown further on in this chapter the addition of high pressure can lead to suppression of the band-gap due to reductions in both the Breathing and Jahn-Teller distortion, another way in which we can tune the size of the gap. Examination of the bandstructures as shown in Figure 4.1 we see the influence of the Au- $d$  and I- $p$  states on the band edges and the so called *intermediate band*, which leads to the formation of the gap. With the introduction of both the breathing and Jahn-Teller distortion we see an overall band-structure as shown in Figure 4.3.

This leads us to the idea that we could tune the gap of the material through the influence of the breathing and Jahn-Teller distortion and one of the ways in which this can be influenced is through chemical change. We will not discuss in this thesis but solid-solutions could be formulated to tune the breathing/Jahn-Teller distortions to a much finer margin and therefore the band-gap. Figure 4.4 show the density of states for both the  $d^8$  and  $d^{10}$  sites, separately. We can clearly see there is a strong contribution to the valence band-edges from the I- $p_{xy}$  and the I- $p_{yy}$ . The conduction band edges in the so called *intermediate band* have the same contribution from the I- $p$  states and overlaps with the Au- $d_{z^2}$  states on the  $d^8$  sites. For the  $d^{10}$  sites we see a small contribution from the Au- $d_{x^2-y^2}$  within the conduction band minimum. The overlap of these orbitals is what contributes to the size of the gap and is something we examine in the bandstructures further on. All density of state plots are supplied in Appendix B.

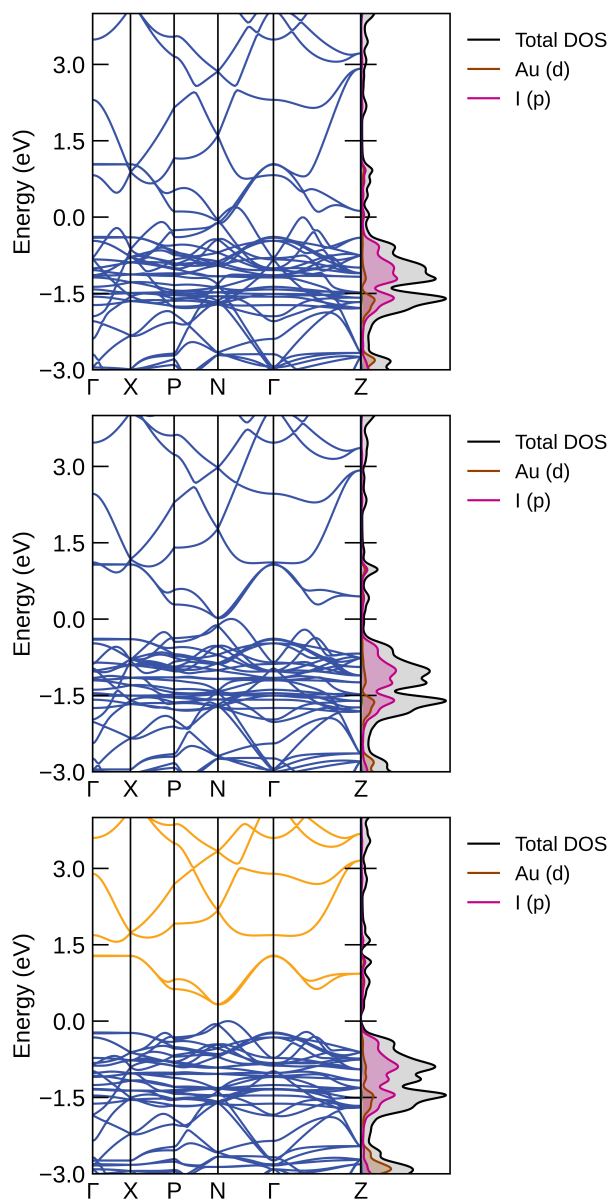


Figure 4.1: Incremental increase of the size of the Jahn-Teller ( $R_3^-$ ) (25%, 50%, 75% of the maximum value found in the ground state structure) distortion for the  $\text{Cs}_2\text{Au}_2\text{I}_6$  and the overall effect on the bandstructure.

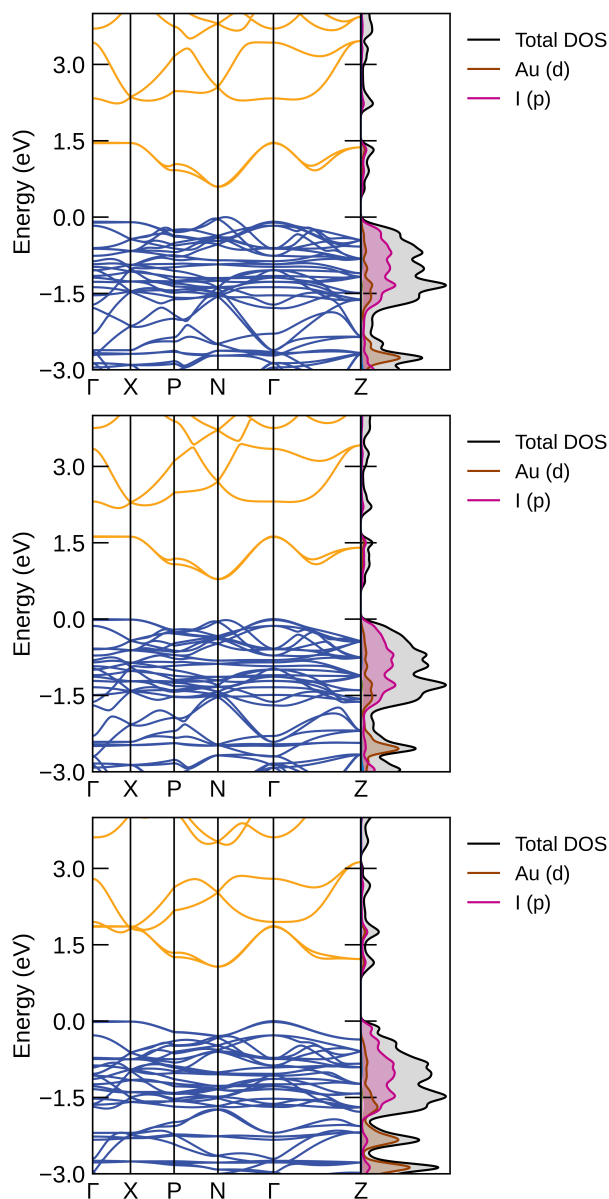


Figure 4.2: Increase in the size of the Breathing ( $R_2^-$ ) (25%, 50%, 75% of the maximum value found in the ground state structure) distortion for the Cs<sub>2</sub>Au<sub>2</sub>I<sub>6</sub> with the overall effects on the bandstructure. The bandstructures shown here show a small increase in the size of the gap as shown by Table 4.1.

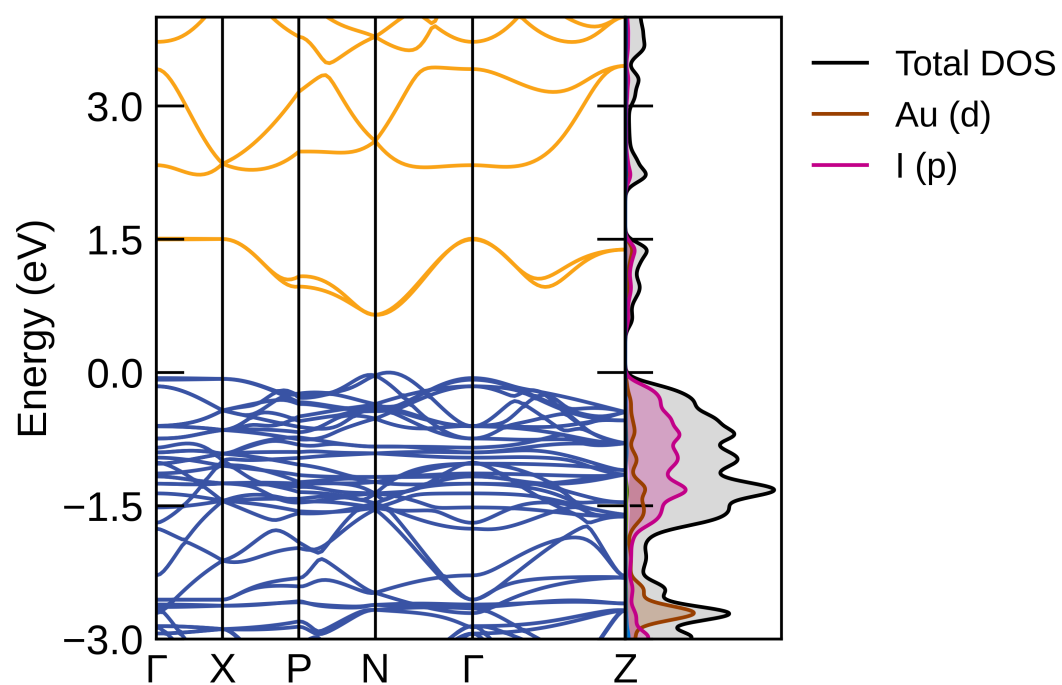


Figure 4.3: Band-Gap for the groundstate  $\text{Cs}_2\text{Au}_2\text{I}_6$  structure. As described by Deb-bichi *et al.*[106], the formation of an *intermediate band* (IB) forms between both the conduction band (CB) and the valence band (VB) at approximately 0.7-1.5eV.

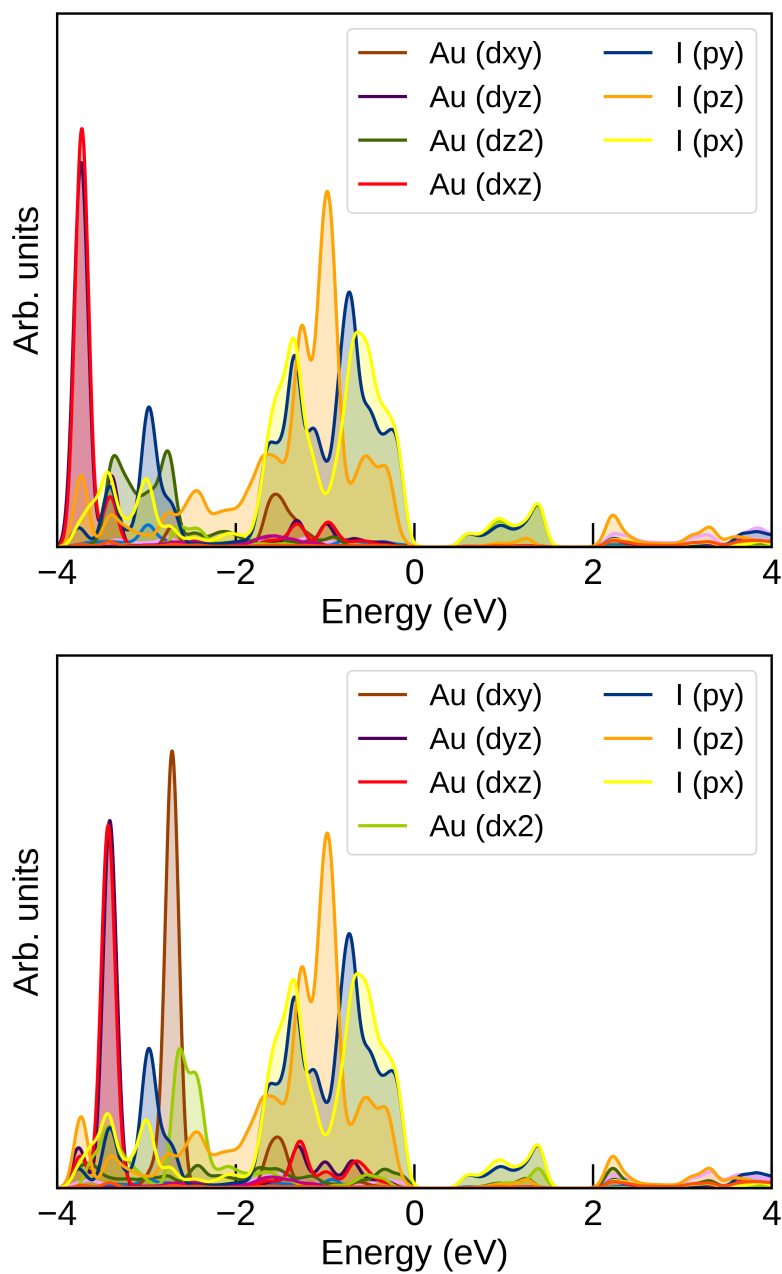


Figure 4.4: Density of states for the  $\text{Cs}_2\text{Au}_2\text{I}_6$   $I4/mmm$  structure. (a) Density of States looking exclusively at the Au- $d^8$  alongside the I- $p$  states. (b) Density of states looking exclusively at the Au- $d^{10}$  sites alongside the I- $p$  states.

When we look at the band-gap for the  $\text{Cs}_2\text{Au}_2\text{I}_6$  in our calculations we find a value of approximately 0.68eV (Figure 4.3. Calculations from Debbichi *et al.*[106] show the band-gap to be around 1.3eV. This massive underestimation is due to the effects the exchange-correlation functional employed in our calculations (PBESol[135]) which severely underestimates the electronic effects of the band-gap. In the work completed by Debbichi *et al.* they employed the hybrid functional **HSE** which is computationally a lot more expensive but can accurately account for the coulomb potential exchange portion of the energy, which fits more in line with what is seen experimentally (see 2.2). We can however makes estimations based on our band-gap calculated and the band-gap of that found from Debbichi *et al.* and that of experimental work on  $\text{Cs}_2\text{Au}_2\text{I}_6$  from Liu *et al.* who further supports a gap of 1.31eV[168]. A gap which is similar to that required through the Shockley-Quiesser limit of a single junction photovoltaic. As we look further at different chemistries, for structures of  $\text{Cs}_2\text{Au}_2(\text{Br},\text{Cl})_6$  we see an overall increase in the size of the gap. This is something in which we predicted even before calculation due to the increase in the size of both the Breathing and Jahn-Teller distortion (see table 3.4). Table 4.2 shows the overall increase in the

Chemistry	Tolerance Factor	Irreps & Amplitude (Å)	$E_g$ (eV)
$\text{Cs}_2\text{Au}_2\text{Cl}_6$	0.92	$\begin{pmatrix} R_2^- \\ R_3^- \end{pmatrix} \rightarrow \begin{pmatrix} 0.10 \\ 0.79 \end{pmatrix}$	0.95
$\text{Cs}_2\text{Au}_2\text{Br}_6$	0.91	$\begin{pmatrix} R_2^- \\ R_3^- \end{pmatrix} \rightarrow \begin{pmatrix} 0.06 \\ 0.69 \end{pmatrix}$	0.72
$\text{Cs}_2\text{Au}_2\text{I}_6$	0.90	$\begin{pmatrix} R_2^- \\ R_3^- \end{pmatrix} \rightarrow \begin{pmatrix} 0.03 \\ 0.61 \end{pmatrix}$	0.65

Table 4.2: Expansion of Table 3.4 with the inclusion of the optical band gap. The gap is influenced based on the size of the Breathing and Jahn-Teller distortions.

gap with the size of the Breathing and Jahn-Teller distortions increasing alongside it. As we tolerance factor becomes larger, the Jahn-Teller and Breathing distortions get larger and thus the gap get larger. This overall increase is again supported by experimental work by Liu *et al.*[168] who show that the optical gap for  $\text{Cs}_2\text{Au}_2\text{Cl}_6$  is 2.01eV, something which is not out of reach for photovoltaics but not the most efficient for

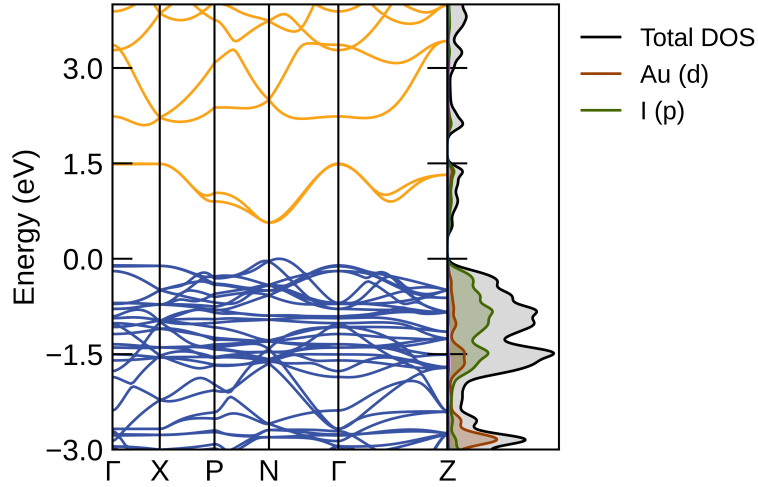


Figure 4.5: Bandstructure for the  $\text{Rb}_2\text{Au}_2\text{I}_6$   $I4/mmm$  phase. We see a similar shape to the caesium counterpart but with the gap bigger due to the increase in both the breathing and Jahn-Teller distortions.

solar light absorption.

### $I4/mmm \rightarrow C2/m$

As mentioned in Chapter 3 we see an overall structural phase transition from the  $I4/mmm$  phase to the lower symmetry tilted  $C2/m$  phase. In between we see structures present in the phonon dispersions which could possibly lead us to exciting properties which will be discussed later. For the  $\text{Rb}_2\text{Au}_2\text{Cl}_6$  we make the prediction that the structure is still in its  $I4/mmm$  phase. The  $\text{Rb}_2\text{Au}_2\text{Cl}_6$  phase has a larger band-gap than its caesium counterpart. The more important analysis was made on the tilted  $\text{Rb}_2\text{Au}_2\text{I}_6$  phase, in which we had two additional distortions present, the  $R_4^-$  anti-polar distortion and the  $R_5^-$  tilt distortion. We looked at both the effects of the incrementally increasing the size of the distortions as we did with the breathing and Jahn-Teller and also looking at both the  $I4/mmm$  high symmetry phase and the low symmetry ground state  $C2/m$  structure. Both Figures 4.5 and 4.6 show the bandstructures of the  $\text{Rb}_2\text{Au}_2\text{I}_6$  high and low symmetry structures. Overall we see quite

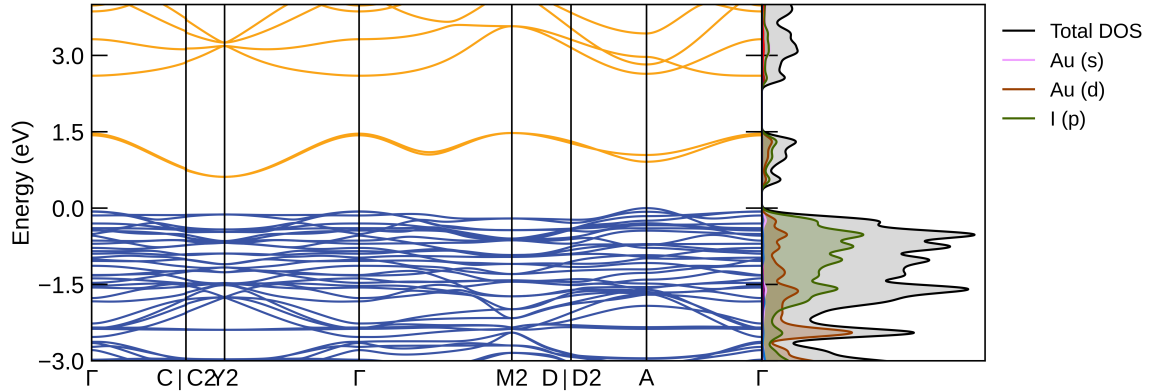


Figure 4.6: Bandstructure for the  $\text{Rb}_2\text{Au}_2\text{I}_6$   $C2/m$  phase. We see more flattening of the bands in the tilted low symmetry phase which opens up the gap.

significantly different bandstructures with the introduction of the anti-polar and tilt distortions. Firstly we see an indirect band-gap (similar to the  $I4/mmm$ , although between the A-point of the VBM and the  $C2$ -point of the CBM with an overall gap of 0.74eV. In our ground state  $C2/m$  phase we see a larger gap with the tilt distortion contributing to the widening of the gap (see Table 4.3). The biggest contribution to gap widening is through the appearance of the  $R_5^-$  with the  $R_4^-$  distortion contributing by reducing the size of a gap by a small margin. This is something we would expect with the band edges primarily shifting due to the Au- $d$  and the I- $p$  states, whereas the  $R_4^-$  appears through the movement of the A-site rubidium cations, which contribute a very small amount. We do also see through measurements of the  $I4/mmm$  phase from Cs Rb that the gap can close by a small amount.

We therefore would expect the gap to get smaller with the introduction of the potassium on the A-site again in the  $I4/mmm$  phase. This helps create another angle for tuning of our optical band-gap to help support solar light absorption. Prasanna *et al.* efficiently tuned the band-gap of lead and tin perovskite structures through contraction and expansion of the lattice parameters and octahedral tilting[169]. Similarly, Coduri *et al.* suggested that a shift in the band-gap could be supported using pressure. This acts a way to suppress certain distortions in the structure and thus

% Change of Ground State Distortion	Band-Gap ( $R_4^-$ ) (eV)	Band-Gap $R_5^-$ (eV)
25	0.69	0.395
50	0.68	0.513
75	0.63	0.610

Table 4.3: Band-gap changes based on the systematic change in the size of the anti polar ( $R_4^-$ ) distortion and the tilt ( $R_5^-$ ) distortion.

close/tune the gap[170]. Amat *et al.* show that changes in the cation from Methylammonium to Formadinium leads to superior band-gap values for solar light absorption due to suppression of the tilting distortions present in the structure[171]. The tilting that we see through this transition from the I4/mmm to the C2/m phase leads to considerably different charge carrier properties. Work on the  $Rb_2SnI_6$  and  $Cs_2SnI_6$  structures sees increases in the effective masses of the charge carriers when static octahedral tilting is introduced into the structure and the overall increase in electron effective mass for the  $Rb_2SnI_6$  seems to lead to lower carrier mobility within in the structures[172]. We can make comparisons between the effective masses of the tilted

Charge Carrier	Eff. Mass
$m_e^*$	0.183
$m_h^*$	-0.244

Table 4.4: Effective masses of the charge carriers in the  $Rb_2Au_2I_6$  I4/mmm phase. from the N  $\rightarrow$   $\Gamma$  point.

Charge Carrier	Eff. Mass
$m_e^*$	1.043
$m_h^*$	-0.240

Table 4.5: Effective masses of the charge carriers in the C2/m phase with the effective masses of the electron holes between the D2-A point and the effective masses of electron at the Y2 point.

and untilted phases to see the clear effects that the tilting can have on the mobility of the charge carriers through the material, something which is important for the func-

tion of a photovoltaic. This opening of the gap between the high and low-symmetry structures for gold double perovskites arises due to the overall decrease in the size of the Au-I-Au orbitals, this opens up the gap and reduces overall bandwidth as shown in Figure 4.6. Work has been conducted on how the size of effective masses can affect the mobility of charge carriers as far back as 1958, where there is a clear trend that an increase in the effective mass of the charge carriers leads to slower mobility through the material[173]. It is also important to note that effective masses of charge carriers can be manipulated through chemical substitution (which as a result can lead to steric change). For example the change of anion from Cl  $\rightarrow$  Br  $\rightarrow$  I can lead to increase of effective mass in charge carriers for  $\text{CH}_3\text{NH}_3\text{PbX}_3$  (X = Cl, Br, I)[174].

#### **I4/mmm $\rightarrow$ P2<sub>1</sub>/c**

The final part of our phase diagram is analysis of the bandstructures that appear in the lowest symmetry phase the P2<sub>1</sub>/c. Analysis was primarily undertaken on the  $\text{K}_2\text{Au}_2\text{I}_6$  due to the experimental work supporting its synthesis[175]. In our low symmetry structure we expected to see a very large band-gap appear due to two tilt distortions being active in comparison to the other structures we have observed. Figure 4.7 and Figure 4.8 shows the difference in the bandgaps between the high symmetry I4/mmm phase and the low symmetry P2<sub>1</sub>/c. In our high symmetry phase we see a indirect band-gap of 0.58eV between the N- $\Gamma$  point, again we see a reduction in the band-gap as we change our A-site cation to something which is smaller where an overall reduction in the size of the A-site cation leads to a reduction in the overall volume of the unit cell. This subsequently increases the amount of overlap between the Au-I-Au orbitals. In our P2<sub>1</sub>/c phase the bandgap is inflated up to an indirect value of 1.26eV at the  $\Gamma$ -point for the VBM and between the C2-Y2 point for the CBM. Table 4.7 shows the effective masses of the P2<sub>1</sub>/c phase with the increased effective mass of one of the charge carriers. What we have here is a lots of interplay between the various distortions and the optical properties of the material. Firstly if we look at how the optical absorption changes over the anions so looking at  $\text{Cs}_2\text{Au}_2\text{X}_6$  (X = I, Br, Cl). Figure

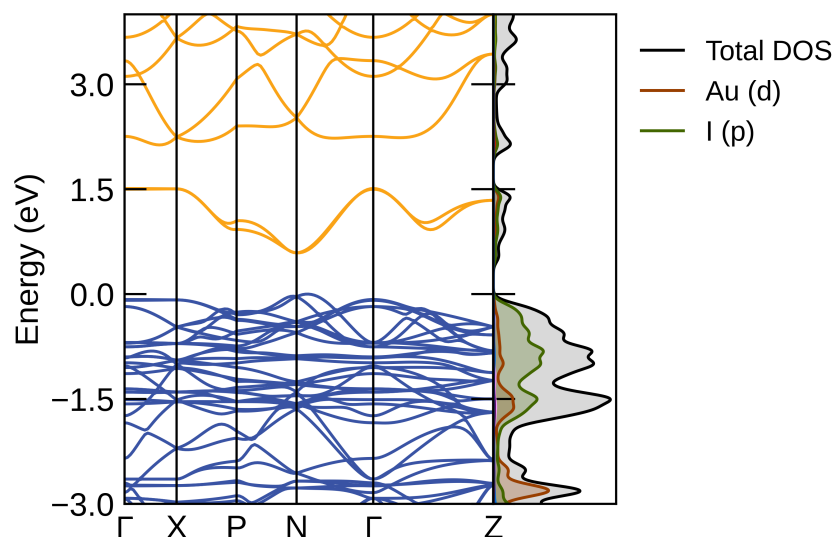


Figure 4.7: Bandstructure for the  $I4/mmmm$   $K_2Au_2I_6$  phase. The bandstructure looks similar to all of the other  $I4/mmm$  phases, with small changes in the gap due to chemical substitution.

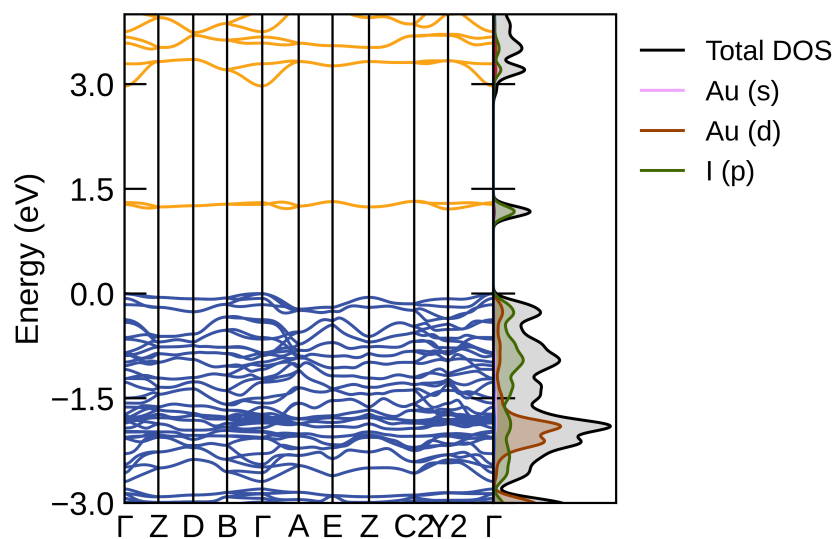


Figure 4.8: Bandstructure for the low symmetry  $P2_1/c$   $K_2Au_2I_6$  phase. All of the bands appear more flat due to the two tilts that appear in the low symmetry structure, subsequently reducing Au-I-Au orbital overlap and reducing the bandwidth. Indirect band-gap of 1.22eV between the C2-Y2 point and the  $\Gamma$  point.

Charge Carrier	Eff. Mass
$m_e^*$	0.188
$m_h^*$	-0.235

Table 4.6: Effective masses of the charge carriers from the high-symmetry  $I4/mmm$  phase of the  $K_2Au_2I_6$  with both the electron hole and electron effective masses appearing between  $N \rightarrow \Gamma$

Charge Carrier	Eff. Mass
$m_e^*$	1.667
$m_h^*$	-2.268

Table 4.7: Effective masses of the charge carriers for the ground state low-symmetry structure of the  $P2_1/c$  between the  $C2-Y2$  for the holes and the  $\Gamma$  for the electrons.

4.9 shows how the absorption of the structures changes with incident energy of light in eV. All structures seem to absorb light at the same level before the appearance of an absorption *gap*, this occurs with all structures where the level or absorption becomes significantly lower. This is similar to that of MAPI where an absorption *gap* appears between the first two peaks[176]. Absorption across these materials follows a similar trend. We also looked at the absorption across the three different ground states that we were able to determine and as such we looked at the  $X_2Au_2I_6$  ( $X = Cs, Rb, K$ ). Figure 4.10 shows this absorption based on the energy of the incident light. We can see clearly that there is a shift in the initial peak of the due to the overall increase in the size of the band-gap.

Much like the changes through the caesium compounds we see smaller absorption at lower energy levels and much higher absorption at higher energy levels, this is similarly due to and matches that of the AM1.5G solar irradiance spectrum. Due to its lower bandgap specifically the caesium and rubidium compounds absorb light more readily than the well known organic photovoltaic perovskite MAPI[176, 106].

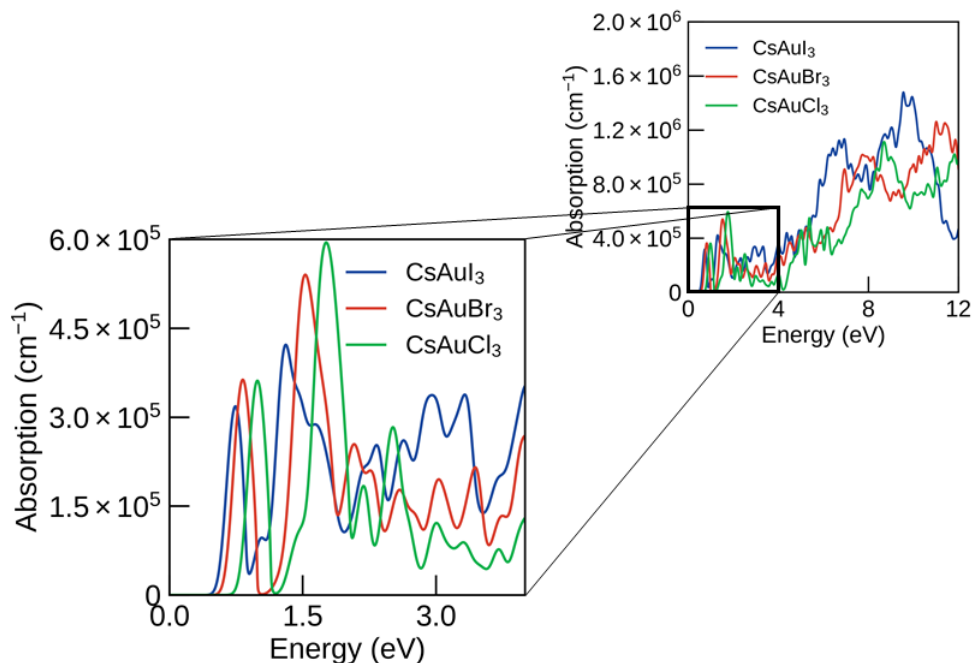


Figure 4.9: Absorption of all three caesium compounds across a range of 12eV (100nm) and a focused area which looks at the areas from around the bandgap onwards. All of which are based on the I4/mmm bandstructure displayed in Figure 4.3

### Effects of Pressure on Distortions

One of the calculations that we put forward was the effects of hydrostatic pressure on the electronic properties of the material. Application of hydrostatic pressure is both used experimentally and theoretically to determine any changes in the optoelectronic properties of the material. In our first step of this study we looked at the effects of the hydrostatic pressure on the two main distortions which allow the electronic properties to appear; the  $R_2^-$  and  $R_3^-$ . What we observed was an overall reduction in the size of both of the distortions and they both follow a similar trend.

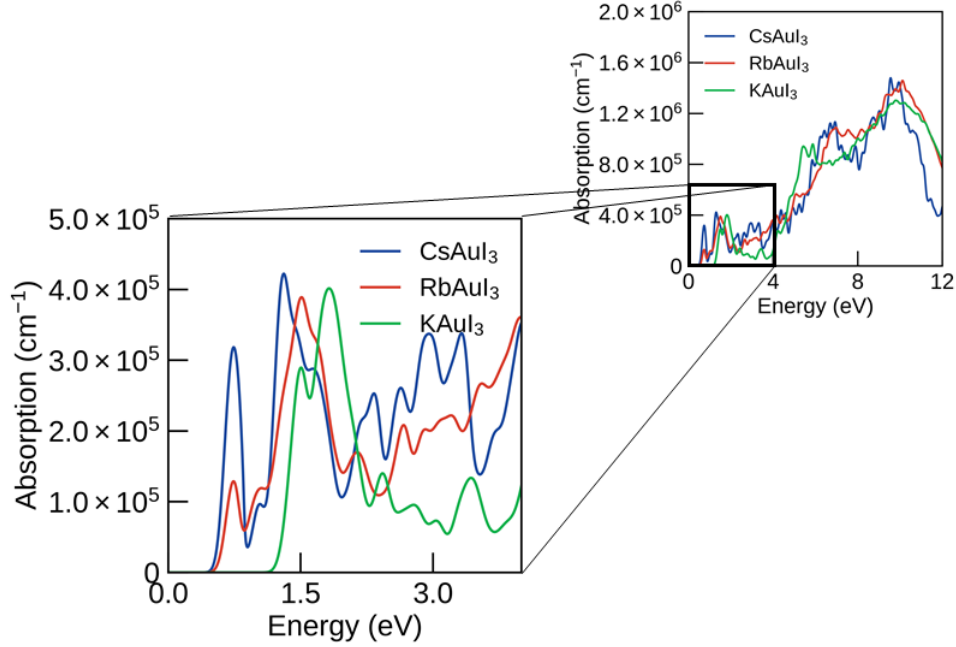


Figure 4.10: Absorption of the three ground state Iodine structures, Cs (I4/mmm), Rb(C2/m) and the K(P2<sub>1</sub>/c).

Analysis of the band-structures show that we see an insulating to metal transition at around the 3.5-4.5GPa region, and it would appear that this is driven by the reduction in the Jahn-Teller distortion. We also similar properties experimentally with these structures. For example, experimentally we a change from the (Au<sup>I</sup>, Au<sup>III</sup>) to a Au<sup>II</sup> electronic state in which there is not a insulator-metal transition at approximately 55kbar (5.5GPa)[177, 178]. Other work suggests that there is a insulator-metal transition at approximately 4.5GPa, something which is supported by Kojima *et al.*[179]. Research has also been conducted on similar transition metal perovskites that are Jahn-Teller active where hydrostatic pressure reduces the Jahn-Teller distortions[180] Because of the reduction in both the breathing and Jahn-Teller distortions we see some changes in the distortions of other materials, the material that we will be examining is the Rb<sub>2</sub>Au<sub>2</sub>I<sub>6</sub> C2/m phase. Figure 4.12 shows the effects of hydrostatic pres-

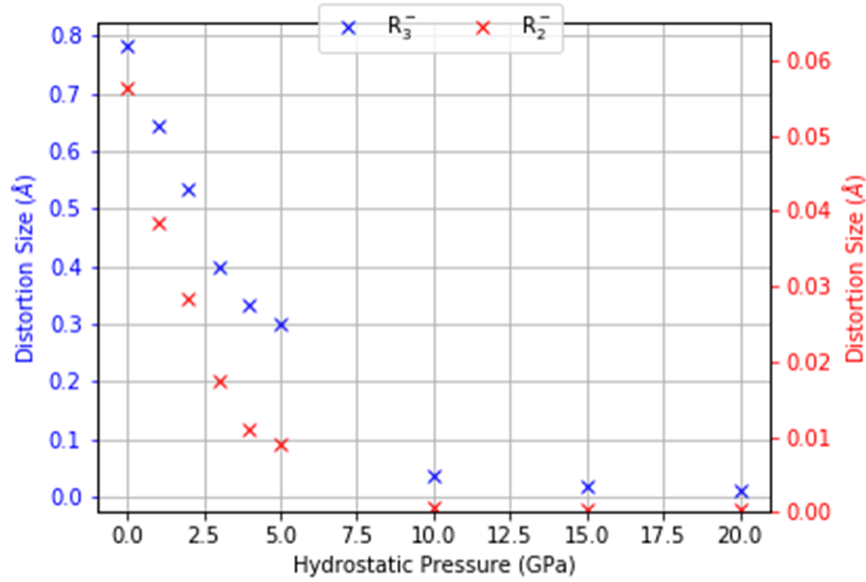


Figure 4.11: The effect of hydrostatic pressure on the size of the  $R_2^-$  breathing distortion and the  $R_3^-$  Jahn-Teller distortion showing a steep reduction that occurs between 0 to 5GPa and the following measurements shown an almost 0 amplitude for the size of the breathing distortion from 10GPa onwards.

sure on the three distortions of interest. Pressure usually induces tilting in perovskites and has been shown to induce such a phase transition in  $\text{LaAlO}_3$ [181]. The previously mentioned transition metal perovskite structures similarly produces tilt distortions when the pressure is sufficiently high enough[180]. The reason as to which ours suppresses the appearance of the tilt distortion and the rest of the distortions is due to the fact that the main reason these distortions appear is because of the two main tetragonal distortions.

As we know that the initial tetragonal structure brings in both the Jahn-Teller and Breathing distortions and subsequently at lower tolerance factors we see a secondary phase transition to the  $C2/m$  phase (see equation A.2.2). Therefore suppression of these two distortions leads to the tilts and other distortions disappearing. Looking at Figure 4.12 we can see that generally all distortions move relative to each other and therefore there will be a pressure in which the polar distortion is isolated. Unfortu-

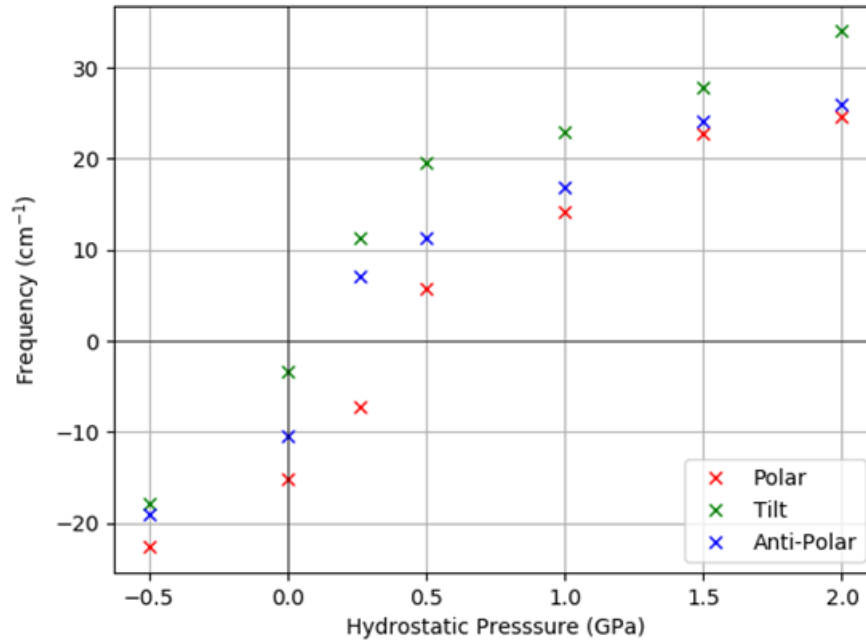


Figure 4.12: The effects of hydrostatic pressure on three distortions of interest in the  $\text{Rb}_2\text{Au}_2\text{I}_6$ . The Tilt distortion, polar distortion and anti-polar distortion.

nately this is likely to be a very small pressure window, with the precise transition point likely to depend on the DFT details, however we can work with the idea that the polar distortion could be just stable, this would lead to a larger dielectric response when the pressure is just above the transition to the polar phase.

### Dielectric Response

As mentioned it is possible to suppress the polar distortion so it is just stable and it is shown that there can be an enhanced dielectric response in our perovskite material. The analysis of the dielectric response was primarily carried out within the  $\text{Rb}_2\text{Au}_2\text{Cl}_6$ , the reasoning behind this is due to lower frequencies found in the  $I4/mmm$  phase of the Cl compound. The application of a positive/negative hydrostatic pressure systematically changes the  $\Gamma_1^+$  and  $\Gamma_3^+$  strain (See equation 3.3.7 and can lead to

an enhanced dielectric effect. We looked initially at understanding the ionic dielectric response through the phonon distortions. Equation 4.1.1 shows how we calculated the dielectric response. In principle VASP calculates the 3 x 3 dimensional matrix of the dielectric tensor but we were interested in looking at the effects of the phonons individually for the dielectric. We initially examined the value for the dielectric in the  $xx$ ,  $yy$  and  $zz$  directions for the  $\text{Cs}_2\text{Au}_2\text{X}_6$  ( $X = \text{Cl, Br, I}$ ) and the  $\text{Rb}_2\text{Au}_2\text{Cl}_6$ . As shown

Structure	$\epsilon_{xx}$	$\epsilon_{yy}$	$\epsilon_{zz}$
$\text{Cs}_2\text{Au}_2\text{Cl}_6$	8.78	8.78	5.16
$\text{Cs}_2\text{Au}_2\text{Br}_6$	12.1	12.1	5.89
$\text{Cs}_2\text{Au}_2\text{I}_6$	16.2	16.2	6.56
$\text{Rb}_2\text{Au}_2\text{Cl}_6$	21.1	21.1	14.75

Table 4.8: Dielectric response in the  $xx$ ,  $yy$ , and  $zz$  directions for the Cs compounds and the highest tolerance factor Rb in the  $I4/mmm$  space group. We see a slow increase as the phonon distortion reduces in frequency (See the dielectric phonon tables in Appendix B).

from Table 4.8 we can see that the dielectric constant in all three directions increases as the tolerance factor decreases. When we observe the phonon distortions all four structures we see the  $xx$  and  $yy$  direction dominates the increase in the dielectric for the cesium structures and to some extent it dominates the rubidium compound also. However as we get closer to the  $\text{Rb}_2\text{Au}_2\text{Br}_6$  compound the  $zz$  component of the dielectric starts to increase considerably and this is the one which becomes active when we observe the various instabilities in the Br and I structures of the Rb. So there does seem to be a bigger influence through a reduction in the tolerance factor/ion size which leads to an instability in the  $I4mm$  phase (see section 3.3).

It is also important to note that a change of chemistry through the A-site cation or X-site anion can also lead to changes in the dielectric constant individually due to changes in the born-effective charges. Through adjustments to the size of the strain we can attempt to tune the size of the ionic dielectric contribution quite significantly. We know from equation 4.1.1 that the size of the dielectric constant changes based on

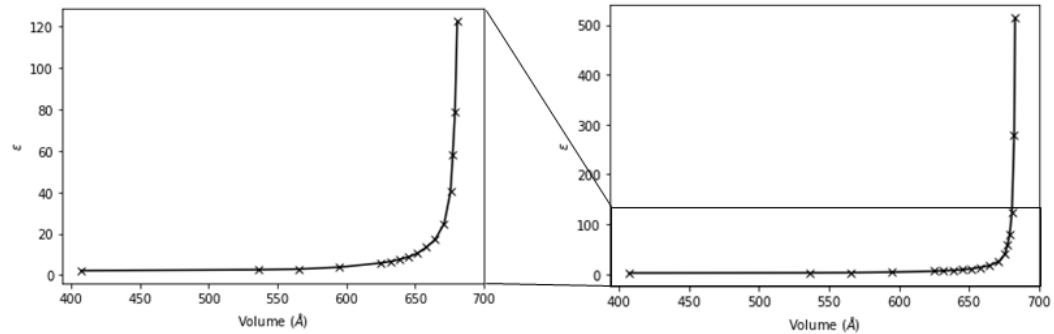


Figure 4.13: Size of the ionic contribution to the dielectric constant in the  $zz$  direction with respect to the volume of the unit cell in the  $\text{Rb}_2\text{Au}_2\text{Br}_6$ .

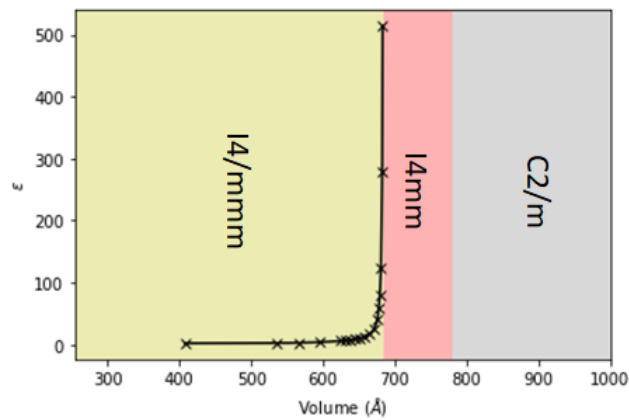


Figure 4.14: Graphic displaying the dielectric constant with respect to a phase diagram. The volumes were taken from the ground state volumes for the  $\text{Rb}_2\text{Au}_2\text{Br}_6$  structure.

the inverse of  $\omega^2$  so a reduction in the size of the distortions in  $\text{Rb}_2\text{Au}_2\text{Br}_6$  structure can lead to an enhanced dielectric effect. We subsequently decreased the volume of the unit cell systematically and measured how the dielectric constant changed. As shown in Figure 4.13 the dielectric becomes very large when the volume and thus the  $R_2^-$  and  $R_3^-$  is just right for the ground state to stay tetragonal  $I4/mmm$ . As the strain is increased the dielectric constant begins to decrease significantly due to the suppression of the key distortions which allow for the activation of the polar mode. In order

for us to be able to produce a dielectric of this magnitude, a sensitive and refined solid-solution between the chlorine and bromine may be necessary for the dielectric to become large enough for photoferroic use.

### 4.3 Conclusions and Final Remarks

Overall across these previous two chapters we have explored and examined in detail the physical and electronic properties of the gold double perovskites. We initially discussed the origin of the gap in our double perovskite structures. We systematically reduced the two primary distortions in the gold double perovskite  $I4/mmm$  phase and found that although both open up the gap between the VBM and CBM, we see a very large change with the  $R_3^-$  Jahn-Teller distortion. Not only did we discover that the primary distortion in these structures is the Jahn-Teller but it is also the one which influences the size of the gap. We therefore predicted that a metal-insulator transition appears at approximately 50% of the maximum value for the Jahn-Teller distortion in the ground state. Beyond this we explored how the gap changed with chemistry and saw an reduction in the bandgap as we moved from  $\text{Cl} \rightarrow \text{Br} \rightarrow \text{I}$  with the Chlorine having a band-gap 0.95eV. We discussed the underestimation with respect to the experimental work that has been completed on these materials and this is something we will discuss more at the end of Chapter 5.

We looked at the effects of the tilt and anti-polar distortions with the anti-polar reducing the gap by a very small amount the tilt with combination of chemical change lead to a much larger gap and we showed the effect with the flattening on the band edges. We also discussed the low symmetry  $\text{K}_2\text{Au}_2\text{I}_6$  which has two tilts and bands which are extremely flat which lead us into a small discussion of the effective masses of the charge carriers. These effective masses increased a small amount and dependent on the K-space path that was taken it seemed to be the electrons and the holes which were swapping in which was getting bigger. We discussed the effects of absorption and looked at the absorption coefficients for each of the main structures discussed and found a variety of differences and similarities between them. It was

when there was phase changes that we saw the physical differences in the absorption spectra change. Finally we explored the effects of hydrostatic pressure on the electronic properties of these materials. Usually we see through the increase in hydrostatic strain on perovskite like materials tilts become more pronounced and the idea of polar distortions can come apparent, however with the gold double perovskites we do not see this. This is due to the primary link between the Breathing, Jahn-Teller and all of the distortions that appear after them. Due to the link as discussed in Chapter 3 between the strain and the Jahn-Teller a reduction in the strain leads to a reduction in the Jahn-Teller. This therefore supported our idea that structures that had phonon instabilities in them were removed as those frequencies became positive. We discussed the possibility of having a ground state polar distortion through hydrostatic pressure but found the pressure to be very small.

We then looked at applying this process to a dielectric material and we looked at the effects of the born-effective charges and the phonons on the dielectric constant and the influence of changing the chemistry on the phonons and therefore the influence of the dielectric constant. We saw the dielectric constant increase as we moved towards the structure which had a polar instability and we finally looked at tuning the size of this distortion through hydrostatic pressure once more, through this we found the dielectric constant can be maximised up to a singular point at which the material would become polar. Overall exploring these gold perovskite structures has lead us to some fascinating discoveries in terms of the appearance in the polar distortions, the rich complexity of distortions in all of the different chemistries and their associated electronic properties. I will discuss future work in the conclusion at the end.



# Engineering Ferroelectricity in Metal Halide Perovskites

*All the mathematical sciences are founded on the relations between physical laws and  
laws of numbers.*

- James Clerk Maxwell

Over the past 10-15 years there has been a tremendous amount of work put into the field of perovskite photovoltaics. Thousands of papers and several books later we are not at a point where efficiencies are now comparable or supersede the most popular light absorber, silicon. Through *ab initio* methodologies we have been able to show the potential that perovskite materials have and unravelled the mysteries surrounding the origins of such properties that were listed previously. In this chapter we will be taking an analytical approach to determine whether layered perovskite-like materials are suitable as photoferroics.

## 5.1 Introduction

One of the key aspects to a photovoltaic is the ability to separate charge. In a conventional solar cell n-type and p-type silicon is used to create an electric field which drives the charge separation. This is however, not cost effective nor efficient. Therefore there has been a research put into finding ferroelectric photovoltaics (FE-PV), with enhanced photogenerated charge separation, with the possibility of above band-gap photovoltages. Unlike traditional semiconductor photovoltaic devices that require a p-n junction to allow for charge separation, ferroelectric materials do not. Ferroelectric materials have spontaneous polarisation which can be reversed using an electric field, a built in depolarising field[182]. There is a clear indication that charge separation can occur through the presence of microscopic domain walls in ferroelectric materials[183, 184]. The development of perovskite FE-PV has moved through several channels over the years including single-crystal  $\text{LiNbO}_3$ [185], thin film  $\text{BiFeO}_3$ [186] which have shown generally low band-gaps of 2.17eV for oxide perovskites and even the multi-junction ferroelectric perovskites which have been shown to have power conversion efficiencies of about 21%[187]. One of the growing issues around the use of ferroelectric photovoltaics is the usually large band-gaps which are associated with perovskite oxides, examples including  $\text{BiMnO}_3$ [188],  $\text{CdTiO}_3$ [189],  $\text{AgNbO}_3$ [190] and  $\text{PbTiO}_3$ [191]. There has also been progressive development of organic ferroelectric perovskites and a lot of debate over whether the ferroelectric prop-

erties of Methylammonium Lead Iodide (MAPI) lead to an improvement in photovoltaic performance[192].

As we have previously shown in the results chapters 3 and 4, distortions can play a large effect on the development of ferroelectricity and band-gap, for example Nechache *et al.* conducted research on the double perovskite structure  $\text{Bi}_2\text{FeCrO}_6$  and were able to tune the ferroelectric and photovoltaic properties via the Jahn-Teller distortions driven by the  $\text{BB}'$  ions, through the physical deposition of the Fe and Cr ions. This ordering of the Fe-Cr lead to a substantial lowering of the gap to 1.4eV and the creation of ferroelectric domains[193]. What we have shown here is the breadth of different ferroelectric materials that can enhance the separation of charge carriers in the material. Unfortunately generally most ferroelectric materials have large band-gaps and are not suitable for photovoltaic applications. Therefore, we propose taking a photovoltaic material and engineering ferroelectricity in it. The basis for this research is the Ruddlesden-Popper structure. This has been a target for photovoltaic research due to large power conversion efficiencies, large open circuit photovoltages and improved stability[194]. Examples include the two-dimensional Ruddlesden-Popper layered metal halide perovskites by Huang *et al.* in which power conversion efficiencies of 16.5% were generated[194]. Huang *et al.* also were able to show the development of even further power conversion efficiencies of 17.8% in  $(n=5)$   $(\text{MTEA})_2(\text{MA})_4\text{Pb}_5\text{I}_{16}$  with improved moisture and thermal stability (1,512 hours under 70% humidity and 375 hours at 85°C)[195]. This is a large improvement on the stability of a material which is notorious for poor light, moisture and thermal stability[196], which is quite humorous for a material which would be bolted to a roof. There seems to be a large amount of work being put into the organic Ruddlesden-Popper phases[197, 198, 199] which exhibit more suitable optoelectronic properties for photovoltaic purposes and are more lightweight and can be used as smaller thin films with a few nanometres thick, they are however more prone to environmental problems.

## Ferroelectric Solar Cells

Recapping from the introduction, in a ferroelectric, the spontaneous symmetry breaking leads to a polarised material. Suggestions that it could improve photovoltages within photovoltaic materials has made these systems extremely interesting. There has been a lot of work that has gone into the understanding of ferroelectric materials in photovoltaics and the modern theory of ferroelectrics shows that the photocurrents that are produced exclusively from the appearance of a lack of inversion symmetry and not an electric field. As described by Young and Rappe, the *shift current* can be calculated using the perturbation theory method with the second order coupling with monochromatic light[200, 201]:

$$\begin{aligned}
 J_q &= \sigma_{rsq} E_r E_s \\
 \sigma_{rsq}(\omega) &= \pi e \left( \frac{e}{m\hbar\omega} \right)^2 \sum_{n', n''} \int d\mathbf{k} (f[n''\mathbf{k}] - f[n'\mathbf{k}]) \\
 &\quad \times \langle n'\mathbf{k} | \hat{P}_r | n''\mathbf{k} \rangle \langle n''\mathbf{k} | \hat{P}_s | n'\mathbf{k} \rangle \\
 &\quad \times \left( - \frac{\delta\phi_{n'n''}(\mathbf{k}, \mathbf{k})}{\delta k_q} - [\chi_{n''q}(\mathbf{k}) - \chi_{n'q}(\mathbf{k})] \right) \\
 &\quad \times \delta(\omega_{n''}(\mathbf{k}) - \omega_{n'}(\mathbf{k}) \pm \omega)
 \end{aligned} \tag{5.1.1}$$

where  $n'$  and  $n''$  are band indices,  $\mathbf{k}$  is the wave vector in the Brillouin zone,  $\omega_k(\mathbf{k})$  is the energy of the  $n$ th band, so that  $\sigma_{rsq}$  gives the current density response  $\mathbf{J}$  to the EM-field  $\mathbf{E}$ ,  $\chi_{nq}(\mathbf{k})$  denotes the Berry connections for band  $n$  at  $\mathbf{k}$ , and  $\phi_{n'n''}$  is the phase of the transition dipole between the band  $n'$  and  $n''$ . With ferroelectric photovoltaics offering above band-gap photovoltages any the lack of  $p$ - $n$  junction it seems like they would be an excellent material for photovoltaics. We have briefly discussed the effects of using perovskite like materials for solar cell materials and in depth discussed the effects of the gold double perovskites as possible photovoltaic cells<sup>1</sup> We

<sup>1</sup>It is relatively clear that a lot of these structures that we discuss are not very suitable for photovoltaics. Experimentally gold double perovskite materials are extremely expensive to make, but it is a hope that the work combined in the previous chapters and this one will lead to an improvement in the understanding of ferroelectric photovoltaics

have discussed briefly some of the different ferroelectric materials but a lot of these are based in the ferroelectric non-layered materials. Examples of ferroelectric photovoltaics can include the the  $(n\text{-propylammonium})_2\text{CsAgBiBr}_7$  which exhibits a saturation polarisation of  $1.5\mu\text{C cm}^{-2}$ , more importantly this double perovskite also exhibits excellent photodetector performance with fast response rates and very high detectivity[202].  $\text{CuInP}_2\text{S}_6$  is another example of layered ferroelectric material with the large photovoltages and excellent optical properties. The CIPS structure has a curie temperature of 315K which allows it to operate at room temperature, a  $V_{oc}$  of 1.0V with the enhanced photocurrent density being two orders of magnitude higher than from ferroelectric perovskite oxides[203].

There has also been some interesting work carried out into anti Ruddlesden-Popper phases where the structure follows the  $\text{A}_4\text{X}_2\text{O}$  ( $\text{A}=\text{Ca}, \text{Sr}, \text{Ba}, \text{Eu}, \text{X}=\text{Sb}, \text{P}, \text{As}, \text{Bi}$ ), with different chemistries exhibiting either ferroelectric or anti-ferroelectric properties. For example the  $\text{Ba}_4\text{Sb}_2\text{I}$  offers a spontaneous polarisation of  $9.55\mu\text{C cm}^{-2}$ . More excitingly as well there is a band-gap with approximately 1.22eV, close to the optimal gaps of 1.3-1.4eV[204]. In this chapter we will be comparing the structural distortions that can appear in metal halide perovskite structures. The main focus will be on the Ruddlesden-Popper perovskite structure where we will examine how the size of the ferroelectric distortion changes with chemistry and observe how the band-gap and density of states also change with chemistry. Finally we discuss the optimal chemistry that not only has the largest amplitude of ferroelectric distortion but has the optimal band-gap of around 1.3eV to enable higher absorption of electrons[26]. Band-gaps too high and the amount of electrons being lifted to the conduction band is too low and the current will be considerably smaller. Band-gaps too low and the energy is mainly lost as heat. This full description is available in section 1.2.

## 5.2 Hybrid Improper Ferroelectricity

Ferroelectricity, a property of certain insulating and semiconducting materials is where there is a spontaneous polarisation that can be reversed with an external electric field.

In crystallographic terms the distortion appears due to a Brillouin zone-center ( $\Gamma$ ) point instability. This particular kind of ferroelectricity is called *proper ferroelectricity* and can appear generally in perovskite oxides with lone pairs of electrons or  $d^0$  arrangements. When using Landau Theory we can describe this as a second order phase transition:

$$(F - F_0) = a(T - T_c)P^2 + bP^4, \quad (5.2.1)$$

where  $a$  and  $b$  are positive coefficients,  $T$  and  $T_c$  are the temperature and critical temperature respectively. Unfortunately as mentioned in the introduction the majority of structures either do not have a polar instability which lowers the energy, or, if it does they do not have an optimal gap to readily absorb large portions of the visible light region[205, 206]. A lot of structures primarily do not have a polar distortion present, and if they do appear it is generally met with competition amongst other distortions which usually include tilts and rotations (See Chapter 3). *hybrid Improper Ferroelectricity* is a type of geometric ferroelectricity which produces a polar distortion through the coupling of two non-polar distortions. This coupling is through an odd-order coupling of term of the free energy and can be described as:

$$F_{hybrid} \propto Q_1 Q_2 P, \quad (5.2.2)$$

In order for this odd-order coupling term to appear there has to be a conservation of crystal momentum and parity with respect to inversion symmetry. Therefore any two distortions that transform as  $X^-$  and  $X^+$ , or  $M^-$  and  $M^+$  or  $R^-$  and  $R^+$  collectively will couple to a non-centrosymmetric distortion (usually a  $\Gamma^-$  distortion). In a complete description of the equation 5.2.2 we would see other terms containing the polar distortion  $\Gamma^-$ , but those terms would seek to raise the overall energy of the system. The overall energy of the system will therefore only be lowered to allow the appearance of a polar distortion through the two non-polar distortions that appear. Therefore the polar distortion is not a primary order parameter, similar to that of a *proper* ferroelectric but a secondary order parameter, an *improper ferroelectric*.

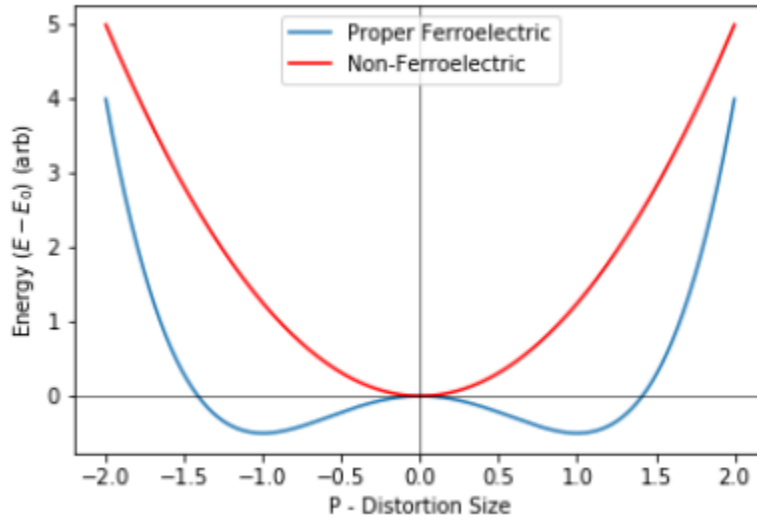


Figure 5.1

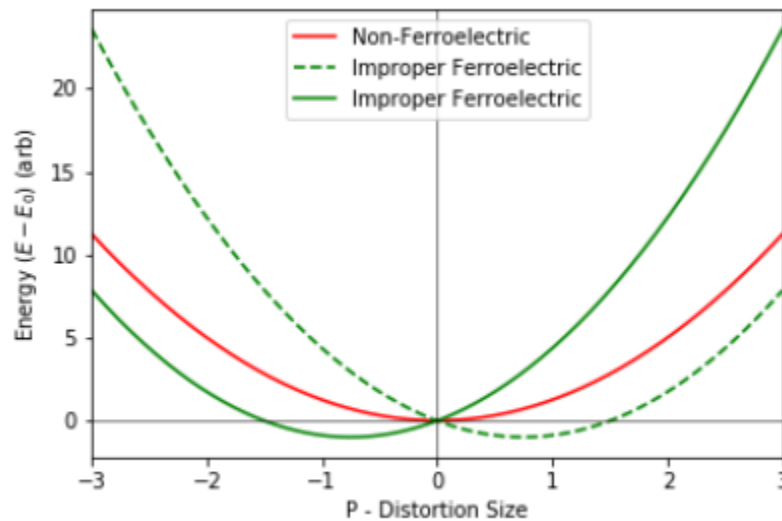


Figure 5.2: (a) The figure shows a graphical representation of the high and low-symmetry phases for *proper* ferroelectric, which follows equation 5.2.1. (b) Graphical representation of the free energy for an improper ferroelectric with a non-ferroelectric highlighted in red and the two associated improper ferroelectric phases.

Although the polar distortion is now a secondary order parameter in the improper mechanism, the reversal of the polarisation happens through a different mechanism. In a proper ferroelectric, as discussed, the polarisation can be reversed through an external electric field and as shown by Figure 1.12. Through the improper mechanism the polarisation can only be reversed through the reversal of one of the non-polar distortions. We can describe this numerically. If  $Q_1 = Q_2$  then the polarisation will not appear due to lack of inversion symmetry breaking. If however,  $Q_1 \neq Q_2$  and the crystal momentum is conserved and parity is opposite then the polarisation will occur through an odd-order (usually trilinear) coupling term. Reversal of such one of the distortions  $Q_1 \cdot -Q_2$  the polarisation will then also reverse. Reversal of both non-polar distortions will lead to polarisation to an overall no change. Within this review we will be examining the improper mechanism by looking at the coupling between two non-polar tilt distortions.

### 5.3 Computational Methods

We employed ab initio methods based on Density Functional Theory (DFT) in combination with post-analysis tools. Here, the VASP (Vienna ab initio Simulation Package) DFT code was utilised [130, 131, 132, 133] with PAW (Projector Augmented Wave) pseudopotentials [110, 134], and the Generalised Gradient Approximation (GGA) exchange-correlation functional PBESol [135]. The Pb *5d* electrons were treated as valence. An energy cutoff of 700eV was used for the plane-wave basis, and a  $8 \times 8 \times 4$  and  $2 \times 8 \times 8$  MonkhorstPack grid [136] for the *I4/mmm* and *Cmc2<sub>1</sub>* respectively. Symmetry mode analysis was performed with AMPLIMODES [137, 138], ISODISTORT [139] and FINDSYM [116]. We employed the Density Functional Perturbation Theory (DFPT) method to determine dynamical instabilities [140] with energies minimised to  $10^{-9}$  eV and forces minimised to  $10^{-6}$  eV/Å. Spin-Orbit coupling was not employed on mass in this body of work due to its large computational cost but it is appreciated that it can have an effect on the results and this is something we discuss at the end of this chapter. Bandstructure, density of states and effective masses were determined

using the sumo package[141].

## 5.4 Results

In this section we will look initially at the structural analysis of the high and low symmetry phases. The low symmetry phase in our case allows for the HIFE mechanism to appear. We will also examine the non-layered system phase and show that the HIFE mechanism does not appear in this particular structure. Secondly we will discuss the bandstructure of the  $\text{Cs}_3\text{Pb}_2\text{I}_7$  phase to show the appearance of the band opening through the appearance of both the tilt distortions that become present in the material and finally we will examine the effects of chemical substitution on the band-gap and the size of the polar distortion.

### Structural Analysis of the $I4/mmm$ and $Cmc2_1$ Phases

It was important that all of our structures were sufficiently relaxed. Whereas in the previous chapters we initially used the Murnaghan equation of state to determine the optimum volume and then compared this to the results from VASP itself to keep ourselves as rigorous as possible. In this chapter we worked on nine different structures of differing chemistry, starting from the  $\text{Cs}_3\text{Pb}_2\text{I}_7$  structure. We systematically changed each of the elements. For example we examined the effects of changing the A-site cation then B-site cation then finally the X-site anion of the Ruddlesden-Popper  $\text{A}_3\text{B}_2\text{X}_7$ . We did not look at the intermediaries such as  $\text{Rb}_3\text{Ge}_2\text{I}_7$  as we wanted to observe the effects of changing each of the cation/anions - It would be possible to estimate the effects of such subsequent structures just by knowing the patterns between these three different chemical paths. Initially the work looked at the cubic  $Pm\bar{3}m$  structure. The initial purpose of this is to prove that the effects of tilting in the same K-space with the same parity does not enable the introduction of the HIFE mechanism - an additional complexity of layering is required to break this the centrosymmetry of the crystal to enable to trilinear coupling term to appear. We observed the phonons of the  $\text{CsPbI}_3$  phase and found two distortions present one

present at the  $R$  and another at the  $M$  points. We know from the varying crystal momentum as described by the distortions present in the  $Pnma$  phase that our  $Pm\bar{3}m \rightarrow Pnma$  phase transition does produce a polar ground state. Structural analysis was carried out on the structure  $\text{CsPbI}_3$  as produced by Straus *et al.*[207]. As shown in

Structure	Irrep	Amplitude (Å)
$\text{CsPbI}_3$	$\left( \begin{array}{c} R_4^- \\ R_5^- \\ X_5^- \\ M_2^+ \\ M_3^+ \end{array} \right)$	$\left( \begin{array}{c} 0.39 \\ 1.92 \\ 1.34 \\ 1.85 \\ 0.08 \end{array} \right)$

Table 5.1: Representation and magnitude of distortions from the  $\text{CsPbI}_3$  high symmetry cubic  $Pm\bar{3}m$  to the low-symmetry  $Pnma$  structure.

Table 5.1 we can see that a polar distortion which usually translates to a  $\Gamma^-$  distortion does not appear. We therefore explored the effects of layering on the appearance of an improper mechanism for the appearance of a polarisation. Condensing these distortions and further relaxation with subsequent analysis shows the appearance of a  $\Gamma_5^-$  which corresponds to our polar structure. The combination of the three distortions drives the structure to a  $Cmc2_1$  phase as shown in Figure 5.3. In this phase we see the HIFE mechanism in play where the two non-polar centrosymmetric rotations of the  $\text{BX}_6$  octahedra drive the non-centrosymmetric polar distortion to appear. We used INVARIANTS to show how these distortions couple together:

$$\begin{aligned}
 (F - F_0) = & a_1 Q_{(X_2^+)}^2 + b_1 Q_{(X_2^+)}^4 \\
 & + a_2 Q_{(X_3^-)}^2 + b_2 Q_{(X_3^-)}^4 \\
 & + a_3 Q_{(\Gamma_5^-)}^2 + b_3 Q_{(\Gamma_5^-)}^4 \\
 & + C_{1,2} Q_{(X_2^+)}^2 Q_{(X_3^-)}^2 + C_{1,3} Q_{(X_2^+)}^2 Q_{(\Gamma_5^-)}^2 + C_{2,3} (X_3^-)^2 (\Gamma_5^-)^2 \\
 & + \boxed{(X_2^+) Q_{(X_3^-)} Q_{(\Gamma_5^-)}} \tag{5.4.1}
 \end{aligned}$$

As highlighted at the bottom of the equation above we see a trilinear coupling term between the two non-polar tilt distortions and the polar distortion. This mechanism

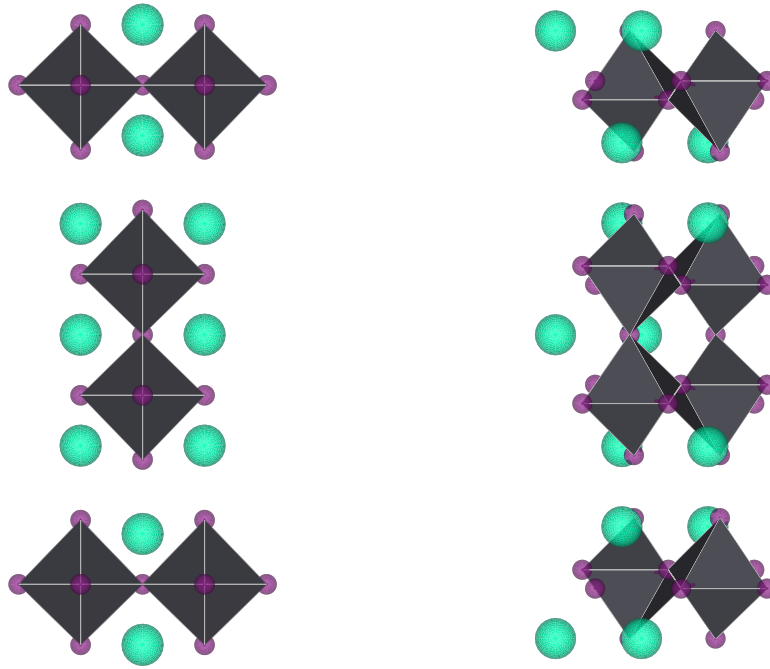


Figure 5.3: a) High-symmetry  $I4/mmm$  structure of the  $\text{Cs}_3\text{Pb}_2\text{I}_7$ . b) low-symmetry  $Cmc2_1$  structure of  $\text{Cs}_3\text{Pb}_2\text{I}_7$ . The  $Cmc2_1$  phase has both the  $X_3^-$  and the  $X_2^+$  distortion present.

is present in all but one of our structures, therefore I will not spend too much time discussing the physical distortions present in the majority of these structures. What we can see is the size of the distortions as we change the chemistry of our structure and the effect that this has on the band-gap of their respective structures.

### Electronic Structure of $I4/mmm$ and $Cmc2_1$

In this section we will look at the electronic structure of the  $Cmc2_1$  phase of the  $\text{Cs}_2\text{Pb}_3\text{I}_7$ . As previously discussed the motivation behind this research stems from the relatively high band-gaps that oxide perovskites possess. Here we look at the band-structure of both the high and low-symmetry  $I4/mmm$  and  $Cmc2_1$  phases respectively. The initial purpose is to determine the effects of the distortions on the structure of the bands and thus the band-gap of the materials. As we have spoken about in

the previous section the effect of tilts on the bands is generally the increase of the gap. McGehee *et. al* have shown that band-gap tuning of lead and tin iodide perovskites is possible through compositional substitution which show differing amplitudes of the respective tilt distortions[169].

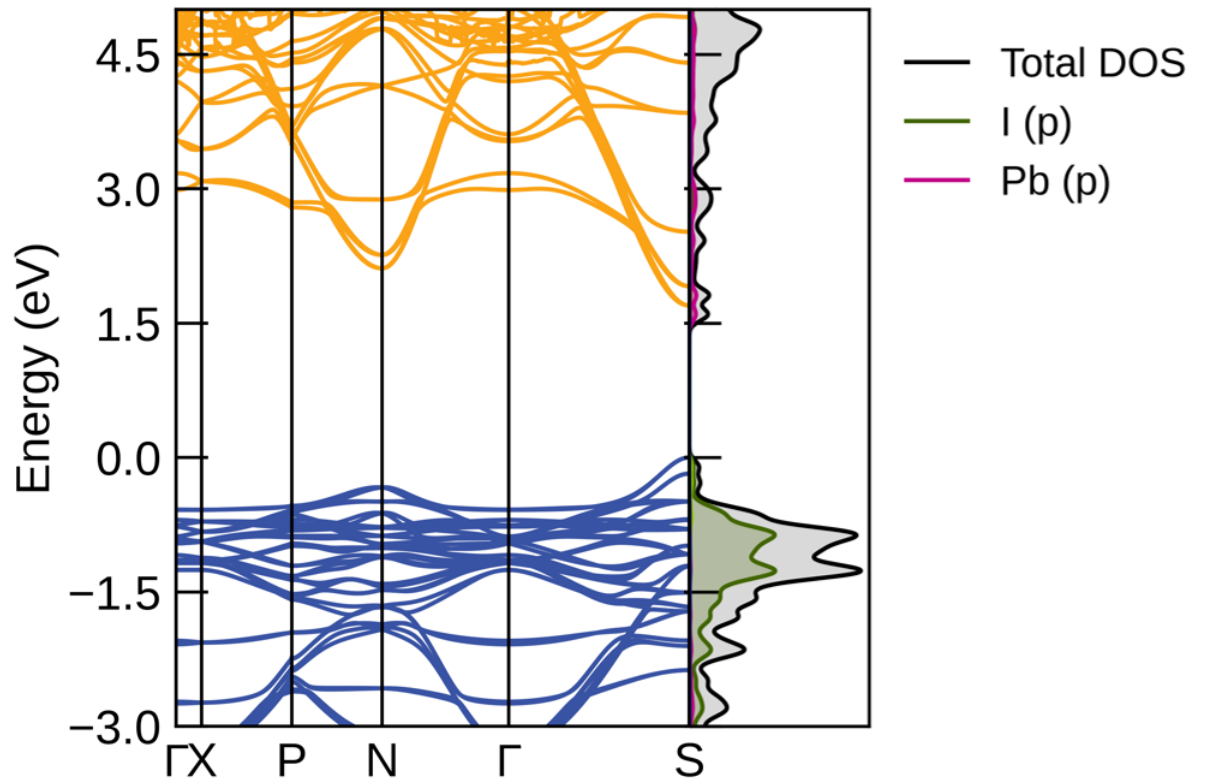


Figure 5.4: Bandstructure and Density of states for the  $I4/mmm$   $\text{Cs}_3\text{Pb}_2\text{I}_7$  phase. The density of states highlight the effects of which orbitals contribute the most to the conduction and valence bands.

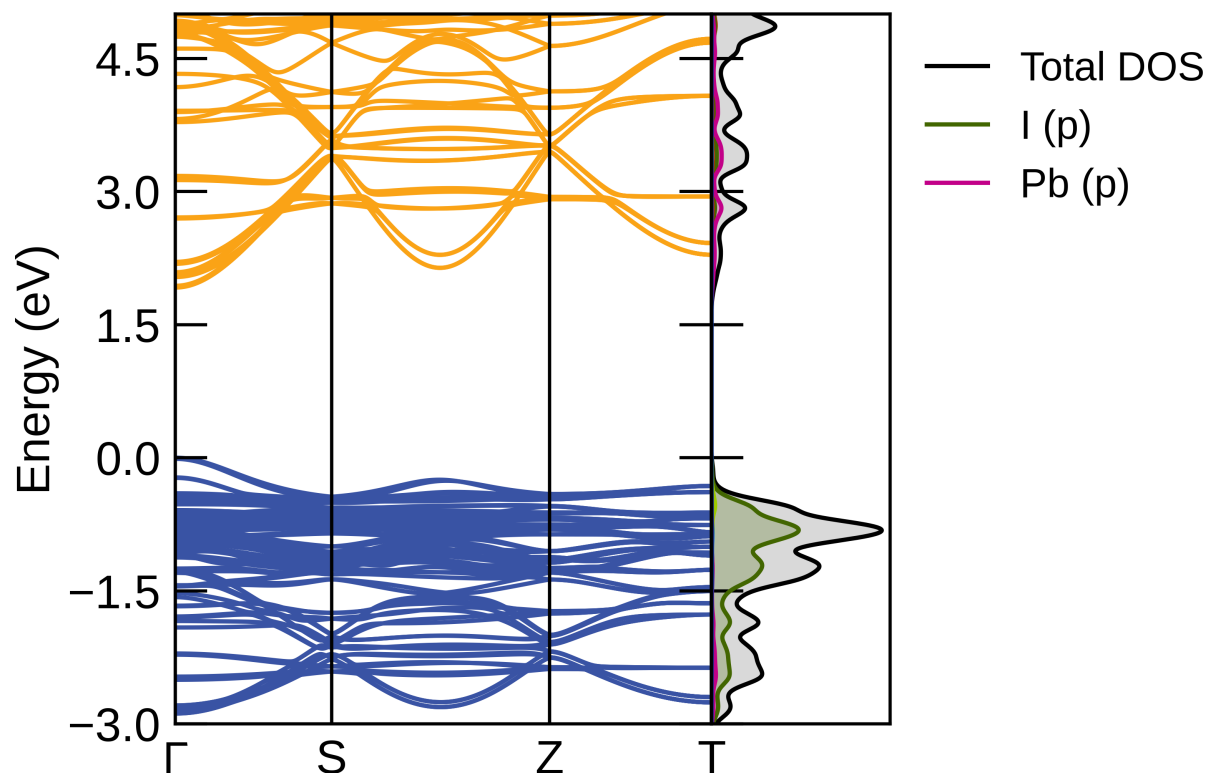


Figure 5.5: Bandstructure and density of states for the  $Cmc2_1$   $Cs_3Pb_2I_7$  phase. The density of states highlight the effects of which orbitals contribute the most to the conduction and valence bands. The band-gap which is direct and 1.83eV is at the  $\Gamma$  point.

The purpose of this project is to determine ideal chemical composition of the Ruddlesden-Popper structure which enables a high-degree of charge separation through a large polar distortion and a suitable band-gap. Here we look at the different chemical compositions and examine the sizes of distortions, the tolerance factor and the band-gap of both the high and low symmetry phases. Table 5.2. summarises all of these key discoveries. We can see some clear trends in the data that has been collated. Dependent on whether we are looking at the A, B or X atom in our structure changes how we see the trends. Overall a reduction in the tolerance factor leads to an

Table 5.2: Changes in band-gap for both the  $I4/mmm$  and  $Cmc2_1$  Ruddlesden-Popper phases with varying chemistry. Amplitudes are described for the phase transition  $Pm\bar{3}m \rightarrow Cmc2_1$ .

Compound	Tolerance Factor ( $t$ )	Amplitudes ( $\text{\AA}$ )	BG (eV) $Cmc2_1$	BG (eV) $I4/mmm$
$\text{Cs}_3\text{Pb}_2\text{I}_7$	0.85	$\begin{pmatrix} X_2^+ \\ X_3^- \\ \Gamma_5^- \end{pmatrix} \rightarrow \begin{pmatrix} 1.37 \\ 2.03 \\ 1.28 \end{pmatrix}$	1.83	1.63
$\text{Cs}_3\text{Sn}_2\text{I}_7$	0.91	$\begin{pmatrix} X_2^+ \\ X_3^- \\ \Gamma_5^- \end{pmatrix} \rightarrow \begin{pmatrix} 0.85 \\ 1.57 \\ 0.83 \end{pmatrix}$	1.13	0.82
$\text{Cs}_3\text{Ge}_2\text{I}_7$	0.98	$\begin{pmatrix} X_2^+ \\ X_3^- \\ \Gamma_5^- \end{pmatrix} \rightarrow \begin{pmatrix} 0.01 \\ 0.03 \\ 1.22 \end{pmatrix}$	1.30	1.08
$\text{Cs}_3\text{Pb}_2\text{Br}_7$	0.86	$\begin{pmatrix} X_2^+ \\ X_3^- \\ \Gamma_5^- \end{pmatrix} \rightarrow \begin{pmatrix} 1.31 \\ 1.80 \\ 1.16 \end{pmatrix}$	2.34	2.05
$\text{Cs}_3\text{Pb}_2\text{Cl}_7$	0.87	$\begin{pmatrix} X_2^+ \\ X_3^- \\ \Gamma_5^- \end{pmatrix} \rightarrow \begin{pmatrix} 1.08 \\ 1.69 \\ 0.92 \end{pmatrix}$	2.75	2.36
$\text{Rb}_3\text{Pb}_2\text{I}_7$	0.81	$\begin{pmatrix} X_2^+ \\ X_3^- \\ \Gamma_5^- \end{pmatrix} \rightarrow \begin{pmatrix} 1.87 \\ 2.87 \\ 1.88 \end{pmatrix}$	2.02	1.66
$\text{K}_3\text{Pb}_2\text{I}_7$	0.80	$\begin{pmatrix} X_2^+ \\ X_3^- \\ \Gamma_5^- \end{pmatrix} \rightarrow \begin{pmatrix} 2.09 \\ 3.50 \\ 2.22 \end{pmatrix}$	2.23	1.68

overall increase in the size of the tilts. Due to the trilinear coupling term we see an increase in the size of the polar distortion - which is good for the overall separation of charges in the material. It does however increase the band-gap of the material. As we have previously discussed in Chapter 4 this is due to the tilt distortions being present in the structure. The data on an individual A, B and X basis shows us that as we reduce the size of the A-site cation from Cs  $\rightarrow$  Rb  $\rightarrow$  K, the overall ionic size of the atom decreases by 18% overall, This consequently leads gives an approximate 5% decrease in the tolerance factor and a 22% increase in the band-gap. This is reflected in the large increase in both  $X_2^+$  and  $X_3^-$  distortions. Interestingly we do not see such an increase in the band-gap value for the low symmetry phase.

X-site cation changes see the opposite effect, with an overall ionic radii reduction of 17.72% we see a much smaller 2.35% increase in the tolerance factor. A general increase in the tolerance factor reduces the size of tilt distortions and thus we see a reduction in the polar distortion. It is clear that the X-site anions play an important role in the size of the band-gaps as we see a huge 50% increase in the size of the band-gap for the low-symmetry phase. It is clear that overlap of the p-orbitals of the anion and the d-orbitals of the B-site cation has been reduced as the size of the X-site anion is decreased. This is has been shown experimentally with the vacancy ordered  $\text{Cs}_2\text{SnX}_6$  structure where the Cl perovskite structure exhibits a 4.89eV band-gap and the I-perovskite exhibits a 1.35eV band-gap[208]. It was also stated in this paper that the band-gap was non-linear with changes in composition which for the anions specifically in our case also followed suit. The B-site cations followed a different trend in terms of the band-gap and the overall size of the polar distortions. A reduction in size of the B-site cations from Pb  $\rightarrow$  Sn  $\rightarrow$  Ge of which is an overall reduction of 38% of the original size of the ionic radii. However, for this set of results we see some non-linear changes in the sizes of the tilt distortions, polar distortions and the band-gap. The overall expectancy when carrying out this project was an overall reduction in the size of the polar distortion in a generally linear way however, when we move from Sn  $\rightarrow$  Ge we see a large increase in the polar distortion but an almost complete removal of the tilt distortions. This leads us to believe that this structure

might not follow the improper mechanism but the proper mechanism, whereby the primary order parameter is now the polar distortion. Figure 5.6 shows the effects of tolerance factor/chemical substitution on the size of the distortions present. This is a graphical representation of the data summarised in Table 5.2. These lines are of the assumption that anything between these individual chemistries (solid solutions of different chemical makeups) follow a linear trend between them, however this is not overly expected.

### Discussion of Band-Gap

There needs to be a finely tuned balance between the size of the polar mode and the size of the distortions as there is a general trend between both. In the previous section we discussed the overall effects of the chemical substitution on the size of the distortions and the polar mode. Here we combine the analysis between both the band-gaps and the polar distortions. Figure 5.7 shows the relationship between the polar distortion and the band-gap. The golden region of the figure was designated based on the AM1.5 solar radiation spectrum which accesses the biggest range of photon energies. In this particular region we see only one particular chemistry which is the non-HIFE  $\text{Cs}_3\text{Ge}_2\text{I}_7$  where we see a band-gap of approximately 1.30eV, close to the *optimal* 1.6eV for photovoltaic cells. As we can clearly see from figure 5.7 we see the  $\text{Cs}_3\text{Ge}_2\text{I}_7$  sits in our self-proclaimed *golden* region. This is based on a combination of polar distortions and band-gap size. Although this looks promising in two of the most prominent properties needed for photovoltaic materials analysis of the literature notes some issues with the composition. Currently there are none or very few experimental papers which highlight this as a possible composition that can be synthesised which of course is disappointing. Where Germanium compounds are synthesised it is alongside an organic A-site cation like methylammonium. For example methylammonium germanium iodide can be synthesised has a power conversion efficiency of 0.2% which is incredibly low and suffers from really poor stability.

The introduction of bromine into the structure as a  $(\text{MA})\text{GeI}_{2.7}\text{Br}_{0.3}$  leads to a minor

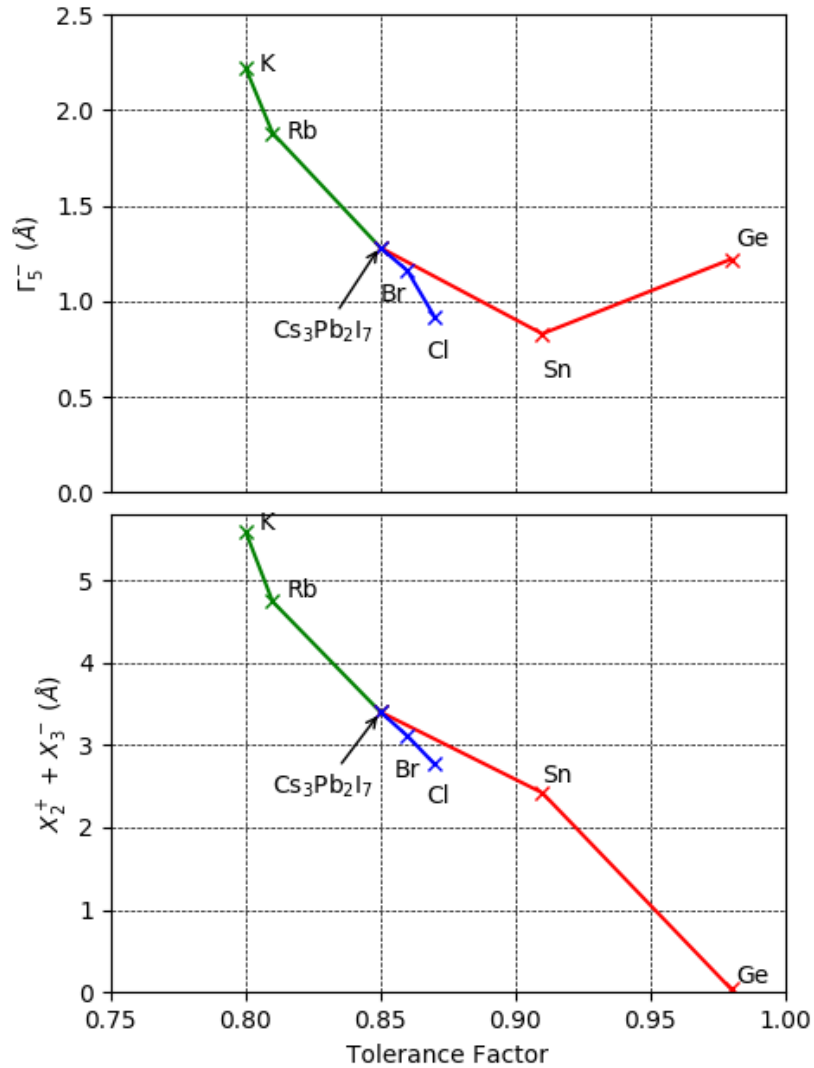


Figure 5.6: Graphical representation of the changing tilt distortions and polar distortions. Each individual colour represents chemical substitution of a particular cation/anion. The green path represents the change from Cs→K, blue I → Cl and finally red Pb → Ge. The  $\text{Cs}_3\text{Pb}_2\text{I}_7$  is labelled in the middle of each graph to represent the start of the changing chemical substitution.

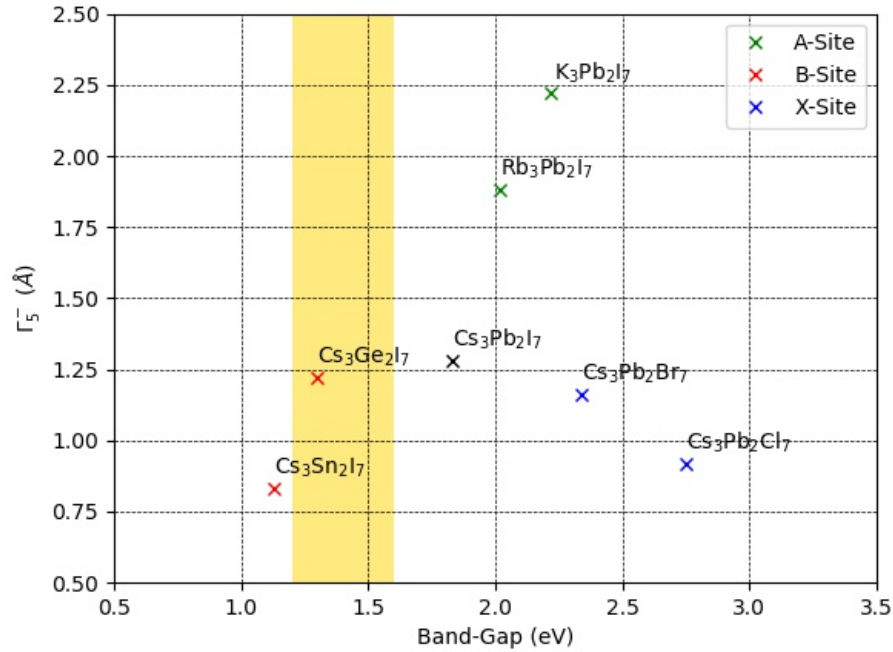


Figure 5.7: Relationship between the band-gap and the polar distortion. The golden region is highlighted to examine the band-gap for optimal solar AM1.5 photovoltaics.

increase in the PCE to 0.57%[\[37\]](#). On the contrary there has been further research which supports a much better PCE for the germanium halide perovskites, with the formamidinium germanium iodide supporting a 7% PCE[\[209\]](#).

### Functionals and Spin-Orbit Coupling

The final section is more of an overview for all of the chapters of this thesis. Throughout this research we have been making use of the GGA exchange-correlation functionals for our DFT calculations. However for this part of the thesis we examined the use of the meta-GGA SCAN and the use of Spin-Orbit Coupling on the effects of the bands. Figure 5.8 shows how the band gap for the  $I4/mmm$  phase of the three chemistries changes based on the input parameters that were selected. As we would

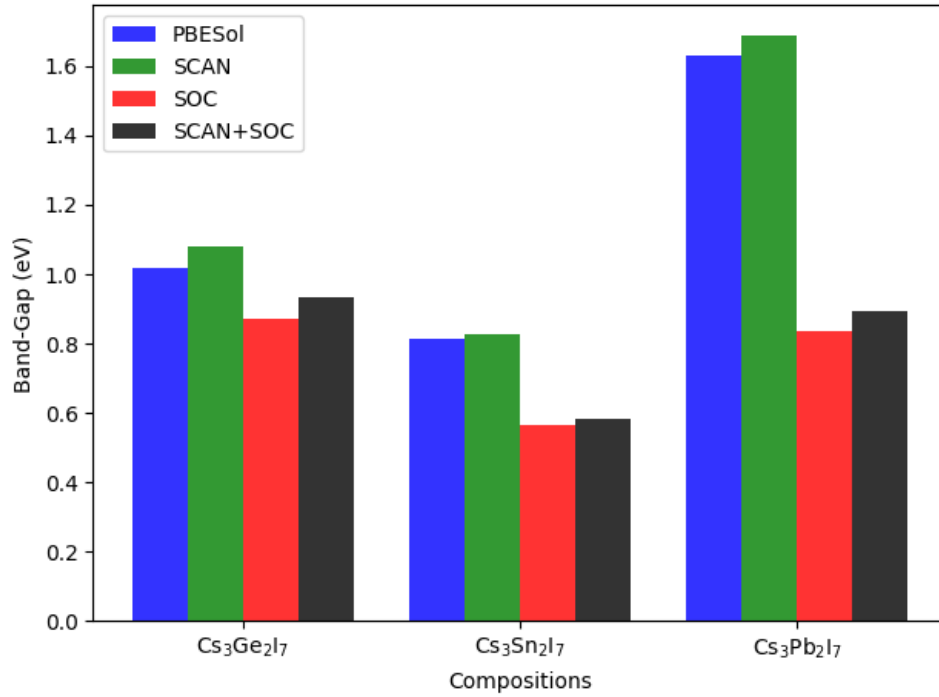


Figure 5.8: Analysis of the  $I4/mmm$  phases for PBESol, SOC, SCAN and SCAN+SOC.

expect SOC plays a large effect on the size of the gap for the B-site cations which are much heavier. Spin-Orbit coupling is an interaction between the spin of the electrons and their relativistic motion inside the electrostatic field which is generated by the charge nucleus of an atom. Because the charge of the nucleus increases as the atomic number of the atom increases the effects of spin-orbit coupling is very significant within larger atoms including Lead. This is why as shown in Figure 5.8 the effects on the band gap is significant, therefore if accurate values for band-gaps and other excited states want to be assessed then it does need to be included. It is also clear from Figure 5.8 that SCAN makes very insignificant changes to the overall band-gap of the structures here with predictions showing it more often than not underestimates the gap by approximately 27%[210]. Therefore to accurately map out an accurate electronic bandstructure we need to move further up the Jacob's Ladder (Figure 2.2). Hy-

brid functionals are the most likely to give more accurate values of the band-gap with the HSE06 functional usually accurately predicting bandstructures, but this always come with the largest computational expense. HLE16 would be an excellent functional for structures that have large values for spin-orbit coupling and is competitive with the hybrid functionals[211]. We have however, for the purpose of this study been looking at the overall trends for in the metal halide perovskites and how external factors can affect the electronic properties, therefore we did not find it overly necessary to use huge amounts of computing resources.

## 5.5 Conclusions and Final Remarks

This chapter reflected on the challenges that face the FE-PV community with the significant engineering problems around having a large ferroelectric distortion within photovoltaic materials with suitable band-gaps. We therefore explored the phenomenon of hybrid improper ferroelectricity where coupling between two non-polar modes gives rise to a polar mode, in our case the two non-polar modes are the rotation and tilts of the  $BX_6$  octahedra. Hybrid improper ferroelectricity can also appear due to the presence of a layered structure, in our case the Ruddlesden-Popper  $A_3B_2X_7$ . The results in this chapter exhibited the effects of hybrid improper ferroelectricity through the coupling of two non-polar rotations and tilts ( $X_2^+$  and  $X_3^-$ ) with the polar distortion  $\Gamma_5^-$  and this was displayed through the symmetry analysis and the group-supgroup relations. Exploration of the bandstructures and density of states showed the effects of these distortions on the band-gap showed that we see a reduction in the dispersion of the bands and the changing value of the band-gap.

We explored the effects of chemical substitution on the band-gap and developed some trends in both the values found for the gap and the size of the distortions itself. Overall the trends generally fit with predictions of the anions and cations but we saw a change for the  $Cs_3Ge_2I_7$  where the overall trend of the  $X_2^+$  and  $X_3^-$  decreasing for the B-site cation lead to an overall increase in the  $\Gamma_5^-$ . This led to some further work where we discovered that the  $Cs_3Ge_2I_7$  structure fits the  $Imm2$  ground state

instead. Finally we discussed the overall picture and put forward some ideas of the ideal structure that could be put forward as an ideal FE-PV and discussed the future of metal halide perovskites as photovoltaics. Overall the results in this chapter have shed a light and developed some key understanding in the effects of hybrid improper ferroelectricity for photovoltaics in metal halide perovskites. It is important to note that this entire project was theoretical and the majority of these structures have not been synthesised before but it is with hope the process can be applied to other structures for ferroelectric photovoltaics and functional solar cells.



# Conclusions, Final Remarks and Future Work

*People do not like to think. If one thinks, one must reach conclusions. Conclusions are  
not always pleasant*

- Helen Keller

The work presented in this thesis is a culmination of our desire to combine the electronic and sterical properties of inorganic metal halide perovskites. What we have explored here is the synonymous link between the various distortions that are found in both the gold double perovskite and Ruddlesden-Popper metal halide perovskites and the electronic and photovoltaic properties that they possess.

### Chapter 3: Structural Analysis

We primarily wanted to explore a range of chemistries that already appear in the experimental literature. This allowed us to explore the complex array of distortions through the parent-daughter relationships in great depth. We discovered a complex interplay between several distortions as we progress from the relatively simple  $I4/mmm$  with its two distortions, the breathing and Jahn-Teller distortions to more complex structures like the  $K_2Au_2I_6$   $P2_1/c$  structure, with six distortions present. In this chapter we then explored the appearance of a polar distortions present in some of the structures. It is not overly clear on the origin of this distortion in the various structures explored and it would be beneficial for somebody in the future to explore the origin of this polar distortion, whether it be proper or improper. From our calculations it looks that the  $R_5^-$  anti-polar distortion is very small and would suggest numerical noise in the process and its important to see whether this is truly appears in the structure or not. The work presented in this chapter was a grounding in the structural understanding of these structures and lead us down a path to the more interesting and commercially important electronic properties.

### Chapter 4: Optoelectronic Analysis

This chapter was an extension of the work completed in the previous. We applied our understanding of these distortions in the variety of different structures to observe the effects on the electronic properties. We found a plethora of different electronic properties in the gold materials which suggests that such materials could be excellent as

part of solar light absorbers. We found suitable band gaps, the possibility of effective charge mobility and more interestingly enhanced charge separation through a large dielectric constant. Due to the fact that gold is within the material it is clear that this material specifically would not be commercially viable due to its high cost. There needs to be a more thorough exploration of different double perovskite materials with more viable elements substituted in place of the gold. Firstly, computationally there should be some exploration of a solid-solution of the Br-I compounds in an attempt to increase the dielectric constant even further, this could subsequently lead to a polar distortion which enables enhanced photovoltages and charge separation. Secondly, there needs to be a more comprehensive understanding of the bandgaps suggested in this chapter with the use of hybrid functionals to give a clearer picture of the exact gaps we could expect. Finally, with a deeper study of the literature and understanding of the electronic structure of charge-ordered double perovskites, substitution of the gold sites could lead to more experimental work being put forward and understanding of the general stability of said materials. Importantly it was clear in this thesis that the polar distortion is small, therefore an understanding of its ability to separate charge effectively will decide whether these materials should be pushed forward as a possible candidate for solar light absorbers.

### **Chapter 5: Hybrid Improper Ferroelectricity**

In this final chapter we explored the possibility of observing a large polar distortion in Ruddlesden-Popper halide perovskites through an improper ferroelectric mechanism. Much like the previous chapters we explored a large array of different structures in terms of chemical substitution. Analysis of these different structures allowed us to develop a comprehensive understanding of both the band-gap of the materials and the size of the polar distortion. We explored the trends in the chemical substitution in terms of the gap and polar distortion and found some structures which were more interesting than others. Computationally more exploration of the structures could be examined especially in terms of the band-gap in the materials. The heavy B-site cations

can give rise to under representation of the band-gap and this needs to be corrected through the use of Spin-Orbit Coupling and hybrid functional analysis. There also needs to be a more thorough exploration of the possibility of the  $\text{Cs}_3\text{Ge}_2\text{I}_7$  structure. This shows promising results but also there are gaps in the understanding of the origin of the polar distortion and this needs exploring. The work in this chapter has also loaned itself to more structures which are generally nowadays frowned upon, in the fact that lead is highly toxic, but, we have shown that there are materials which enable suitable band-gaps for light absorption and also very large polar distortions which can give rise to exceptional charge separation.

### **Final Remarks**

In this thesis we have explored the effects of the sterical with the electronic and although we have explored several structures which unfortunately do not lend themselves to commercial viability with toxicity involved (Lead) and extreme cost (Gold) we have shown that these materials possess some incredible properties which could support the hunt for a solar light absorber or a material which can assist in the increase in PCE for solar cells. Of course we have been incredibly computationally focused and my suggestion would be a more comprehensive literature exploration of materials that could support the  $d^8 - d^{10}$  splitting of charge on the B-site cation of a double perovskite and a full exploration of these materials which exhibit some exceptional electronic properties. For an experimentalist the work in this thesis should be able to show the link between understanding of the coupling distortions that can appear in phase transitions and our understanding of the electronic properties.

# Bibliography

- [1] UN. Projected world population.
- [2] J. Jouzel, V. Masson-Delmotte, O. Cattani, G. Dreyfus, S. Falourd, G. Hoffmann, B. Minster, J. Nouet, J. M. Barnola, J. Chappellaz, H. Fischer, J. C. Gallet, S. Johnsen, M. Leuenberger, L. Loulergue, D. Luethi, H. Oerter, F. Parrenin, G. Raisbeck, D. Raynaud, A. Schilt, J. Schwander, E. Selmo, R. Souchez, R. Spahni, B. Stauffer, J. P. Steffensen, B. Stenni, T. F. Stocker, J. L. Tison, M. Werner, and E. W. Wolff. Orbital and millennial antarctic climate variability over the past 800,000 years. *Science*, 317(5839):793–796, 2007.
- [3] Hannah Ritchie, Max Roser, and Pablo Rosado. Electricity mix, Nov 2020.
- [4] Kyoto Protocol. Kyoto protocol. *UNFCCC Website. Available online: [http://unfccc.int/kyoto\\_protocol/items/2830.php](http://unfccc.int/kyoto_protocol/items/2830.php) (accessed on 1 January 2011)*, 1997.
- [5] Paris Agreement. Paris agreement. In *Report of the Conference of the Parties to the United Nations Framework Convention on Climate Change (21st Session, 2015: Paris)*. Retrived December, volume 4, page 2017. HeinOnline, 2015.
- [6] Alan Chodos. This month in physics history.
- [7] D. M. Chapin, C. S. Fuller, and G. L. Pearson. A New Silicon p-n Junction Photocell for Converting Solar Radiation into Electrical Power. *Journal of Applied Physics*, 25(5):676–677, May 1954.

- 
- [8] NREL. Best research-cell efficiency chart.
- [9] Jongseung Yoon, Sungjin Jo, Ik Su Chun, Inhwa Jung, Hoon-Sik Kim, Matthew Meitl, Etienne Menard, Xiuling Li, James J. Coleman, Ungyu Paik, and John A. Rogers. Gaas photovoltaics and optoelectronics using releasable multilayer epitaxial assemblies. *Nature*, 465(7296):329–333, May 2010.
- [10] X. Zhang, P. Kung, D. Walker, J. Piotrowski, A. Rogalski, A. Saxler, and M. Razeghi. Photovoltaic effects in gan structures with p-n junctions. *Applied Physics Letters*, 67(14):2028–2030, 1995.
- [11] Elaissa Trybus, Gon Namkoong, Walter Henderson, Shawn Burnham, W. Alan Doolittle, Maurice Cheung, and Alexander Cartwright. Inn: A material with photovoltaic promise and challenges. *Journal of Crystal Growth*, 288(2):218–224, 2006. Proceedings of the Second ONR International Indium Nitride Workshop Kailua-Kona, Hawaii 9-13 January 2005.
- [12] Frank Dimroth, Thomas ND Tibbits, Markus Niemeyer, Felix Predan, Paul Beutel, Christian Karcher, Eduard Oliva, Gerald Siefer, David Lackner, Peter Fuß-Kailuweit, et al. Four-junction wafer-bonded concentrator solar cells. *IEEE Journal of Photovoltaics*, 6(1):343–349, 2015.
- [13] Akihiro Kojima, Kenjiro Teshima, Yasuo Shirai, and Tsutomu Miyasaka. Organometal halide perovskites as visible-light sensitizers for photovoltaic cells. *Journal of the American Chemical Society*, 131(17):6050–6051, 2009. PMID: 19366264.
- [14] In Chung, Jung-Hwan Song, Jino Im, John Androulakis, Christos D. Malliakas, Hao Li, Arthur J. Freeman, John T. Kenney, and Mercouri G. Kanatzidis. Csn<sub>3</sub>: Semiconductor or metal? high electrical conductivity and strong near-infrared photoluminescence from a single material. high hole mobility and phase-transitions. *Journal of the American Chemical Society*, 134(20):8579–8587, 2012. PMID: 22578072.

- [15] Qidong Tai, Kai-Chi Tang, and Feng Yan. Recent progress of inorganic perovskite solar cells. *Energy Environ. Sci.*, 12:2375–2405, 2019.
- [16] Barbara Pinho. Solar cells perovskite films made at record low cost and speed, Dec 2020.
- [17] Samuel D. Stranks and Henry J. Snaith. Metal-halide perovskites for photovoltaic and light-emitting devices. *Nature Nanotechnology*, 10(5):391–402, May 2015.
- [18] Faming Li and Mingzhen Liu. Recent efficient strategies for improving the moisture stability of perovskite solar cells. *J. Mater. Chem. A*, 5:15447–15459, 2017.
- [19] Sebastian Pont, Daniel Bryant, Chieh-Ting Lin, Nicholas Aristidou, Scot Wheeler, Xuerui Ma, Robert Godin, Saif A. Haque, and James R. Durrant. Tuning  $\text{CH}_3\text{NH}_3\text{Pb}(\text{I-xBr}_x)_3$  perovskite oxygen stability in thin films and solar cells. *J. Mater. Chem. A*, 5:9553–9560, 2017.
- [20] Isabel Mesquita, Luísa Andrade, and Adélio Mendes. Perovskite solar cells: Materials, configurations and stability. *Renewable and Sustainable Energy Reviews*, 82:2471–2489, 2018.
- [21] Insung Hwang, Minki Baek, and Kijung Yong. Core/shell structured  $\text{TiO}_2/\text{CdS}$  electrode to enhance the light stability of perovskite solar cells. *ACS Applied Materials & Interfaces*, 7(50):27863–27870, 2015. PMID: 26615978.
- [22] Miaoqiang Lyu, Jung-Ho Yun, Peng Chen, Mengmeng Hao, and Lianzhou Wang. Addressing toxicity of lead: Progress and applications of low-toxic metal halide perovskites and their derivatives. *Advanced Energy Materials*, 7(15):1602512, 2017.
- [23] Ranbir Singh and Mritunjaya Parashar. *Origin of Hysteresis in Perovskite Solar Cells*, chapter Chapter 1, pages 1–1–1–42.

- 
- [24] *The physics of Solar Cells*. Taylor amp; Francis Ltd, 2017.
- [25] NREL. Reference air mass 1.5 spectra.
- [26] William Shockley and Hans J. Queisser. Detailed balance limit of efficiency of p-n junction solar cells. *Journal of Applied Physics*, 32(3):510–519, 1961.
- [27] Kunal Ghosh. Heterojunction and nanostructured photovoltaic device: Theory and experiment. phdph. d. thesis, Arizona State University, 2011.
- [28] M.A. Green, F.D. King, and J. Shewchun. Minority carrier mis tunnel diodes and their application to electron- and photo-voltaic energy conversion—i. theory. *Solid-State Electronics*, 17:551 – 561, Jan-06-1974 1974.
- [29] Pn junction theory for semiconductor diodes, Jan 2018.
- [30] Rongqing Hui. Chapter 4 - photodetectors. In Rongqing Hui, editor, *Introduction to Fiber-Optic Communications*, pages 125–154. Academic Press, 2020.
- [31] Electrical characterization of organic and perovskite solar cells.
- [32] FA. Lindholm, J.G. Fossum, and E.L. Burgess. Application of the superposition principle to solar-cell analysis. *IEEE Transactions on Electron Devices*, 26(3):165–171, 1979.
- [33] Minu Mohan. Chapter 14 - perovskite photovoltaics: Life cycle assessment. In Sabu Thomas and Aparna Thankappan, editors, *Perovskite Photovoltaics*, pages 447–480. Academic Press, 2018.
- [34] Charles M. Culbertson, Alexander T. Flak, Michael Yatskin, Paul H.-Y. Cheong, David P. Cann, and Michelle R. Dolgos. Neutron total scattering studies of group ii titanates (at<sub>10</sub>3, a<sub>2+</sub> = mg, ca, sr, ba). *Scientific Reports*, 10(1):3729, Feb 2020.

- [35] Xianyuan Jiang, Zihao Zang, Yuanyuan Zhou, Hansheng Li, Qi Wei, and Zhi-jun Ning. Tin halide perovskite solar cells: An emerging thin-film photovoltaic technology. *Accounts of Materials Research*, 2(4):210–219, 2021.
- [36] Jiupeng Cao and Feng Yan. Recent progress in tin-based perovskite solar cells. *Energy Environ. Sci.*, 14:1286–1325, 2021.
- [37] Indira Kopacic, Bastian Friesenbichler, Sebastian F. Hoefler, Birgit Kunert, Harald Plank, Thomas Rath, and Gregor Trimmel. Enhanced performance of germanium halide perovskite solar cells through compositional engineering. *ACS Applied Energy Materials*, 1(2):343–347, 2018.
- [38] V. M. Goldschmidt. Die gesetze der krystallochemie. *Naturwissenschaften*, 14(21):477–485, May 1926.
- [39] R. D. Shannon. Revised effective ionic radii and systematic studies of interatomic distances in halides and chalcogenides. *Acta Crystallographica Section A*, 32(5):751–767, Sep 1976.
- [40] Reza Asiaie, Weidong Zhu, Sheikh A. Akbar, and Prabir K. Dutta. Characterization of submicron particles of tetragonal batio<sub>3</sub>. *Chemistry of Materials*, 8(1):226–234, 1996.
- [41] Matthew R. Linaburg, Eric T. McClure, Jackson D. Majher, and Patrick M. Woodward. Cs<sub>1-x</sub>Rb<sub>x</sub>PbCl<sub>3</sub> and Cs<sub>1-x</sub>Rb<sub>x</sub>PbBr<sub>3</sub> solid solutions: Understanding octahedral tilting in lead halide perovskites. *Chemistry of Materials*, 29(8):3507–3514, 2017.
- [42] Giles E. Eperon, Samuel D. Stranks, Christopher Menelaou, Michael B. Johnston, Laura M. Herz, and Henry J. Snaith. Formamidinium lead trihalide: a broadly tunable perovskite for efficient planar heterojunction solar cells. *Energy Environ. Sci.*, 7:982–988, 2014.

- [43] Yun Hee Park, Inyoung Jeong, Seunghwan Bae, Hae Jung Son, Phillip Lee, Jinwoo Lee, Chul Ho Lee, and Min Jae Ko. Inorganic rubidium cation as an enhancer for photovoltaic performance and moisture stability of  $\text{hc}(\text{nh}_2)_2\text{pb}\text{i}_3$  perovskite solar cells. *Advanced Functional Materials*, 27(16), April 2017. Funding Information: Y.H.P. and I.J. contributed equally to this work. The authors thank Dr. Weon-Sik Chae, KBSI Daegu Center, for the fluorescence lifetime measurements. This work was supported from the Technology Development Program to Solve Climate Changes (2015M1A2A2056824) and the Global Frontier RD Program on Center for Multiscale Energy System (2012M3A6A7054856), funded by the National Research Foundation under the Ministry of Science, ICT Future Planning, Korea; this work was also supported by the KU-KIST Graduate School of Converging Science and Technology Program, and KIST institutional program. Publisher Copyright: © 2017 WILEY-VCH Verlag GmbH Co. KGaA, Weinheim.
- [44] Yi Hou, Xiaoyan Du, Simon Scheiner, David P. McMeekin, Zhiping Wang, Ning Li, Manuela S. Killian, Haiwei Chen, Moses Richter, Ievgen Levchuk, Nadine Schrenker, Erdmann Spiecker, Tobias Stubhan, Norman A. Luechinger, Andreas Hirsch, Patrik Schmuki, Hans-Peter Steinrück, Rainer H. Fink, Marcus Halik, Henry J. Snaith, and Christoph J. Brabec. A generic interface to reduce the efficiency-stability-cost gap of perovskite solar cells. *Science*, 358(6367):1192–1197, 2017.
- [45] Aurélien M. A. Leguy, Yinghong Hu, Mariano Campoy-Quiles, M. Isabel Alonso, Oliver J. Weber, Pooya Azarhoosh, Mark van Schilfhaarde, Mark T. Weller, Thomas Bein, Jenny Nelson, Pablo Docampo, and Piers R. F. Barnes. Reversible hydration of  $\text{ch}_3\text{nh}_3\text{pb}\text{i}_3$  in films, single crystals, and solar cells. *Chemistry of Materials*, 27(9):3397–3407, 2015.
- [46] Giles E. Eperon, Giuseppe M. Paternò, Rebecca J. Sutton, Andrea Zampetti, Amir Abbas Haghighirad, Franco Cacialli, and Henry J. Snaith. Inorganic cae-

- sium lead iodide perovskite solar cells. *J. Mater. Chem. A*, 3:19688–19695, 2015.
- [47] Rebecca J. Sutton, Marina R. Filip, Amir A. Haghighirad, Nobuya Sakai, Bernard Wenger, Feliciano Giustino, and Henry J. Snaith. Cubic or orthorhombic? revealing the crystal structure of metastable black-phase cspbi<sub>3</sub> by theory and experiment. *ACS Energy Letters*, 3(8):1787–1794, Aug 2018.
- [48] Qi Wang, Xiaopeng Zheng, Yehao Deng, Jingjing Zhao, Zhaolai Chen, and Jinsong Huang. Stabilizing the  $\alpha$ -phase of cspbi<sub>3</sub> perovskite by sulfobetaine zwitterions in one-step spin-coating films. *Joule*, 1(2):371–382, Oct 2017.
- [49] Lydia G. Burley, James H. Beecham-Lonsdale, Anant Kumar Srivastava, Ines E. Collings, and Paul J. Saines. Enhancing the chemical flexibility of hybrid perovskites by introducing divalent ligands. *Dalton Trans.*, 50:5437–5441, 2021.
- [50] J. A. Alonso, M. J. Martínez-Lope, M. T. Casais, and M. T. Fernández-Díaz. Evolution of the Jahn-Teller distortion of mno<sub>6</sub> octahedra in rmno<sub>3</sub> perovskites ( $r = \text{pr, nd, dy, tb, ho, er, y}$ ): A neutron diffraction study. *Inorganic Chemistry*, 39(5):917–923, 2000. PMID: 12526369.
- [51] Makoto Tachibana, Tomotaka Shimoyama, Hitoshi Kawaji, Tooru Atake, and Eiji Takayama-Muromachi. Jahn-teller distortion and magnetic transitions in perovskite  $r\text{MnO}_3$  ( $r = \text{Ho, er, tm, yb, and lu}$ ). *Phys. Rev. B*, 75:144425, Apr 2007.
- [52] Horng-Tay Jeng, Shi-Hsin Lin, and Chen-Shiung Hsue. Orbital ordering and Jahn-teller distortion in perovskite ruthenate sr<sub>2</sub>ruo<sub>3</sub>. *Phys. Rev. Lett.*, 97:067002, Aug 2006.
- [53] Graham King and Patrick M. Woodward. Cation ordering in perovskites. *J. Mater. Chem.*, 20:5785–5796, 2010.
- [54] Ravi Shankar P N, Fabio Orlandi, Pascal Manuel, Weiguo Zhang, P. Shiv Halasyamani, and Athinarayanan Sundaresan. A-site and b-site cation ordering

- induces polar and multiferroic behavior in the perovskite  $\text{Ln} = \text{y, dy, ho, and yb}$ ). *Chemistry of Materials*, 32(13):5641–5649, 2020.
- [55] P. M. Woodward. Octahedral Tilting in Perovskites. I. Geometrical Considerations. *Acta Crystallographica Section B*, 53(1):32–43, Feb 1997.
- [56] J. Valasek. Piezo-electric and allied phenomena in rochelle salt. *Phys. Rev.*, 17:475–481, Apr 1921.
- [57] V. Polinger, P. Garcia-Fernandez, and I.B. Bersuker. Pseudo jahn–teller origin of ferroelectric instability in  $\text{batio}_3$  type perovskites: The green’s function approach and beyond. *Physica B: Condensed Matter*, 457:296–309, 2015.
- [58] M. Stewart, M.G. Cain, and D.A. Hall. *Ferroelectric Hysteresis and Analysis*. National Physics Laboratory, 1999.
- [59] Gerd Berghold, Christopher J. Mundy, Aldo H. Romero, Jürg Hutter, and Michele Parrinello. General and efficient algorithms for obtaining maximally localized wannier functions. *Phys. Rev. B*, 61:10040–10048, Apr 2000.
- [60] Ken ichi Sakayori, Yasunori Matsui, Hiroyuki Abe, Eiji Nakamura, Mikihiko Kenmoku, Tomoyuki Hara, Daisuke Ishikawa, Akihiro Kokubu, Ken ichi Hirota, and Takuro Ikeda. Curie temperature of  $\text{Bi}_2\text{Ti}_2\text{O}_7$ . *Japanese Journal of Applied Physics*, 34(Part 1, No. 9B):5443–5445, sep 1995.
- [61] W. Cochran. Crystal stability and the theory of ferroelectricity. *Advances in Physics*, 9(36):387–423, 1960.
- [62] Paramjit Kour and Sudipta Kishore Pradhan. Perovskite ferroelectric. In Dipti Ranjan Sahu, editor, *Multifunctional Ferroelectric Materials*, chapter 3. IntechOpen, Rijeka, 2021.
- [63] T. Eshita, W. Wang, K. Nakamura, S. Mihara, H. Saito, Y. Hikosaka, K. Inoue, S. Kawashima, H. Yamaguchi, and K. Nomura. Development of ferroelectric ram (fram) for mass production. In *2014 Joint IEEE International Symposium*

- on the Applications of Ferroelectric, International Workshop on Acoustic Transduction Materials and Devices Workshop on Piezoresponse Force Microscopy*, pages 1–3, 2014.
- [64] S. L. Miller, R. D. Nasby, J. R. Schwank, M. S. Rodgers, and P. V. Dressendorfer. Device modeling of ferroelectric capacitors. *Journal of Applied Physics*, 68(12):6463–6471, 1990.
- [65] E. Sawaguchi. Photoferroelectrics by V. M. Fridkin. *Acta Crystallographica Section A*, 36(6):1091–1092, Nov 1980.
- [66] C.Y. Fong, Y. Petroff, S. Kohn, and Y.R. Shen. Wavelength modulation spectra of sbi and its electronic band structure. *Solid State Communications*, 14(8):681–685, 1974.
- [67] Riming Nie, Hyun-sung Yun, Min-Jae Paik, Aarti Mehta, Byung-wook Park, Yong Chan Choi, and Sang Il Seok. Efficient solar cells based on light-harvesting antimony sulfoiodide. *Advanced Energy Materials*, 8(7):1701901, 2018.
- [68] Keith T. Butler, Jarvist M. Frost, and Aron Walsh. Ferroelectric materials for solar energy conversion: photoferroics revisited. *Energy Environ. Sci.*, 8:838–848, 2015.
- [69] V I Belinicher and B I Sturman. The photogalvanic effect in media lacking a center of symmetry. *Soviet Physics Uspekhi*, 23(3):199–223, mar 1980.
- [70] G. Dresselhaus. Spin-orbit coupling effects in zinc blende structures. *Phys. Rev.*, 100:580–586, Oct 1955.
- [71] Jacky Even, Laurent Pedesseau, Jean-Marc Jancu, and Claudine Katan. Importance of spin–orbit coupling in hybrid organic/inorganic perovskites for photovoltaic applications. *The Journal of Physical Chemistry Letters*, 4(17):2999–3005, 2013.

- 
- [72] Ralph von Baltz and Wolfgang Kraut. Theory of the bulk photovoltaic effect in pure crystals. *Physical Review B*, 23(10):5590, 1981.
- [73] N. Ogawa, M. Sotome, Y. Kaneko, M. Ogino, and Y. Tokura. Shift current in the ferroelectric semiconductor sbsi. *Phys. Rev. B*, 96:241203, Dec 2017.
- [74] D Côté, N v Laman, and HM Van Driel. Rectification and shift currents in gaas. *Applied physics letters*, 80(6):905–907, 2002.
- [75] F. Nastos and J. E. Sipe. Optical rectification and shift currents in gaas and gap response: Below and above the band gap. *Phys. Rev. B*, 74:035201, Jul 2006.
- [76] Liang Z. Tan, Fan Zheng, Steve M. Young, Fenggong Wang, Shi Liu, and Andrew M. Rappe. Shift current bulk photovoltaic effect in polar materials—hybrid and oxide perovskites and beyond. *npj Computational Materials*, 2(1):16026, Aug 2016.
- [77] Jueli Shi, Jiaye Zhang, Lu Yang, Mei Qu, Dong-Chen Qi, and Kelvin H. L. Zhang. Wide bandgap oxide semiconductors: from materials physics to optoelectronic devices. *Advanced Materials*, 33(50):2006230, 2021.
- [78] Julien Varignon, Manuel Bibes, and Alex Zunger. Origin of band gaps in 3d perovskite oxides. *Nature Communications*, 10(1):1658, Apr 2019.
- [79] S. S. Shin, S. J. Lee, and S. I. Seok. Exploring wide bandgap metal oxides for perovskite solar cells. *APL Materials*, 7(2):022401, 2019.
- [80] J. Shieh, J.H. Yeh, Y.C. Shu, and J.H. Yen. Hysteresis behaviors of barium titanate single crystals based on the operation of multiple 90° switching systems. *Materials Science and Engineering: B*, 161(1):50 – 54, 2009. Proceedings of the joint meeting of the 2nd International Conference on the Science and Technology for Advanced Ceramics (STAC-II) and the 1st International Conference on the Science and Technology of Solid Surfaces and Interfaces (STSI-I).

- 
- [81] Keigo Suzuki and Kazunori Kijima. Optical band gap of barium titanate nanoparticles prepared by RF-plasma chemical vapor deposition. *Japanese Journal of Applied Physics*, 44(4A):2081–2082, apr 2005.
- [82] Pengcheng Xu, Dongping Chang, Tian Lu, Long Li, Minjie Li, and Wencong Lu. Search for abo<sub>3</sub> type ferroelectric perovskites with targeted multi-properties by machine learning strategies. *Journal of Chemical Information and Modeling*, Aug 2021.
- [83] Haitao Huang. Ferroelectric photovoltaics. *Nature Photonics*, 4(3):134–135, Mar 2010.
- [84] Yichong Liu, Zhuo Kang, Suicai Zhang, Yong Li, Hualin Wu, Jing Wu, Pingwei Wu, Zheng Zhang, Qingliang Liao, and Yue Zhang. Ferroelectric polarization-enhanced charge separation in a vanadium-doped zno photoelectrochemical system. *Inorg. Chem. Front.*, 5:1533–1539, 2018.
- [85] Ilya Grinberg, D. Vincent West, Maria Torres, Gaoyang Gou, David M. Stein, Liyan Wu, Guannan Chen, Eric M. Gallo, Andrew R. Akbashev, Peter K. Davies, Jonathan E. Spanier, and Andrew M. Rappe. Perovskite oxides for visible-light-absorbing ferroelectric and photovoltaic materials. *Nature*, 503(7477):509–512, Nov 2013.
- [86] Lina Li, Xitao Liu, Chao He, Sasa Wang, Chengmin Ji, Xinyuan Zhang, Zhihua Sun, Sangen Zhao, Maochun Hong, and Junhua Luo. A potential sn-based hybrid perovskite ferroelectric semiconductor. *Journal of the American Chemical Society*, 142(3):1159–1163, Jan 2020.
- [87] J. Beilsten-Edmands, G. E. Eperon, R. D. Johnson, H. J. Snaith, and P. G. Radaelli. Non-ferroelectric nature of the conductance hysteresis in ch<sub>3</sub>nh<sub>3</sub>pb<sub>3</sub> perovskite-based photovoltaic devices. *Applied Physics Letters*, 106(17):173502, 2015.

- [88] Zhen Fan, Juanxiu Xiao, Kuan Sun, Lei Chen, Yating Hu, Jianyong Ouyang, Khuong P. Ong, Kaiyang Zeng, and John Wang. Ferroelectricity of  $\text{CH}_3\text{NH}_3\text{PbI}_3$  perovskite. *The Journal of Physical Chemistry Letters*, 6(7):1155–1161, Apr 2015.
- [89] Yevgeny Rakita, Omri Bar-Elli, Elena Meirzadeh, Hadar Kaslasi, Yagel Peleg, Gary Hodes, Igor Lubomirsky, Dan Oron, David Ehre, and David Cahen. Tetragonal  $\text{CH}_3\text{NH}_3\text{PbI}_3$  is ferroelectric. *Proceedings of the National Academy of Sciences*, 114(28):E5504–E5512, 2017.
- [90] Jutta Rogal. *Stability, Composition and Function of Palladium Surfaces in Oxidizing Environments: A First-Principles Statistical Mechanics Approach*. PhD thesis, 2006.
- [91] M. Born and R. Oppenheimer. Zur quantentheorie der molekeln. *Annalen der Physik*, 389(20):457–484, 1927.
- [92] P. Hohenberg and W. Kohn. Inhomogeneous electron gas. *Phys. Rev.*, 136:B864–B871, Nov 1964.
- [93] W. Kohn and L. J. Sham. Self-consistent equations including exchange and correlation effects. *Phys. Rev.*, 140:A1133–A1138, Nov 1965.
- [94] Feliciano Giustino. *Materials modelling using density functional theory: properties and predictions*. Oxford University Press, 2014.
- [95] D. M. Ceperley and B. J. Alder. Ground state of the electron gas by a stochastic method. *Phys. Rev. Lett.*, 45:566–569, Aug 1980.
- [96] J. P. Perdew and Alex Zunger. Self-interaction correction to density-functional approximations for many-electron systems. *Phys. Rev. B*, 23:5048–5079, May 1981.
- [97] A. D. Becke. Density-functional exchange-energy approximation with correct asymptotic behavior. *Phys. Rev. A*, 38:3098–3100, Sep 1988.

- [98] Chengteh Lee, Weitao Yang, and Robert G. Parr. Development of the Colle-Salvetti correlation-energy formula into a functional of the electron density. *Phys. Rev. B*, 37:785–789, Jan 1988.
- [99] John P. Perdew. Density-functional approximation for the correlation energy of the inhomogeneous electron gas. *Phys. Rev. B*, 33:8822–8824, Jun 1986.
- [100] Ying Wang, Xinsheng Jin, Haoyu S. Yu, Donald G. Truhlar, and Xiao He. Revised m06-l functional for improved accuracy on chemical reaction barrier heights, noncovalent interactions, and solid-state physics. *Proceedings of the National Academy of Sciences*, 114(32):8487–8492, 2017.
- [101] Jianwei Sun, Martijn Marsman, Gábor I. Csonka, Adrienn Ruzsinszky, Pan Hao, Yoon-Suk Kim, Georg Kresse, and John P. Perdew. Self-consistent meta-generalized gradient approximation within the projector-augmented-wave method. *Phys. Rev. B*, 84:035117, Jul 2011.
- [102] Jianwei Sun, Adrienn Ruzsinszky, and John P. Perdew. Strongly constrained and appropriately normed semilocal density functional. *Phys. Rev. Lett.*, 115:036402, Jul 2015.
- [103] John P. Perdew, Matthias Ernzerhof, and Kieron Burke. Rationale for mixing exact exchange with density functional approximations. *The Journal of Chemical Physics*, 105(22):9982–9985, 1996.
- [104] Judith Harl, Laurids Schimka, and Georg Kresse. Assessing the quality of the random phase approximation for lattice constants and atomization energies of solids. *Phys. Rev. B*, 81:115126, Mar 2010.
- [105] Judith Harl and Georg Kresse. Accurate bulk properties from approximate many-body techniques. *Phys. Rev. Lett.*, 103:056401, Jul 2009.
- [106] Lamjed Debbichi, Songju Lee, Hyunyoung Cho, Andrew M. Rappe, Ki-Ha Hong, Min Seok Jang, and Hyungjun Kim. Mixed valence perovskite  $\text{Cs}_2\text{Au}_2\text{I}_6$ : A

- potential material for thin-film pb-free photovoltaic cells with ultrahigh efficiency. *Advanced Materials*, 30(12):1707001, Mar 2018.
- [107] Roberto Dovesi, Bartolomeo Civalleri, Carla Roetti, Victor R. Saunders, and Roberto Orlando. *Ab Initio Quantum Simulation in Solid State Chemistry*, chapter 1, pages 1–125. John Wiley & Sons, Ltd, 2005.
- [108] Yoyo Hinuma, Giovanni Pizzi, Yu Kumagai, Fumiyasu Oba, and Isao Tanaka. Band structure diagram paths based on crystallography. *Computational Materials Science*, 128:140 – 184, 2017.
- [109] Neil W. Ashcroft and N. David Mermin. *Solid state physics*. Cengage Learning, 1976.
- [110] P. E. Blöchl. Projector augmented-wave method. *Phys. Rev. B*, 50:17953–17979, Dec 1994.
- [111] Zhanyu Ning. First principles quantitative modeling of molecular devices. 01 2011.
- [112] W Pauli. Principles of wave mechanics. *Handbuch der Physik*, 24:162, 1933.
- [113] Hans Hellmann. *Einführung in die Quantenchemie*. Leipzig : F. Deuticke, 1937.
- [114] R. P. Feynman. Forces in molecules. *Phys. Rev.*, 56:340–343, Aug 1939.
- [115] Harold T. Stokes, Dorian M. Hatch, Branton J. Campbell, and David E. Tanner. Isodisplace: a web-based tool for exploring structural distortions. *Journal of Applied Crystallography*, 39(4):607–614, 2006.
- [116] Harold T. Stokes and Dorian M. Hatch. FINDSYM: program for identifying the space-group symmetry of a crystal. *Journal of Applied Crystallography*, 38(1):237–238, Feb 2005.
- [117] Dorian M. Hatch and Harold T. Stokes. INVARIANTS: program for obtaining a list of invariant polynomials of the order-parameter components associated

- with irreducible representations of a space group. *Journal of Applied Crystallography*, 36(3 Part 2):951–952, Jun 2003.
- [118] W. Zhong and David Vanderbilt. Competing structural instabilities in cubic perovskites. *Phys. Rev. Lett.*, 74:2587–2590, Mar 1995.
- [119] Ritesh Uppuluri, Hirofumi Akamatsu, Arnab Sen Gupta, Huaiyu Wang, Craig M. Brown, Kleyser E. Agueda Lopez, Nasim Alem, Venkatraman Gopalan, and Thomas E. Mallouk. Competing polar and antipolar structures in the ruddlesden–popper layered perovskite  $\text{Li}_2\text{SrNb}_2\text{O}_7$ . *Chemistry of Materials*, 31(12):4418–4425, 2019.
- [120] Astrid Marthinsen, Carina Faber, Ulrich Aschauer, Nicola A. Spaldin, and Sverre M. Selbach. Coupling and competition between ferroelectricity, magnetism, strain, and oxygen vacancies in  $\text{A}(\text{MnO})_3$  perovskites. *MRS Communications*, 6(3):182–191, 2016.
- [121] Annalise E. Maughan, Alex M. Ganose, Mohammed A. Almaker, David O. Scanlon, and James R. Neilson. Tolerance factor and cooperative tilting effects in vacancy-ordered double perovskite halides. *Chemistry of Materials*, 30(11):3909–3919, 2018.
- [122] Ulrich Aschauer and Nicola A Spaldin. Competition and cooperation between antiferrodistortive and ferroelectric instabilities in the model perovskite  $\text{SrTiO}_3$ . 26(12):122203, mar 2014.
- [123] Lamjed Debbichi, Songju Lee, Hyunyoung Cho, Andrew M. Rappe, Ki-Ha Hong, Min Seok Jang, and Hyungjun Kim. Mixed valence perovskite  $\text{Cs}_2\text{Au}_2\text{I}_6$ : A potential material for thin-film pb-free photovoltaic cells with ultrahigh efficiency. *Advanced Materials*, 30(12):1707001, 2018.
- [124] N. Matsushita, H. Kitagawa, and N. Kojima. A Three-Dimensional Iodo-Bridged Mixed-Valence Gold(I, III) Compound,  $\text{Cs}_2\text{Au}^{\text{I}}\text{Au}^{\text{III}}\text{I}_6$ . *Acta Crystallographica Section C*, 53(6):663–666, Jun 1997.

- [125] Scott C. Riggs, M.C. Shapiro, F. Corredor, T.H. Geballe, I.R. Fisher, Gregory T. McCandless, and Julia Y. Chan. Single crystal growth by self-flux method of the mixed valence gold halides  $\text{Cs}_2[\text{Au}^{\text{II}}\text{X}_2][\text{Au}^{\text{III}}\text{X}_4]$  ( $\text{X}=\text{Br}, \text{I}$ ). *Journal of Crystal Growth*, 355(1):13 – 16, 2012.
- [126] Nobuyuki Matsushita, Atsushi Tanaka, and Norimichi Kojima. A three-dimensional iodo-bridged mixed-valence gold(I,III) compound,  $\text{Rb}_2[\text{Au}^{\text{I}}\text{I}_2][\text{Au}^{\text{I}}\text{III}_4]$ . *Acta Crystallographica Section E*, 61(9):i201–i203, Sep 2005.
- [127] J. Strähle, J. Gelinek, and M. Kölmel. Über den thermischen abbau einiger alkalimetall- und ammoniumhalogenoaurate(iii) und die kristallstruktur der zersetzungsprodukte  $\text{Rb}_2\text{Au}_2\text{Br}_6$ ,  $\text{Rb}_3\text{Au}_3\text{Cl}_8$  und  $\text{Au}(\text{NH}_3)\text{Cl}_3$ . *Zeitschrift für anorganische und allgemeine Chemie*, 456(1):241–260, 1979.
- [128] Joachim Strähle, Jürgen Gelinek, Marianne Kölmel, and Anna-Maria Nemecek. Die kristallstruktur der salze  $\text{K}_2\text{Au}_2\text{I}_6$  und  $\text{Cs}_2\text{AgXaui1-xauiiibr6}$ . ein beitrag zur kristallchemie der alkalihexahalogenoaurate(i,iii) / crystal structure of the salts  $\text{K}_2\text{Au}_2\text{I}_6$  and  $\text{Cs}_2\text{AgXaui1-xauiiibr6}$ . a contribution to the crystal chemistry of the alkali hexahalogeno aurates(i,iii). *Zeitschrift für Naturforschung B*, 34(8), 1979.
- [129] Alain Mercy, Jordan Bieder, Jorge Íñiguez, and Philippe Ghosez. Structurally triggered metal-insulator transition in rare-earth nickelates. *Nature Communications*, 8(1):1677, Nov 2017.
- [130] G. Kresse and J. Hafner. Ab initio molecular dynamics for liquid metals. *Phys. Rev. B*, 47:558–561, Jan 1993.
- [131] G. Kresse and J. Hafner. Ab initio molecular-dynamics simulation of the liquid-metal–amorphous–semiconductor transition in germanium. *Phys. Rev. B*, 49:14251–14269, May 1994.

- [132] G. Kresse and J. Furthmüller. Efficiency of ab-initio total energy calculations for metals and semiconductors using a plane-wave basis set. *Computational Materials Science*, 6(1):15 – 50, 1996.
- [133] G. Kresse and J. Furthmüller. Efficient iterative schemes for ab initio total-energy calculations using a plane-wave basis set. *Phys. Rev. B*, 54:11169–11186, Oct 1996.
- [134] G. Kresse and D. Joubert. From ultrasoft pseudopotentials to the projector augmented-wave method. *Phys. Rev. B*, 59:1758–1775, Jan 1999.
- [135] John P. Perdew, Adrienn Ruzsinszky, Gábor I. Csonka, Oleg A. Vydrov, Gustavo E. Scuseria, Lucian A. Constantin, Xiaolan Zhou, and Kieron Burke. Restoring the density-gradient expansion for exchange in solids and surfaces. *Phys. Rev. Lett.*, 100:136406, Apr 2008.
- [136] Hendrik J. Monkhorst and James D. Pack. Special points for brillouin-zone integrations. *Phys. Rev. B*, 13:5188–5192, Jun 1976.
- [137] Danel Orobengoa, Cesar Capillas, Mois I. Aroyo, and J. Manuel Perez-Mato. AMPLIMODES: symmetry-mode analysis on the Bilbao Crystallographic Server. *Journal of Applied Crystallography*, 42(5):820–833, Oct 2009.
- [138] J. M. Perez-Mato, D. Orobengoa, and M. I. Aroyo. Mode crystallography of distorted structures. *Acta Crystallographica Section A*, 66(5):558–590, Sep 2010.
- [139] Branton J. Campbell, Harold T. Stokes, David E. Tanner, and Dorian M. Hatch. ISODISPLACE: a web-based tool for exploring structural distortions. *Journal of Applied Crystallography*, 39(4):607–614, Aug 2006.
- [140] Stefano Baroni, Paolo Giannozzi, and Andrea Testa. Green’s-function approach to linear response in solids. *Phys. Rev. Lett.*, 58:1861–1864, May 1987.

- [141] Alex M. Ganose, Adam J. Jackson, and David O. Scanlon. sumo: Command-line tools for plotting and analysis of periodic \*ab initio\* calculations. *Journal of Open Source Software*, 3(28):717, 2018.
- [142] Melvin J. Lax. *Symmetry principles in solid state and molecular physics*. Dover Publications, Inc., 2001.
- [143] Francis Birch. Finite elastic strain of cubic crystals. *Phys. Rev.*, 71:809–824, Jun 1947.
- [144] F. D. Murnaghan. The compressibility of media under extreme pressures. *Proceedings of the National Academy of Sciences*, 30(9):244–247, 1944.
- [145] Craig J. Fennie and Karin M. Rabe. Ferroelectric transition in  $\text{YMnO}_3$  from first principles. *Phys. Rev. B*, 72:100103, Sep 2005.
- [146] Qing Zhang, Qiuyu Shang, Rui Su, T. Thu Ha Do, and Qihua Xiong. Halide perovskite semiconductor lasers: Materials, cavity design, and low threshold. *Nano Letters*, 21(5):1903–1914, 2021. PMID: 33435686.
- [147] Wei Li, Yalun Xu, Jiali Peng, Ruiming Li, Jiannan Song, Huihuang Huang, Li-hao Cui, and Qianqian Lin. Evaporated perovskite thick junctions for x-ray detection. *ACS Applied Materials & Interfaces*, 13(2):2971–2978, 2021. PMID: 33399446.
- [148] Aozhen Xie, Chathuranga Hettiarachchi, Francesco Maddalena, Marcin E. Witkowski, Michał Makowski, Winicjusz Drozdowski, Arramel Arramel, Andrew T. S. Wee, Stuart Victor Springham, Phan Quoc Vuong, Hong Joo Kim, Christophe Dujardin, Philippe Coquet, Muhammad Danang Birowosuto, and Cuong Dang. Lithium-doped two-dimensional perovskite scintillator for wide-range radiation detection. *Communications Materials*, 1(1):37, Jun 2020.
- [149] Minh Tam Hoang, Ngoc Duy Pham, Ji Hun Han, James M. Gardner, and Ilwhan Oh. Integrated photoelectrolysis of water implemented on organic metal halide

- perovskite photoelectrode. *ACS Applied Materials & Interfaces*, 8(19):11904–11909, 2016. PMID: 27120406.
- [150] Joseph S. Manser, Jeffrey A. Christians, and Prashant V. Kamat. Intriguing optoelectronic properties of metal halide perovskites. *Chemical Reviews*, 116(21):12956–13008, Nov 2016.
- [151] Tim Hellmann, Chittaranjan Das, Tobias Abzieher, Jonas A. Schwenzler, Michael Wussler, Ralph Dachauer, Ulrich W. Paetzold, Wolfram Jaegermann, and Thomas Mayer. The electronic structure of mapi-based perovskite solar cells: Detailed band diagram determination by photoemission spectroscopy comparing classical and inverted device stacks. *Advanced Energy Materials*, 10(42):2002129, Nov 2020.
- [152] Lucy D. Whalley, Jarvist M. Frost, Benjamin J. Morgan, and Aron Walsh. Impact of nonparabolic electronic band structure on the optical and transport properties of photovoltaic materials. *Phys. Rev. B*, 99:085207, Feb 2019.
- [153] Alex M. Ganose, Christopher N. Savory, and David O. Scanlon. Beyond methylammonium lead iodide: prospects for the emergent field of ns<sub>2</sub> containing solar absorbers. *Chem. Commun.*, 53:20–44, 2017.
- [154] Pina Pitriana, Triati Dewi Kencana Wungu, Herman, and Rahmat Hidayat. The characteristics of band structures and crystal binding in all-inorganic perovskite apbbr<sub>3</sub> studied by the first principle calculations using the density functional theory (dft) method. *Results in Physics*, 15:102592, Dec 2019.
- [155] Zihao Fu, Xuning Zhang, Hong Zhang, Yanxun Li, Huiqiong Zhou, and Yuan Zhang. On the understandings of dielectric constant and its impacts on the photovoltaic efficiency in organic solar cells. *Chinese Journal of Chemistry*, 39(2):381–390, Feb 2021.
- [156] Emilio J. Juarez-Perez, Rafael S. Sanchez, Laura Badia, Germá Garcia-Belmonte, Yong Soo Kang, Ivan Mora-Sero, and Juan Bisquert. Photoinduced giant di-

- electric constant in lead halide perovskite solar cells. *The Journal of Physical Chemistry Letters*, 5(13):2390–2394, Jul 2014.
- [157] Yuxuan Lin, Xi Ling, Lili Yu, Shengxi Huang, Allen L. Hsu, Yi-Hsien Lee, Jing Kong, Mildred S. Dresselhaus, and Tomás Palacios. Dielectric screening of excitons and trions in single-layer mos<sub>2</sub>. *Nano Letters*, 14(10):5569–5576, Oct 2014.
- [158] Manjari Jain, Deepika Gill, Preeti Bhumla, Pooja Basera, and Saswata Bhattacharya. Theoretical insights to excitonic effect in lead bromide perovskites. *Applied Physics Letters*, 118(19):192103, 2021.
- [159] M. A. Subramanian and A. W. Sleight.  $\text{Acu}_3\text{Ti}_4\text{O}_{12}$  and  $\text{acu}_3\text{Ru}_4\text{O}_{12}$  perovskites: high dielectric constants and valence degeneracy. *Solid State Sciences*, 4(3):347–351, Mar 2002.
- [160] E. Antolín, A. Martí, and A. Luque. 1.29 - *Intermediate Band Solar Cells*, pages 619–639. Elsevier, Oxford, Jan 2012.
- [161] Han Gyeol Lee, Rokyeon Kim, Jinkwon Kim, Minu Kim, Tae Heon Kim, Shinbuhm Lee, and Tae Won Noh. Anisotropic suppression of octahedral breathing distortion with the fully strained  $\text{BaBiO}_3/\text{BaCeO}_3$  heterointerface. *APL Materials*, 6(1):016107, 2018.
- [162] John W. Freeland, Michel van Veenendaal, and Jak Chakhalian. Evolution of electronic structure across the rare-earth  $\text{RnIO}_3$  series. *Journal of Electron Spectroscopy and Related Phenomena*, 208:56–62, 2016. Special Issue: Electronic structure and function from state-of-the-art spectroscopy and theory.
- [163] Ganesh Kotnana and S. Narayana Jammalamadaka. Band gap tuning and orbital mediated electron–phonon coupling in  $\text{HoFe}_2\text{Cr}_2\text{O}_7$  (0 x 1). *Journal of Applied Physics*, 118(12):124101, Sep 2015.
- [164] N. O. Lipari, J. Bernholc, and S. T. Pantelides. Electronic structure of the jahn-teller distorted vacancy in silicon. *Phys. Rev. Lett.*, 43:1354–1357, Oct 1979.

- [165] R. Franz and H. Werheit. Influence of the jahn-teller effect on the electronic band structure of boron-rich solids containing b<sub>12</sub> icosahedra. *AIP Conference Proceedings*, 231(1):29–36, Jul 1991.
- [166] R Franz and H Werheit. Jahn-teller effect of the b<sub>sub12</sub>/sub icosahedron and its general influence on the valence band structures of boron-rich solids. *Europhysics Letters (EPL)*, 9(2):145–150, may 1989.
- [167] Soham Mukherjee, Dibya Phuyal, Carlo U. Segre, Shyamashis Das, Olof Karis, Tomas Edvinsson, and Håkan Rensmo. Structure and electronic effects from mn and nb co-doping for low band gap batio<sub>3</sub> ferroelectrics. *The Journal of Physical Chemistry C*, 125(27):14910–14923, 2021.
- [168] X. J. Liu, K. Matsuda, Y. Moritomo, A. Nakamura, and N. Kojima. Electronic structure of the gold complexes cs<sub>2</sub>au<sub>2</sub>X<sub>6</sub> (x=i, br, and cl). *Phys. Rev. B*, 59:7925–7930, Mar 1999.
- [169] Rohit Prasanna, Aryeh Gold-Parker, Tomas Leijtens, Bert Conings, Aslihan Babayigit, Hans-Gerd Boyen, Michael F. Toney, and Michael D. McGehee. Band gap tuning via lattice contraction and octahedral tilting in perovskite materials for photovoltaics. *Journal of the American Chemical Society*, 139(32):11117–11124, 2017. PMID: 28704048.
- [170] Mauro Coduri, Timothy A. Strobel, Marek Szafranski, Andrzej Katrusiak, Arup Mahata, Federico Cova, Sara Bonomi, Edoardo Mosconi, Filippo De Angelis, and Lorenzo Malavasi. Band gap engineering in masnbr<sub>3</sub> and cssnbr<sub>3</sub> perovskites: Mechanistic insights through the application of pressure. *The Journal of Physical Chemistry Letters*, 10(23):7398–7405, 2019. PMID: 31721591.
- [171] Anna Amat, Edoardo Mosconi, Enrico Ronca, Claudio Quarti, Paolo Umari, Md. K. Nazeeruddin, Michael Grätzel, and Filippo De Angelis. Cation-induced band-gap tuning in organohalide perovskites: Interplay of spin–orbit coupling and octahedra tilting. *Nano Letters*, 14(6):3608–3616, Jun 2014.

- [172] Annalise E. Maughan, Alex M. Ganose, Mohammed A. Almaker, David O. Scanlon, and James R. Neilson. Tolerance factor and cooperative tilting effects in vacancy-ordered double perovskite halides. *Chemistry of Materials*, 30(11):3909–3919, Jun 2018.
- [173] Robert W. Keyes. Correlation between mobility and effective mass in semiconductors. *Journal of Applied Physics*, 30(3):454–454, Mar 1959.
- [174] Jing Feng and Bing Xiao. Effective masses and electronic and optical properties of nontoxic  $\text{MASnX}_3$  ( $x = \text{Cl, Br, and I}$ ) perovskite structures as solar cell absorber: A theoretical study using HSE06. *The Journal of Physical Chemistry C*, 118(34):19655–19660, Aug 2014.
- [175] Joachim Strähle, Jürgen Gelinek, Marianne Kölmel, and Anna-Maria Nemecek. Die kristallstruktur der salze  $\text{K}_2\text{Au}_2\text{I}_6$  und  $\text{Cs}_2\text{AgXaui1-xauiibr6}$ . ein beitrag zur kristallchemie der alkalihexahalogenoaurate(i,iii) / crystal structure of the salts  $\text{K}_2\text{Au}_2\text{I}_6$  and  $\text{Cs}_2\text{AgXaui1-xauiibr6}$ . a contribution to the crystal chemistry of the alkali hexahalogeno aurates(i,iii). *Zeitschrift für Naturforschung B*, 34(8):1047–1052, 1979.
- [176] Xi Zhu, Haibin Su, Rudolph A. Marcus, and Maria E. Michel-Beyerle. Computed and experimental absorption spectra of the perovskite  $\text{CH}_3\text{NH}_3\text{PbI}_3$ . *The Journal of Physical Chemistry Letters*, 5(17):3061–3065, Sep 2014.
- [177] Anna F. Kusmartseva, Minghui Yang, Angel M. Arevalo-Lopez, Konstantin V. Kamenev, and J. Paul Attfield. Pressure suppression of charge order without metallisation in  $\text{Cs}_2\text{Au}_2\text{I}_6$ . *Chem. Commun.*, 46:6681–6683, 2010.
- [178] Shibing Wang, Shigeto Hirai, Max C. Shapiro, Scott C. Riggs, Ted H. Geballe, Wendy L. Mao, and Ian R. Fisher. Pressure-induced symmetry breaking in tetragonal  $\text{CsAuI}_3$ . *Phys. Rev. B*, 87:054104, Feb 2013.

- [179] N. Kojima and N. Matsushita. P-t phase diagram and au valence state of the perovskite-type au mixed-valence complexes  $m_2[\text{auix}_2][\text{auiix}_4]$  ( $m=k, \text{rb}, \text{cs}; x=\text{cl}, \text{br}, \text{i}$ ). *Coordination Chemistry Reviews*, 198(1):251–263, Mar 2000.
- [180] Fernando Aguado, Fernando Rodríguez, Rafael Valiente, Jean-Paul Itié, and Michael Hanfland. Pressure effects on jahn-teller distortion in perovskites: The roles of local and bulk compressibilities. *Phys. Rev. B*, 85:100101, Mar 2012.
- [181] P. Bouvier and J. Kreisel. Pressure-induced phase transition in  $\text{LaAlO}_3$ . *Journal of Physics: Condensed Matter*, 14(15):3981–3991, Apr 2002.
- [182] Dong Zhao, Thomas Lenz, Gerwin H. Gelinck, Pim Groen, Dragan Damjanovic, Dago M. de Leeuw, and Ilias Katsouras. Depolarization of multidomain ferroelectric materials. *Nature Communications*, 10(1):2547, Jun 2019.
- [183] R. R. Mehta, B. D. Silverman, and J. T. Jacobs. Depolarization fields in thin ferroelectric films. *Journal of Applied Physics*, 44(8):3379–3385, 1973.
- [184] Yongbo Yuan, Zhengguo Xiao, Bin Yang, and Jinsong Huang. Arising applications of ferroelectric materials in photovoltaic devices. *J. Mater. Chem. A*, 2:6027–6041, 2014.
- [185] A. M. Glass, D. von der Linde, and T. J. Negran. High-voltage bulk photovoltaic effect and the photorefractive process in  $\text{LiNbO}_3$ . *Applied Physics Letters*, 25(4):233–235, 1974.
- [186] S. R. Basu, L. W. Martin, Y. H. Chu, M. Gajek, R. Ramesh, R. C. Rai, X. Xu, and J. L. Musfeldt. Photoconductivity in  $\text{BiFeO}_3$  thin films. *Applied Physics Letters*, 92(9):091905, 2008.
- [187] Haijuan Zhang, Zejiao Shi, Laigui Hu, Yuan-Yuan Tang, Zhengyuan Qin, Wei-Qiang Liao, Zi Shuai Wang, Jiajun Qin, Xiaoguo Li, Haoliang Wang, Meenakshi

- Gusain, Fengcai Liu, Yiyi Pan, Mingsheng Xu, Jiao Wang, Ran Liu, Chunfeng Zhang, Ren-Gen Xiong, Wei E. I. Sha, and Yiqiang Zhan. Highly efficient 1d/3d ferroelectric perovskite solar cell. *Advanced Functional Materials*, 31(27):2100205, 2021.
- [188] Cai Jin, Wanrong Geng, Linjing Wang, Wenqiao Han, Dongfeng Zheng, Songbai Hu, Mao Ye, Zedong Xu, Yanjiang Ji, Jiali Zhao, Zuhuang Chen, Gan Wang, Yunlong Tang, Yinlian Zhu, Xiuliang Ma, and Lang Chen. Tuning ferroelectricity and ferromagnetism in bifeo<sub>3</sub>/bimno<sub>3</sub> superlattices. *Nanoscale*, 12:9810–9816, 2020.
- [189] Brendan J. Kennedy, Qingdi Zhou, and Maxim Avdeev. The ferroelectric phase of cdtio<sub>3</sub>: A powder neutron diffraction study. *Journal of Solid State Chemistry*, 184(11):2987–2993, 2011.
- [190] Desheng Fu, Mitsuru Itoh, and Shin-ya Koshihara. Dielectric, ferroelectric, and piezoelectric behaviors of agnbo<sub>3</sub>–knbo<sub>3</sub> solid solution. *Journal of Applied Physics*, 106(10):104104, 2009.
- [191] A. V. Turik and A. G. Khasabov. On the origin of ferroelectricity in pbtio<sub>3</sub>. *Ferroelectrics*, 237(1):65–71, 2000.
- [192] Tobias Leonhard, Holger Röhm, Fabian J. Altermann, Michael J. Hoffmann, and Alexander Colsmann. Evolution of ferroelectric domains in methylammonium lead iodide and correlation with the performance of perovskite solar cells. *J. Mater. Chem. A*, 9:21845–21858, 2021.
- [193] R. Nechache, C. Harnagea, S. Li, L. Cardenas, W. Huang, J. Chakrabartty, and F. Rosei. Bandgap tuning of multiferroic oxide solar cells. *Nature Photonics*, 9(1):61–67, Jan 2015.
- [194] Chao Liang, Hao Gu, Yingdong Xia, Zhuo Wang, Xiaotao Liu, Junmin Xia, Shouwei Zuo, Yue Hu, Xingyu Gao, Wei Hui, Lingfeng Chao, Tingting Niu, Min Fang, Hui Lu, Han Dong, Hui Yu, Shi Chen, Xueqin Ran, Lin Song, Bixin Li, Jing

- Zhang, Yong Peng, Guosheng Shao, Jianpu Wang, Yonghua Chen, Guichuan Xing, and Wei Huang. Two-dimensional ruddlesden–popper layered perovskite solar cells based on phase-pure thin films. *Nature Energy*, 6(1):38–45, Jan 2021.
- [195] Hui Ren, Shidong Yu, Lingfeng Chao, Yingdong Xia, Yuanhui Sun, Shouwei Zuo, Fan Li, Tingting Niu, Yingguo Yang, Huanxin Ju, Bixin Li, Haiyan Du, Xingyu Gao, Jing Zhang, Jianpu Wang, Lijun Zhang, Yonghua Chen, and Wei Huang. Efficient and stable ruddlesden–popper perovskite solar cell with tailored interlayer molecular interaction. *Nature Photonics*, 14(3):154–163, Mar 2020.
- [196] Jeffrey A. Christians, Philip Schulz, Jonathan S. Tinkham, Tracy H. Schloemer, Steven P. Harvey, Bertrand J. Tremolet de Villers, Alan Sellinger, Joseph J. Berry, and Joseph M. Luther. Tailored interfaces of unencapsulated perovskite solar cells for >1,000 hour operational stability. *Nature Energy*, 3(1):68–74, Jan 2018.
- [197] Hsinhan Tsai, Wanyi Nie, Jean-Christophe Blancon, Constantinos C. Stoumpos, Reza Asadpour, Boris Harutyunyan, Amanda J. Neukirch, Rafael Verduzco, Jared J. Crochet, Sergei Tretiak, Laurent Pedesseau, Jacky Even, Muhammad A. Alam, Gautam Gupta, Jun Lou, Pulickel M. Ajayan, Michael J. Bedzyk, Mercouri G. Kanatzidis, and Aditya D. Mohite. High-efficiency two-dimensional ruddlesden–popper perovskite solar cells. *Nature*, 536(7616):312–316, Aug 2016.
- [198] Chao Liang, Dandan Zhao, Yan Li, Xiaojun Li, Shaomin Peng, Guosheng Shao, and Guichuan Xing. Ruddlesden–popper perovskite for stable solar cells. *ENERGY & ENVIRONMENTAL MATERIALS*, 1(4):221–231, 2018.
- [199] Xu Zhang, Rahim Munir, Zhuo Xu, Yucheng Liu, Hsinhan Tsai, Wanyi Nie, Jianbo Li, Tianqi Niu, Detlef-M. Smilgies, Mercouri G. Kanatzidis, Aditya D. Mohite, Kui Zhao, Aram Amassian, and Shengzhong (Frank) Liu. Phase transition control for high performance ruddlesden–popper perovskite solar cells. *Advanced Materials*, 30(21):1707166, 2018.

- [200] M. Nakamura, S. Horiuchi, F. Kagawa, N. Ogawa, T. Kurumaji, Y. Tokura, and M. Kawasaki. Shift current photovoltaic effect in a ferroelectric charge-transfer complex. *Nature Communications*, 8(1):281, Aug 2017.
- [201] Steve M. Young and Andrew M. Rappe. First principles calculation of the shift current photovoltaic effect in ferroelectrics. *Phys. Rev. Lett.*, 109:116601, Sep 2012.
- [202] Weichuan Zhang, Maochun Hong, and Junhua Luo. Halide double perovskite ferroelectrics. *Angewandte Chemie International Edition*, 59(24):9305–9308, 2020.
- [203] Yue Li, Jun Fu, Xiaoyu Mao, Chen Chen, Heng Liu, Ming Gong, and Hualing Zeng. Enhanced bulk photovoltaic effect in two-dimensional ferroelectric  $\text{CuInP}_2\text{S}_6$ . *Nature Communications*, 12(1):5896, Oct 2021.
- [204] Maxime Markov, Louis Alaerts, Henrique Pereira Coutada Miranda, Guido Petretto, Wei Chen, Janine George, Eric Bousquet, Philippe Ghosez, Gian-Marco Rignanese, and Geoffroy Hautier. Ferroelectricity and multiferroicity in anti-ruddlesden–popper structures. *Proceedings of the National Academy of Sciences*, 118(17), 2021.
- [205] Wenxiu Gao, Yi Zhu, Yaojin Wang, Guoliang Yuan, and Jun-Ming Liu. A review of flexible perovskite oxide ferroelectric films and their application. *Journal of Materiomics*, 6(1):1–16, 2020.
- [206] Jiangang He, Cesare Franchini, and James M. Rondinelli. Ferroelectric oxides with strong visible-light absorption from charge ordering. *Chemistry of Materials*, 29(6):2445–2451, 2017.
- [207] Daniel B. Straus, Shu Guo, AM Milinda Abeykoon, and Robert J. Cava. Understanding the instability of the halide perovskite  $\text{CsPbI}_3$  through temperature-dependent structural analysis. *Advanced Materials*, 32(32):2001069, 2020.

- [208] Maham M. S. Karim, Alex M. Ganose, Laura Pieters, W. W. Winnie Leung, Jessica Wade, Lina Zhang, David O. Scanlon, and Robert G. Palgrave. Anion distribution, structural distortion, and symmetry-driven optical band gap bowing in mixed halide  $\text{Cs}_2\text{SnX}_6$  vacancy ordered double perovskites. *Chemistry of Materials*, 31(22):9430–9444, 2019. PMID: 32116409.
- [209] Rossella Chiara, Marta Morana, and Lorenzo Malavasi. Germanium-based halide perovskites: Materials, properties, and applications. *ChemPlusChem*, 86(6):879–888, 2021.
- [210] Pedro Borlido, Jonathan Schmidt, Ahmad W. Huran, Fabien Tran, Miguel A. L. Marques, and Silvana Botti. Exchange-correlation functionals for band gaps of solids: benchmark, reparametrization and machine learning. *npj Computational Materials*, 6(1):96, Jul 2020.
- [211] Pragya Verma and Donald G. Truhlar. Hle16: A local kohn–sham gradient approximation with good performance for semiconductor band gaps and molecular excitation energies. *The Journal of Physical Chemistry Letters*, 8(2):380–387, Jan 2017.



A

The Structural Complexity of  
Gold Halide Double Perovskites

APPENDIX

## A.1 $\text{Rb}_2\text{Au}_2\text{I}_6$ Phonons

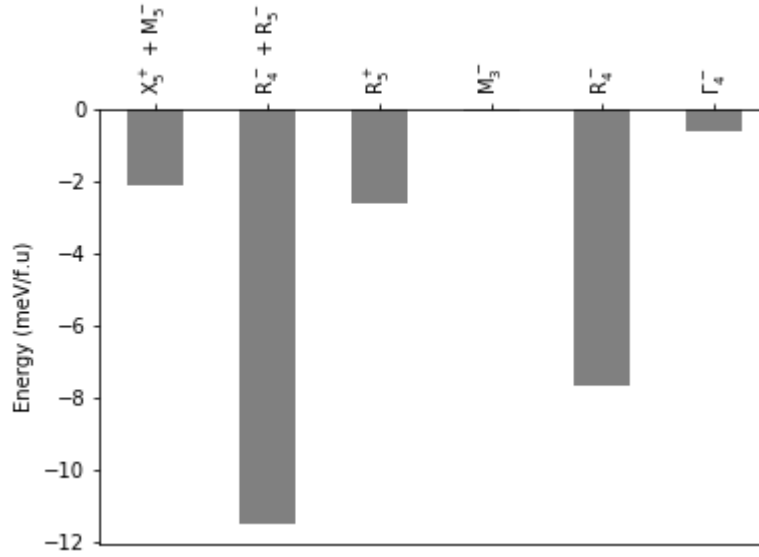


Figure A.1: The combination of both the  $R_5^-$  and  $R_4^-$  distortions contribute the largest energy gain out of each of the phonon instabilities.

## A.2 Full INVARIANTS Analysis of Structures

$\text{Pm}\bar{3}\text{m} \rightarrow \text{I4}/\text{mmm}$

$$\begin{aligned}
 F = & \frac{1}{2}A_0(R_2^-)^2 + \frac{1}{4}B_0(R_2^-)^4 \\
 & + \frac{1}{2}A_1(R_3^-)^2 + \frac{1}{4}B_1(R_3^-)^4 \\
 & - C_{01}(R_3^-)^3(R_2^-) + A_{10}(R_3^-)^2(R_2^-)^2
 \end{aligned} \tag{A.2.1}$$

**Pm $\bar{3}$ m  $\rightarrow$  C2/m**

$$\begin{aligned}
 (F - F_0) = & + a_1(T - T_1)Q_{R_{2-}}^2 + b_1Q_{R_{2-}}^4 \\
 & + a_2(T - T_2)Q_{R_{3-}}^2 + b_2Q_{R_{3-}}^4 \\
 & + a_3(T - T_3)Q_{R_{4-}}^2 + b_3Q_{R_{4-}}^4 \\
 & + a_4(T - T_4)Q_{R_{5-}}^2 + b_4Q_{R_{5-}}^4 \\
 & + \gamma_{12}Q_{R_{2-}}^2 Q_{R_{3-}}^2 + \gamma_{13}Q_{R_{2-}}^2 Q_{R_{4-}}^2 + \gamma_{14}Q_{R_{2-}}^2 Q_{R_{5-}}^2 \\
 & + \gamma_{23}Q_{R_{3-}}^2 Q_{R_{4-}}^2 + \gamma_{24}Q_{R_{3-}}^2 Q_{R_{5-}}^2 \\
 & + \gamma_{1,2}Q_{R_{2-}} Q_{R_{3-}}^3 \\
 & + (\gamma_{3(a),(b),4}Q_{R_{4-(a)}}^3 Q_{R_{5-}} - Q_{R_{4-(a)}} Q_{R_{4-(b)}}^2 Q_{R_{5-}}) + \gamma_{3,4}Q_{R_{4-(a)}} Q_{R_{5-}} \\
 & + \boxed{-C_{123(c),4}Q_{R_{2-}} Q_{R_{3-}} Q_{R_{4-(a)}} Q_{R_{5-}}} + \boxed{-C_{23(c,d),4}Q_{R_{3-}} Q_{R_{4-(a)}} Q_{R_{4-(b)}} Q_{R_{5-}}} \quad (A.2.2)
 \end{aligned}$$

**Pm $\bar{3}$ m  $\rightarrow$  P2 $_1$ /c**

$$\begin{aligned}
 (F - F_0) = & + a_1(T - T_1)Q_{R_{2-}}^2 + b_1Q_{R_{2-}}^4 \\
 & + a_2(T - T_2)Q_{R_{3-}}^2 + b_2Q_{R_{3-}}^4 \\
 & + a_3(T - T_3)Q_{R_{4-}}^2 + b_3Q_{R_{4-}}^4 \\
 & + a_4(T - T_4)Q_{R_{5-}}^2 + b_4Q_{R_{5-}}^4 \\
 & + a_5(T - T_4)Q_{X_{5+}}^2 + b_5Q_{X_{5+}}^4 \\
 & + a_6(T - T_4)Q_{M_{5+}}^2 + b_6Q_{M_{5+}}^4 \\
 & + \gamma_{1,2}Q_{R_{2-}} Q_{R_{3-(a)}}^3 \\
 & + \boxed{C_{5,6,6}Q_{M_{5+}} Q_{X_{5+(a)}} Q_{X_{5+(b)}}} \\
 & + \boxed{C_{1,2,3,4}Q_{R_{2-}} Q_{R_{3-(b)}} Q_{R_{4-}} Q_{R_{5-}} + C_{2,2,3,4}Q_{R_{3-(a)}} Q_{R_{3-(b)}} Q_{R_{4-}} Q_{R_{5-}}} \\
 & + \boxed{C_{1,3,6,6}Q_{R_{2-}} Q_{R_{4-}} Q_{M_{5+(a)}} Q_{M_{5+(b)}}} \quad (A.2.3)
 \end{aligned}$$

**$Pm\bar{3}m \rightarrow I4mm$  (Strain Induced Mechanism)**

$$\begin{aligned}
 (F - F_0) = & + a_1(T - T_1)Q_{\Gamma_{1+}}^2 + b_1Q_{\Gamma_{1+}}^4 \\
 & + a_2(T - T_2)Q_{\Gamma_{3+}}^2 + b_2Q_{\Gamma_{3+}}^4 \\
 & + a_3(T - T_3)Q_{\Gamma_{4-}}^2 + b_3Q_{\Gamma_{4-}}^4 \\
 & + a_4(T - T_4)Q_{R_{3-}}^2 + b_4Q_{R_{3-}}^4 \\
 & + \gamma_{13}Q_{\Gamma_{1+}}Q_{\Gamma_{4-}}^2 + \gamma_{23}Q_{\Gamma_{3+}}Q_{\Gamma_{4-}}^2 + \gamma_{14}Q_{\Gamma_{1+}}Q_{R_{3-}}^2 + \gamma_{23}Q_{\Gamma_{3+}}Q_{R_{3-}}^2
 \end{aligned} \tag{A.2.4}$$

 **$Pm\bar{3}m \rightarrow I4mm$  (Improper Mechanism)**

$$\begin{aligned}
 (F - F_0) = & Q_{\Gamma_4^-}^2 + Q_{\Gamma_4^-}^4 \\
 & + Q_{R_2^-}^2 + Q_{R_2^-}^4 \\
 & + Q_{R_3^-}^2 + Q_{R_3^-}^4 \\
 & + Q_{R_5^+}^2 + Q_{R_5^+}^4 \\
 & + Q_{R_3^-}^3 Q_{R_2^-} + Q_{\Gamma_4^-}^2 Q_{R_2^-}^2 + Q_{\Gamma_4^-}^2 Q_{R_3^-}^2 + Q_{\Gamma_4^-}^2 Q_{R_5^+}^2 \\
 & + Q_{R_2^-}^2 Q_{R_3^-}^2 + Q_{R_2^-}^2 Q_{R_5^+}^2 + Q_{R_3^-}^2 Q_{R_5^+}^2 \\
 & + Q_{\Gamma_4^-}^2 Q_{R_2^-} Q_{R_3^-} + Q_{R_2^-} Q_{R_3^-} Q_{R_5^+}^2 \\
 & + Q_{\Gamma_4^-} Q_{R_2^-} Q_{R_5^+} + Q_{\Gamma_4^-} Q_{R_3^-} Q_{R_5^+}
 \end{aligned} \tag{A.2.5}$$

**B**

**Tuning the Optoelectronic and  
Dielectric Properties of Gold  
Double Perovskites APPENDIX**

### B.1 Electronic Density of States: $\text{Rb}_2\text{Au}_2\text{I}_6$

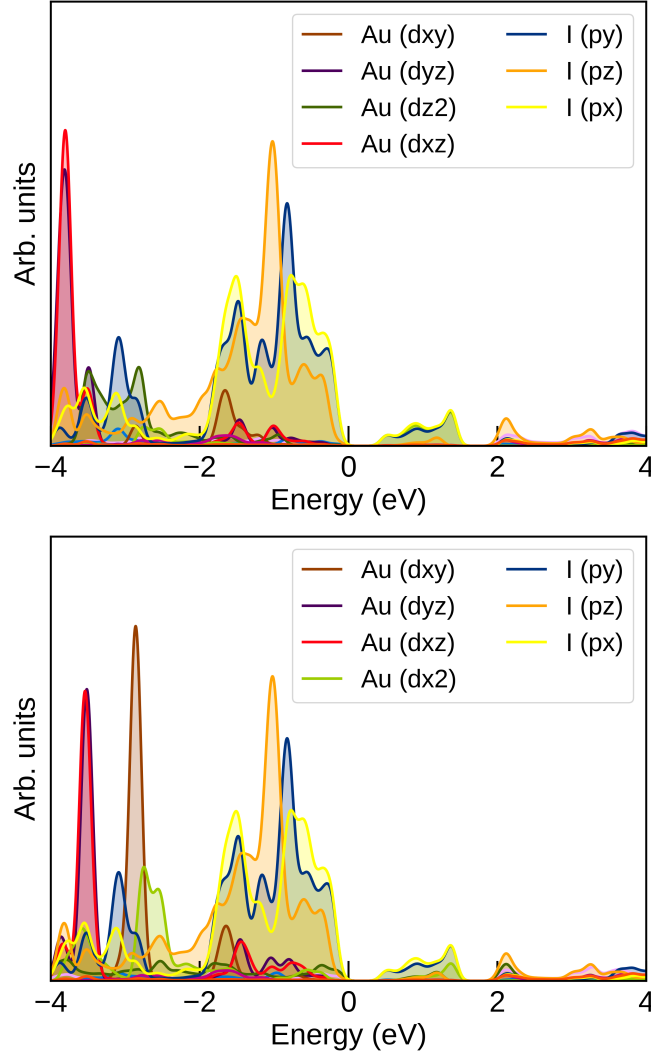


Figure B.1: Density of states of the  $\text{Rb}_2\text{Au}_2\text{I}_6$  I4/mmm structure. The top figure includes the Gold atoms in which their electrons sit within the  $d_{z^2}$  orbital and the bottom figure includes the gold atom where the electrons sit within the  $d_{x^2-y^2}$  orbital.

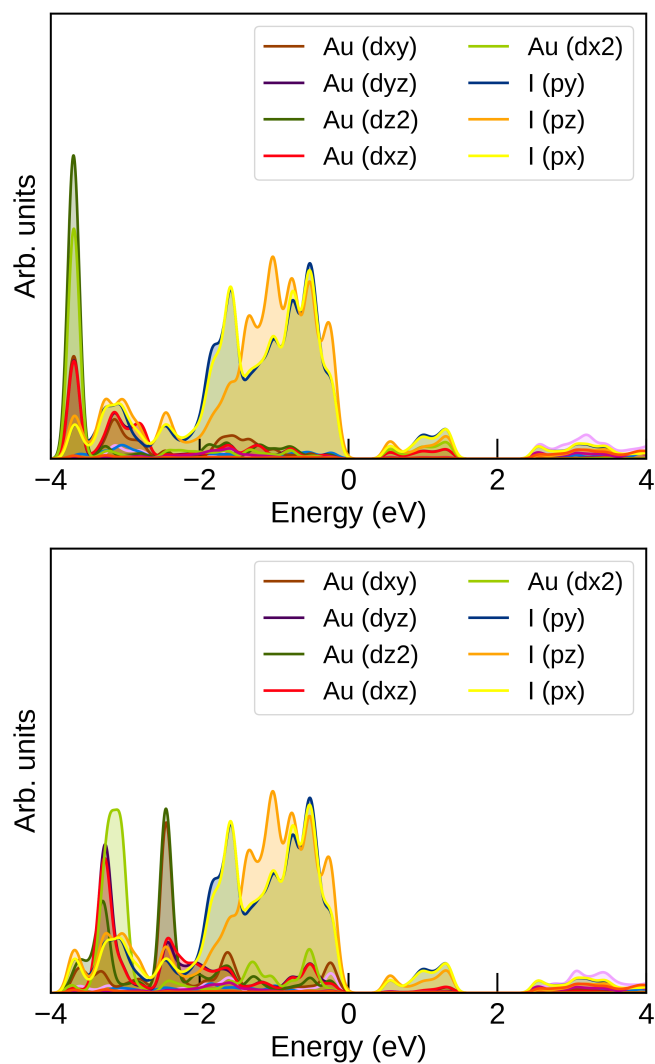


Figure B.2: Density of states of the  $\text{Rb}_2\text{Au}_2\text{I}_6$   $C2/m$  structure. The top figure includes the Gold atoms in which there electrons sit within the  $d_{z^2}$  orbital and bottom figure includes the gold atom where the electrons sit within the  $d_{x^2-y^2}$  orbital.

## B.2 Electronic Density of States: $\text{K}_2\text{Au}_2\text{I}_6$

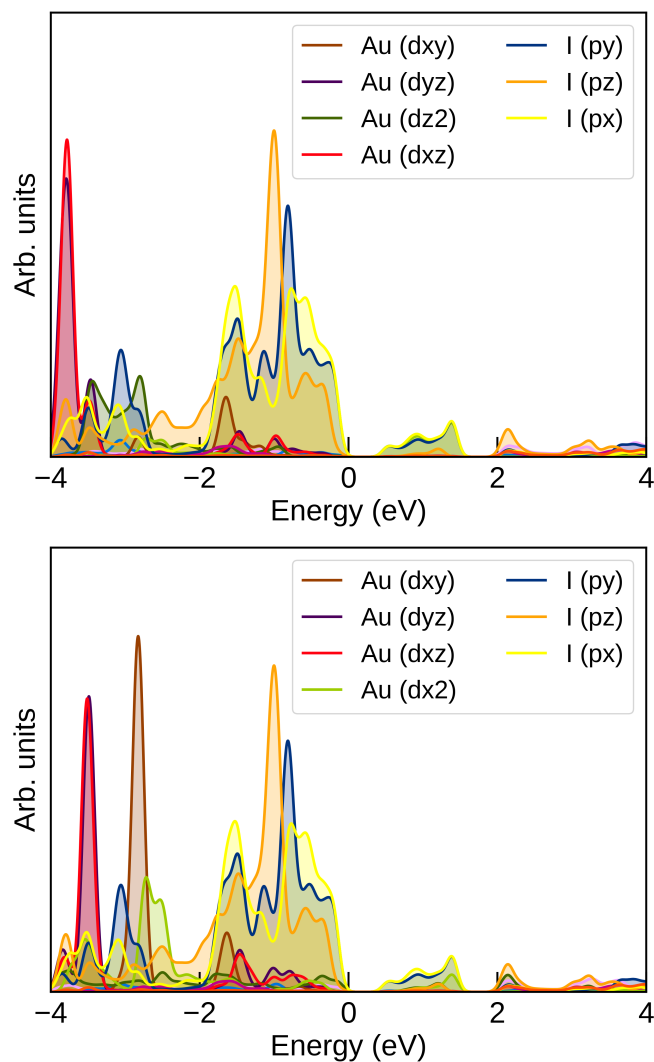


Figure B.3: Density of states of the  $\text{K}_2\text{Au}_2\text{I}_6$  I4/mmm structure. The top figure includes the Gold atoms in which their electrons sit within the  $d_{z^2}$  orbital and the bottom figure includes the gold atom where the electrons sit within the  $d_{x^2-y^2}$  orbital.

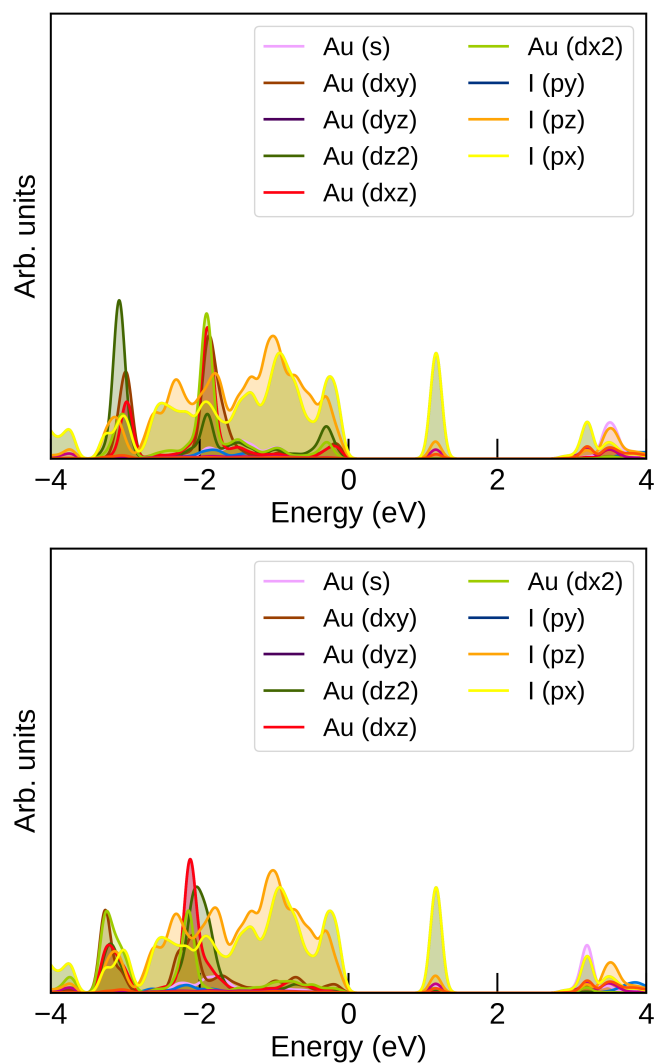


Figure B.4: Density of states of the  $\text{Rb}_2\text{Au}_2\text{I}_6$   $P2_1/c$  structure. The top figure includes the Gold atoms in which there electrons sit within the  $d_{z^2}$  orbital and bottom figure includes the gold atom where the electrons sit within the  $d_{x^2-y^2}$  orbital.

## B.3 Phonon Dielectrics

### Dielectric Code

The code below was used to determine the size of the dielectric constant in relation to the phonon mode frequency:

```
1  const BigNumber = require('bignumber.js');
2  const csv = require('csvtojson');
3  const inquirer = require('inquirer');
4  const fs = require('fs');
5  const { writeFile } = require('fs/promises');
6  const { parseAsync } = require('json2csv');
7
8  const converter = csv({
9    noheader:true,
10   trim:true,
11 });
12
13 // Helper for easier logging
14 BigNumber.prototype[require('util').inspect.custom] = BigNumber.
    prototype.valueOf;
15
16 BigNumber.set({
17   DECIMAL_PLACES: 100
18 });
19
20 /**
21  * Models
22  */
23 class Question {
24   constructor({ type, name, message }) {
25     this.type = type;
26     this.name = name;
27     this.message = message;
28   }
29 }
```

```
30
31 /**
32  * Prompts
33  */
34 const get_csv_file_path = async () => {
35   const csv_file_path_question = new Question({
36     type: 'string',
37     name: 'csv_file_path',
38     message: 'Please enter the path to your csv:'
39   });
40
41   const { csv_file_path } = await inquirer.prompt([
42     csv_file_path_question
43   ]);
44
45   if (!csv_file_path) {
46     throw new Error('No filepath provided');
47   }
48
49   fs.access(csv_file_path, (error) => {
50     if (error) {
51       throw new Error(`File not found at path ${csv_file_path}`);
52     }
53     return;
54   });
55
56   return csv_file_path;
57 };
58
59 const get_atomic_masses = async () => {
60   const first_atomic_mass_label_question = new Question({
61     type: 'string',
62     name: 'first_atomic_mass_label',
63     message: 'Enter the first element label:'
64   });
65
66   const first_atomic_mass_question = new Question({
```

```
65     type: 'string',
66     name: 'first_atomic_mass',
67     message: 'Enter the first elements atomic mass:'
68 });
69
70 const second_atomic_mass_label_question = new Question({
71     type: 'string',
72     name: 'second_atomic_mass_label',
73     message: 'Enter the second element label:'
74 });
75
76 const second_atomic_mass_question = new Question({
77     type: 'string',
78     name: 'second_atomic_mass',
79     message: 'Enter the second elements atomic mass:'
80 });
81
82 const third_atomic_mass_label_question = new Question({
83     type: 'string',
84     name: 'third_atomic_mass_label',
85     message: 'Enter the third element label:'
86 });
87
88 const third_atomic_mass_question = new Question({
89     type: 'string',
90     name: 'third_atomic_mass',
91     message: 'Enter the third elements atomic mass:'
92 });
93
94 const answers = await inquirer.prompt([
95     first_atomic_mass_label_question,
96     first_atomic_mass_question,
97     second_atomic_mass_label_question,
98     second_atomic_mass_question,
99     third_atomic_mass_label_question,
100    third_atomic_mass_question
```

```
101   });
102
103   const elements = {};
104   elements[answers.first_atomic_mass_label] = new BigNumber(answers.
105     first_atomic_mass);
106   elements[answers.second_atomic_mass_label] = new BigNumber(answers.
107     second_atomic_mass);
108   elements[answers.third_atomic_mass_label] = new BigNumber(answers.
109     third_atomic_mass);
110
111   return elements;
112 };
113
114 const get_volume = async () => {
115   const question = new Question({
116     type: 'string',
117     name: 'volume',
118     message: 'Enter the volume:'
119   });
120
121   const { volume } = await inquirer.prompt([ question ]);
122
123   return new BigNumber(volume);
124 };
125
126 /**
127  * Utils
128  */
129 const map_fields_to_dimensions = (fields) => fields.map(({ field1,
130   field2, field3 }) => ({
131   x: new BigNumber(field1),
132   y: new BigNumber(field2),
133   z: new BigNumber(field3)
134 }));
135
136 const chunk_array = (array, chunk_size) => {
```

```
133   const chunked_array = [];
134   for (let i = 0; i < array.length; i += chunk_size) {
135     const chunk = array.slice(i, i + chunk_size);
136     chunked_array.push(chunk);
137   }
138
139   return chunked_array;
140 };
141
142 const calculate_mass_in_kilograms = (atomic_mass_value) =>
    atomic_mass_value.multipliedBy(proton_mass);
143
144 const calculate_um_values_for_dimension = (dimension,
    atomic_mass_value) => {
145   const mass_in_kilograms = calculate_mass_in_kilograms(
    atomic_mass_value);
146   return dimension.multipliedBy(m0.dividedBy(mass_in_kilograms).
    squareRoot());
147 };
148
149 const calculate_the_constant = (volume) => {
150   return m0.dividedBy(volume.multipliedBy(vacuum.multipliedBy(m4.
    multipliedBy(pi).multipliedBy(pi)))
151 };
152
153 /**
154  * /*);
155  * Constants
156  */
157 const m0 = new BigNumber(1);
158 const proton_mass = new BigNumber('1.6726219236951E-27');
159 const vacuum = new BigNumber('8.854187812812E-12');
160 const e0 = new BigNumber('8.854187812813E-12');
161 const e = new BigNumber('1.602176634E-19');
162 const pi = new BigNumber('3.1415926535')
163 const m4 = new BigNumber('4')
```

```
164
165 /**
166  * Main function
167  */
168
169 const run = async () => {
170   try {
171     const output = [Array(100).fill(null)];
172     // const csv_file_path = await get_csv_file_path();
173
174     // const atomic_masses = await get_atomic_masses();
175     const atomic_masses = {
176       'Rb': new BigNumber('132.90545'),
177       'Au': new BigNumber('196.96657'),
178       'Cl': new BigNumber('35.453'),
179     };
180
181     // const volume = await get_volume();
182     const volume = new BigNumber('563.68E-30');
183
184     const the_constant = calculate_the_constant(volume);
185     output.push(['The constant']);
186     output.push([ the_constant ]);
187
188     const input = await converter.fromFile('C:/Users/Jordan/Desktop/
189     Desk/VS/phonon_modes/phonon_modes/BEC_Phonons/BEC_phonons.csv');
190
191     const bec_fields_input = input.slice(0, 60);
192     const phonons_input = input.slice(60, 1260);
193     const frequencies_input = input.slice(1260);
194
195     const bec_fields = map_fields_to_dimensions(bec_fields_input);
196     const phonons = map_fields_to_dimensions(phonons_input);
197
198     const frequencies = frequencies_input.map(({ field1: frequency })
=> {
```

```
198     const freq = new BigNumber(frequency).multipliedBy('1E12');
199     return freq.multipliedBy(freq);
200   });
201
202   output.push(['Frequencies']);
203   frequencies.forEach((freq) => output.push([ freq ]));
204
205   const chunked_bec_fields = chunk_array(bec_fields, 3);
206   const chunked_phonons = chunk_array(phonons, 20);
207
208   const alpha = chunked_phonons.map((phonon, phonon_index) => {
209     output.push([ `Phonon mode ${phonon_index + 1}` ]);
210     const unsummed_alpha_values = phonon.map(({ x, y, z }, index) =>
211     {
212       let atomic_mass_value;
213       if (index < 4) {
214         atomic_mass_value = Object.values(atomic_masses)[0];
215       } else if (index < 8) {
216         atomic_mass_value = Object.values(atomic_masses)[1];
217       } else {
218         atomic_mass_value = Object.values(atomic_masses)[2];
219       }
220
221       const x_um_value = calculate_um_values_for_dimension(x,
222       atomic_mass_value);
223       const y_um_value = calculate_um_values_for_dimension(y,
224       atomic_mass_value);
225       const z_um_value = calculate_um_values_for_dimension(z,
226       atomic_mass_value);
227
228       const bec_matrix = chunked_bec_fields[index];
229
230       const alpha_matrix = bec_matrix.map(({ x: bec_x, y: bec_y, z:
231       bec_z }) => ({
232         x: bec_x.multipliedBy(e).multipliedBy(x_um_value),
233         y: bec_y.multipliedBy(e).multipliedBy(y_um_value),
```

```
229         z: bec_z.multipliedBy(e).multipliedBy(z_um_value),
230     }));
231
232     output.push([ 'atomic_mass_value', 'x_um_value', 'y_um_value',
233                 'z_um_value' ]);
234     output.push([ atomic_mass_value, x_um_value, y_um_value,
235                 z_um_value ]);
236
237     const alpha_x = [];
238     const alpha_y = [];
239     const alpha_z = [];
240
241     alpha_matrix.forEach(({ x, y, z }, alpha_index) => {
242         if (alpha_index === 0) {
243             alpha_x.push(BigNumber.sum.apply(null, [ x, y, z ]));
244         } else if (alpha_index === 1) {
245             alpha_y.push(BigNumber.sum.apply(null, [ x, y, z ]));
246         } else if (alpha_index === 2) {
247             alpha_z.push(BigNumber.sum.apply(null, [ x, y, z ]));
248         }
249     });
250
251     return {
252         x: BigNumber.sum.apply(null, alpha_x),
253         y: BigNumber.sum.apply(null, alpha_y),
254         z: BigNumber.sum.apply(null, alpha_z),
255     };
256
257     const alpha_x = unsummed_alpha_values.map(({ x }) => x);
258     const alpha_y = unsummed_alpha_values.map(({ y }) => y);
259     const alpha_z = unsummed_alpha_values.map(({ z }) => z);
260
261     const x = BigNumber.sum.apply(null, alpha_x);
262     const y = BigNumber.sum.apply(null, alpha_y);
263     const z = BigNumber.sum.apply(null, alpha_z);
```

```
263
264     output.push([ 'alpha_x', 'alpha_y', 'alpha_z' ]);
265     output.push([ x, y, z ]);
266
267     return {
268         x,
269         y,
270         z,
271     };
272 });
273
274     output.push([ 'Dimensions squared multiplied by the constant' ]);
275
276     const alpha_matrices = alpha.map(({ x, y, z }, index) => {
277         const xx = x.multipliedBy(x).multipliedBy(the_constant);
278         const xy = x.multipliedBy(y).multipliedBy(the_constant);
279         const xz = x.multipliedBy(z).multipliedBy(the_constant);
280         const yx = y.multipliedBy(x).multipliedBy(the_constant);
281         const yy = y.multipliedBy(y).multipliedBy(the_constant);
282         const yz = y.multipliedBy(z).multipliedBy(the_constant);
283         const zx = z.multipliedBy(x).multipliedBy(the_constant);
284         const zy = z.multipliedBy(y).multipliedBy(the_constant);
285         const zz = z.multipliedBy(z).multipliedBy(the_constant);
286
287         output.push([ `Phonon mode ${index + 1} after squaring the
288 dimension then multiplying by the constant` ]);
289         output.push([
290             xx.toExponential(20), xy.toExponential(20), xz.toExponential
291 (20)
292             ]);
293         output.push([
294             yx.toExponential(20), yy.toExponential(20), yz.toExponential
295 (20)
296             ]);
297         output.push([
298             zx.toExponential(20), zy.toExponential(20), zz.toExponential
```

```
(20)
296     });
297
298     return {
299         xx,
300         xy,
301         xz,
302         yx,
303         yy,
304         yz,
305         zx,
306         zy,
307         zz
308     };
309 });
310
311 let results = alpha_matrices.map((alpha_matrix, index) => {
312     const frequency = frequencies[index];
313
314     let xx = alpha_matrix.xx.dividedBy(frequency);
315     let xy = alpha_matrix.xy.dividedBy(frequency);
316     let xz = alpha_matrix.xz.dividedBy(frequency);
317     let yx = alpha_matrix.yx.dividedBy(frequency);
318     let yy = alpha_matrix.yy.dividedBy(frequency);
319     let yz = alpha_matrix.yz.dividedBy(frequency);
320     let zx = alpha_matrix.zx.dividedBy(frequency);
321     let zy = alpha_matrix.zy.dividedBy(frequency);
322     let zz = alpha_matrix.zz.dividedBy(frequency);
323
324     output.push([ `Phonon mode ${index + 1} after dividing by the
frequency: ${frequency.toExponential(20)}` ]);
325     output.push([
326         xx.toExponential(20), xy.toExponential(20), xz.toExponential
(20)
327     ]);
328     output.push([
```

```
329     yx.toExponential(20), yy.toExponential(20), yz.toExponential
330     (20)
331     ]);
332     output.push([
333     zx.toExponential(20), zy.toExponential(20), zz.toExponential
334     (20)
335     ]);
336
337     return {
338     xx,
339     xy,
340     xz,
341     yx,
342     yy,
343     yz,
344     zx,
345     zy,
346     zz
347     };
348
349     const xx_result = BigNumber.sum.apply(null, results.map(({ xx })
350     => xx)).toExponential(20);
351     const xy_result = BigNumber.sum.apply(null, results.map(({ xy })
352     => xy)).toExponential(20);
353     const xz_result = BigNumber.sum.apply(null, results.map(({ xz })
354     => xz)).toExponential(20);
355     const yx_result = BigNumber.sum.apply(null, results.map(({ yx })
356     => yx)).toExponential(20);
357     const yy_result = BigNumber.sum.apply(null, results.map(({ yy })
358     => yy)).toExponential(20);
359     const yz_result = BigNumber.sum.apply(null, results.map(({ yz })
360     => yz)).toExponential(20);
361     const zx_result = BigNumber.sum.apply(null, results.map(({ zx })
362     => zx)).toExponential(20);
363     const zy_result = BigNumber.sum.apply(null, results.map(({ zy })
```

```
=> zy)).toExponential(20);
356   const zz_result = BigNumber.sum.apply(null, results.map(({ zz })
=> zz)).toExponential(20);
357
358   const summed_results_matrix = [
359     [ null, 'X', 'Y', 'Z' ],
360     [ 'X', xx_result, xy_result, xz_result ],
361     [ 'Y', yx_result, yy_result, yz_result ],
362     [ 'Z', zx_result, zy_result, zz_result ]
363   ];
364
365   // results = results.map((res) => res.valueOf());
366   const formatted_results = results.map((res) => Object.values(res).
map((obj) => obj.valueOf()));
367
368   const result = [
369     [ 'XX', 'XY', 'XZ', 'YX', 'YY', 'YZ', 'ZX', 'ZY', 'ZZ' ],
370     ...formatted_results,
371   ];
372
373   const result_csv_string = await parseAsync(result, {
374     header: false
375   });
376
377   const summed_results_string = await parseAsync(
summed_results_matrix, {
378     header: false
379   });
380
381   const parsed_output = await parseAsync(output, {
382     header: false
383   });
384
385   const csv_string = `${parsed_output}\n\n${result_csv_string}\n\n,
${summed_results_string}`;
386
```

```
387     await writeFile('./test.csv', csv_string);
388
389   } catch (error) {
390     console.log(error);
391     process.exit(1);
392   }
393 };
394
395 run();
```

The tables below show the dielectric constant based on the size of the phonon mode. All structures explored were in the  $I4/mmm$  space group and the total dielectric constant can be found in the table of dielectric constants found in [chapter 4](#).

Phonon	XX	XY	XZ	YX	YY	YZ	ZX	ZY	ZZ
1	0	0	0	0	0	0	0	0	0
2	0	0	0	0	0	0	0	0	0.185289334
3	0	0	0	0	0	0	0	0	0
4	0	0	0	0	0	0	0	0	0
5	0.065826256	-0.066751265	0	-0.066751265	0.067689272	0	0	0	0
6	0.067690523	0.066751265	0	0.066751265	0.06582504	0	0	0	0
7	4.71E-07	4.70E-07	-6.92E-09	4.70E-07	4.70E-07	-6.91E-09	-6.92E-09	-6.91E-09	1.02E-10
8	0	0	0	0	0	0	0	0	0
9	0	0	0	0	0	0	0	0	0
10	6.48E-07	6.47E-07	-1.41E-07	6.47E-07	6.46E-07	-1.41E-07	-1.41E-07	-1.41E-07	3.07E-08
11	0	0	0	0	0	0	0	0	0
12	0	0	0	0	0	0	0	0	0
13	0	0	0	0	0	0	0	0	0
14	0	0	0	0	0	0	0	0	0
15	0.016714544	-0.016510281	0	-0.016510281	0.016308514	0	0	0	0
16	0.016308559	0.016510281	0	0.016510281	0.016714497	0	0	0	0
17	0	0	0	0	0	0	0	0	0
18	5.32E-07	-5.40E-07	0	-5.40E-07	5.47E-07	0	0	0	0
19	0	0	0	0	0	0	0	0	0
20	0	0	0	0	0	0	0	0	0.397327459
21	0	0	0	0	0	0	0	0	0
22	0	0	0	0	0	0	0	0	0
23	0.221115282	-0.235505628	0	-0.235505628	0.25083251	0	0	0	0
24	0.250839193	0.235505628	0	0.235505628	0.22110939	0	0	0	0
25	0	0	0	0	0	0	0	0	0
26	0	0	0	0	0	0	0	0	0
27	0	0	0	0	0	0	0	0	0
28	0	0	0	0	0	0	0	0	0
29	0	0	0	0	0	0	0	0	0
30	0	0	0	0	0	0	0	0	0
31	0	0	0	0	0	0	0	0	0.00131832
32	0	0	0	0	0	0	0	0	0
33	0	0	0	0	0	0	0	0	0
34	0	0	0	0	0	0	0	0	0
35	0	0	0	0	0	0	0	0	0
36	1.664641359	-1.772207919	0	-1.772207919	1.886725263	0	0	0	0
37	1.886703138	1.772207919	0	1.772207919	1.66466088	0	0	0	0
38	0	0	0	0	0	0	0	0	0
39	0	0	0	0	0	0	0	0	0
40	0	0	0	0	0	0	0	0	0
41	0	0	0	0	0	0	0	0	0
42	0	0	0	0	0	0	0	0	0
43	0	0	0	0	0	0	0	0	0
44	0	0	0	0	0	0	0	0	0
45	0	0	0	0	0	0	0	0	0
46	0	0	0	0	0	0	0	0	0
47	2.151816071	-2.292848805	0	-2.292848805	2.443125002	0	0	0	0
48	2.443171648	2.292848805	0	2.292848805	2.151774987	0	0	0	0
49	0	0	0	0	0	0	0	0	0
50	0	0	0	0	0	0	0	0	0
51	0	0	0	0	0	0	0	0	4.5776047
52	3.76E-09	-2.96E-09	0	-2.96E-09	2.33E-09	0	0	0	0
53	0	0	0	0	0	0	0	0	0
54	0	0	0	0	0	0	0	0	0
55	0	0	0	0	0	0	0	0	0
56	0	0	0	0	0	0	0	0	0
57	0	0	0	0	0	0	0	0	0

Table B.1: Dielectric response to phonons for the Cs<sub>2</sub>Au<sub>2</sub>Cl<sub>6</sub>

Phonon	XX	XY	XZ	YX	YY	YZ	ZX	ZY	ZZ
1	0	0	0	0	0	0	0	0	0
2	0	0	0	0	0	0	0	0	0.098363636
3	0	0	0	0	0	0	0	0	0
4	0	0	0	0	0	0	0	0	0
5	0.053749209	0.025181923	0	0.025181923	0.011797927	0	0	0	0
6	0.011795665	-0.025181923	0	-0.025181923	0.053759518	0	0	0	0
7	6.31E-07	6.30E-07	-2.92E-08	6.30E-07	6.29E-07	-2.91E-08	-2.92E-08	-2.91E-08	1.35E-09
8	0	0	0	0	0	0	0	0	0
9	0	0	0	0	0	0	0	0	0
10	7.62E-07	7.60E-07	-1.34E-07	7.60E-07	7.58E-07	-1.33E-07	-1.34E-07	-1.33E-07	2.35E-08
11	0	0	0	0	0	0	0	0	0
12	0	0	0	0	0	0	0	0	0
13	0	0	0	0	0	0	0	0	0
14	0	0	0	0	0	0	0	0	0
15	0.007474696	-0.01728446	0	-0.01728446	0.039968526	0	0	0	0
16	0.039965622	0.01728446	0	0.01728446	0.007475239	0	0	0	0
17	0	0	0	0	0	0	0	0	0
18	5.83E-08	-5.82E-08	0	-5.82E-08	5.82E-08	0	0	0	0
19	0	0	0	0	0	0	0	0	0
20	0	0	0	0	0	0	0	0	0.154741334
21	0	0	0	0	0	0	0	0	0
22	0	0	0	0	0	0	0	0	0
23	0.002586668	-0.012635525	0	-0.012635525	0.061722839	0	0	0	0
24	0.061731948	0.012635525	0	0.012635525	0.002586286	0	0	0	0
25	0	0	0	0	0	0	0	0	0
26	0	0	0	0	0	0	0	0	0
27	0	0	0	0	0	0	0	0	0
28	0	0	0	0	0	0	0	0	0
29	0	0	0	0	0	0	0	0	0
30	0	0	0	0	0	0	0	0	0
31	0	0	0	0	0	0	0	0	0.000505491
32	0.040270331	0.259513651	0	0.259513651	1.67238097	0	0	0	0
33	1.672621137	-0.259513651	0	-0.259513651	0.040264549	0	0	0	0
34	0	0	0	0	0	0	0	0	0
35	0	0	0	0	0	0	0	0	0
36	0	0	0	0	0	0	0	0	0
37	0	0	0	0	0	0	0	0	0
38	0	0	0	0	0	0	0	0	0
39	0	0	0	0	0	0	0	0	0
40	0	0	0	0	0	0	0	0	0
41	0	0	0	0	0	0	0	0	0
42	0	0	0	0	0	0	0	0	0
43	0	0	0	0	0	0	0	0	0
44	0	0	0	0	0	0	0	0	0
45	0	0	0	0	0	0	0	0	0
46	0	0	0	0	0	0	0	0	0
47	0	0	0	0	0	0	0	0	0
48	0	0	0	0	0	0	0	0	0
49	6.18E-09	-9.34E-09	0	-9.34E-09	1.41E-08	0	0	0	0
50	0.216756722	-1.47058666	0	-1.47058666	9.97719982	0	0	0	0
51	9.976352896	1.47058666	0	1.47058666	0.216775123	0	0	0	0
52	0	0	0	0	0	0	0	0	0
53	0	0	0	0	0	0	0	0	0
54	0	0	0	0	0	0	0	0	5.63689007
55	0	0	0	0	0	0	0	0	0
56	0	0	0	0	0	0	0	0	0
57	0	0	0	0	0	0	0	0	0

Table B.2: Dielectric response to phonons for the Cs<sub>2</sub>Au<sub>2</sub>Br<sub>6</sub>

Phonon	XX	XY	XZ	YX	YY	YZ	ZX	ZY	ZZ
1	0	0	0	0	0	0	0	0	0
2	0	0	0	0	0	0	0	0	0.119289905
3	0.016279312	0.012309169	0	0.012309169	0.009307251	0	0	0	0
4	0.009305581	-0.012309192	0	-0.012309192	0.016282295	0	0	0	0
5	0	0	0	0	0	0	0	0	0
6	0	0	0	0	0	0	0	0	0
7	1.37E-06	1.41E-06	-2.84E-07	1.41E-06	1.46E-06	-2.94E-07	-2.84E-07	-2.94E-07	5.91E-08
8	0	0	0	0	0	0	0	0	0
9	0	0	0	0	0	0	0	0	0
10	1.55E-06	1.64E-06	-7.10E-07	1.64E-06	1.73E-06	-7.50E-07	-7.10E-07	-7.50E-07	3.24E-07
11	0	0	0	0	0	0	0	0	0
12	0	0	0	0	0	0	0	0	0
13	0.270783889	0.302815018	0	0.302815018	0.338635121	0	0	0	0
14	0.338613003	-0.302815522	0	-0.302815522	0.270802478	0	0	0	0
15	0	0	0	0	0	0	0	0	0
16	0	0	0	0	0	0	0	0	0
17	0	0	0	0	0	0	0	0	0
18	2.96E-07	-2.54E-07	6.31E-13	-2.54E-07	2.18E-07	-5.42E-13	6.31E-13	-5.42E-13	1.35E-18
19	0	0	0	0	0	0	0	0	0.160447579
20	0	0	0	0	0	0	0	0	0
21	0.118481568	0.072565744	0	0.072565744	0.044443935	0	0	0	0
22	0.044436345	-0.072565626	0	-0.072565626	0.118501421	0	0	0	0
23	0	0	0	0	0	0	0	0	0
24	0	0	0	0	0	0	0	0	0
25	0	0	0	0	0	0	0	0	0.387900022
26	0	0	0	0	0	0	0	0	0
27	0	0	0	0	0	0	0	0	0
28	0	0	0	0	0	0	0	0	0
29	0	0	0	0	0	0	0	0	0
30	0	0	0	0	0	0	0	0	0
31	0	0	0	0	0	0	0	0	0
32	0	0	0	0	0	0	0	0	0
33	5.15290902	2.399876928	0	2.399876928	1.62104046	0	0	0	0
34	1.621032316	-2.399881224	0	-2.399881224	5.152939587	0	0	0	0
35	0	0	0	0	0	0	0	0	0
36	0	0	0	0	0	0	0	0	0
37	0	0	0	0	0	0	0	0	0
38	0	0	0	0	0	0	0	0	0
39	0	0	0	0	0	0	0	0	0
40	3.785596018	1.289321403	0	1.289321403	0.771172747	0	0	0	0
41	0.771176686	-1.28931974	0	-1.28931974	3.785596018	0	0	0	0
42	0	0	0	0	0	0	0	0	0
43	0	0	0	0	0	0	0	0	0
44	0	0	0	0	0	0	0	0	0
45	0	0	0	0	0	0	0	0	0
46	0	0	0	0	0	0	0	0	0
47	0	0	0	0	0	0	0	0	5.870882835
48	0	0	0	0	0	0	0	0	0
49	0	0	0	0	0	0	0	0	0
50	0	0	0	0	0	0	0	0	0
51	0	0	0	0	0	0	0	0	0
52	1.07E-18	3.58E-19	0	3.58E-19	1.19E-19	0	0	0	0
53	3.87E-09	-1.11E-08	0	-1.11E-08	3.18E-08	0	0	0	0
54	0	0	0	0	0	0	0	0	0
55	0	0	0	0	0	0	0	0	0
56	0	0	0	0	0	0	0	0	0
57	0	0	0	0	0	0	0	0	0

Table B.3: Dielectric response to phonons for the Cs<sub>2</sub>Au<sub>2</sub>I<sub>6</sub>

Phonon	XX	XY	XZ	YX	YY	YZ	ZX	ZY	ZZ
1	0	0	0	0	0	0	0	0	0
2	0	0	0	0	0	0	0	0	0.19839909
3	0	0	0	0	0	0	0	0	0
4	0	0	0	0	0	0	0	0	0
5	0.046598214	0.060713732	0	0.060713732	0.07910512	0	0	0	0
6	0.07925568	-0.060713733	0	-0.060713733	0.046509693	0	0	0	0
7	8.66E-07	8.65E-07	-3.79E-08	8.65E-07	8.64E-07	-3.79E-08	-3.79E-08	-3.79E-08	1.66E-09
8	0	0	0	0	0	0	0	0	0
9	0	0	0	0	0	0	0	0	0
10	6.89E-07	6.94E-07	-1.97E-07	6.94E-07	6.98E-07	-1.98E-07	-1.97E-07	-1.98E-07	5.61E-08
11	0	0	0	0	0	0	0	0	0
12	0	0	0	0	0	0	0	0	0
13	0	0	0	0	0	0	0	0	0
14	0	0	0	0	0	0	0	0	0
15	0.032740677	0.026907115	0	0.026907115	0.022112948	0	0	0	0
16	0.022124019	-0.026907115	0	-0.026907115	0.032724291	0	0	0	0
17	0	0	0	0	0	0	0	0	0
18	5.82E-07	-5.93E-07	0	-5.93E-07	6.04E-07	0	0	0	0
19	0	0	0	0	0	0	0	0	0
20	0	0	0	0	0	0	0	0	0.368637484
21	0	0	0	0	0	0	0	0	0
22	0	0	0	0	0	0	0	0	0
23	0.039544349	0.120519589	0	0.120519589	0.367308397	0	0	0	0
24	0.36698208	-0.12051959	0	-0.12051959	0.039579512	0	0	0	0
25	0	0	0	0	0	0	0	0	0
26	0	0	0	0	0	0	0	0	0
27	0	0	0	0	0	0	0	0	0
28	0	0	0	0	0	0	0	0	0
29	0	0	0	0	0	0	0	0	0.004949501
30	0	0	0	0	0	0	0	0	0
31	0	0	0	0	0	0	0	0	0
32	0	0	0	0	0	0	0	0	0
33	0	0	0	0	0	0	0	0	0
34	0.910779677	2.677222321	0	2.677222321	7.869652272	0	0	0	0
35	7.865350986	-2.677222325	0	-2.677222325	0.911277754	0	0	0	0
36	0	0	0	0	0	0	0	0	0
37	0	0	0	0	0	0	0	0	0
38	0	0	0	0	0	0	0	0	0
39	0	0	0	0	0	0	0	0	0
40	0	0	0	0	0	0	0	0	0
41	0	0	0	0	0	0	0	0	0
42	0	0	0	0	0	0	0	0	0
43	0	0	0	0	0	0	0	0	0
44	0	0	0	0	0	0	0	0	0
45	8.17E-09	-8.32E-09	0	-8.32E-09	8.48E-09	0	0	0	0
46	0.944321733	2.885710467	0	2.885710467	10.8183133	0	0	0	0
47	10.82386841	-2.885710477	0	-2.885710477	0.943727237	0	0	0	0
48	0	0	0	0	0	0	0	0	14.17993362
49	0	0	0	0	0	0	0	0	0
50	0	0	0	0	0	0	0	0	0
51	0	0	0	0	0	0	0	0	0
52	0	0	0	0	0	0	0	0	0
53	0	0	0	0	0	0	0	0	0
54	0	0	0	0	0	0	0	0	0
55	0	0	0	0	0	0	0	0	0
56	0	0	0	0	0	0	0	0	0
57	0	0	0	0	0	0	0	0	0

Table B.4: Dielectric response to phonons in the  $\text{Rb}_2\text{Au}_2\text{Cl}_6$